UNIVERSITY OF SOUTHAMPTON

FACULTY OF ENGINEERING, SCIENCE & MATHEMATICS

School of Ocean & Earth Science

Fundamental Magnetic Properties of Greigite (Fe_3S_4)

By

Liao Chang

Thesis for the degree of Doctor of Philosophy

January 2009

UNIVERSITY OF SOUTHAMPTON

ABSTRACT

FACULTY OF ENGINEERING, SCIENCE & MATHEMATICS

SCHOOL OF OCEAN & EARTH SCIENCE

Doctor of Philosophy

FUNDAMENTAL MAGNETIC PROPERTIES OF GREIGITE

By Liao Chang

Over the last twenty years, greigite (Fe_3S_4), an authigenic magnetic iron sulphide mineral, has been increasingly identified in sulphate-reducing marine and lacustrine sedimentary systems. Its presence can significantly affect palaeomagnetic and environmental magnetic records. Understanding the recording characteristics of any magnetic mineral requires that its fundamental magnetic properties are known. However, unlike magnetite (Fe_3O_4) and other common terrestrial magnetic minerals, the fundamental magnetic properties of greigite are poorly known. The metastability of greigite and difficulties in producing pure greigite samples make it difficult to characterize its magnetic properties. In this study, pure synthetic greigite samples were produced using a new hydrothermal method. Sample purity has been confirmed by X-ray diffraction, neutron diffraction, Mössbauer spectroscopy and elemental analyses. Based on this suite of highly pure synthetic greigite samples, as well as a range of natural greigite samples collected from widely distributed localities, extensive analyses have documented some of the fundamental magnetic properties of greigite. The saturation magnetization (M_s) of greigite was determined to be 59 Am^2kg^{-1} (equivalent to 3.13 μ_B/formula unit (f.u.)) from magnetic measurements and 3.03 μ_B/f.u. from neutron scattering. Neutron scattering, Mössbauer spectroscopy and X-ray magnetic circular dichroism were used to probe the magnetic structure of greigite. Results confirm that greigite has a collinear ferrimagnetic structure with antiferromagnetic coupling between the tetrahedral and the octahedral sites, but with lower magnetic moments of Fe ions for the two sublattices compared to magnetite. The low magnetic moment in greigite compared to magnetite is probably caused by an increased degree of covalency between iron and sulphur compared to oxygen ligands, and/or by greater delocalization of the 3*d* electrons. By measuring the low-temperature M_s of pure greigite samples and based on the Bloch spin wave expansion, the spin wave stiffness of greigite was determined to be ~193 meV·$Å^2$, with a corresponding exchange constant J_{AB} of ~1.03 meV. High-temperature magnetic analyses on a stable natural greigite sample from Italy indicate that the Curie temperature of greigite most exceed 350°C. However, thermal alteration of greigite at elevated temperatures precludes determination of its Curie temperature. Production of large-grained synthetic greigite samples enables an extension of our knowledge of the magnetic properties of greigite to include the pseudo-single-domain/multi-domain region, which now provides coverage of the complete domain state range. Low-temperature magnetic analyses indicate that greigite has strong domain-state dependence of magnetic properties, although greigite has no low-temperature magnetic transitions. These fundamental studies provide important new magnetic data for greigite that will benefit future efforts to model magnetizations of greigite in a wide range of palaeomagnetic and environmental magnetic contexts.

List of Contents

List of Figures

List of Tables

DECLARATION OF AUTHORSHIP

I, Liao Chang, declare that the thesis entitled:

Fundamental Magnetic Properties of Greigite (Fe_3S_4),

and the work presented in the thesis are both my own, and have been generated by me as the result of my own original research. I confirm that:

- this work was done wholly while in candidature for a research degree at this University;

- where any part of this thesis has previously been submitted for a degree or any other qualification at this University or any other institution, this has been clearly stated;

- where I have consulted the published work of others, this is always clearly attributed;

- where I have quoted from the work of others, the source is always given. With the exception of such quotations, this thesis is entirely my own work;

- I have acknowledged all main sources of help;

- where the thesis is based on work done by myself jointly with others, I have made clear exactly what was done by others and what I have contributed myself;

- parts of this work have been published as:

Chang, L., A. P. Roberts, A. R. Muxworthy, Y. Tang, Q. Chen, C. J. Rowan, Q. Liu and P. Pruner (2007), Magnetic characteristics of synthetic pseudo-single-domain and multi-domain greigite (Fe_3S_4), *Geophys. Res. Lett.*, *34*, L24304, doi:10.1029/2007GL032114.

Chang, L., A. P. Roberts, Y. Tang, B. D. Rainford, A. R. Muxworthy, and Q. Chen (2008), Fundamental magnetic parameters from pure synthetic greigite (Fe_3S_4), *J. Geophys. Res.*, *113*, B06104, doi:10.1029/2007JB005502.

Chang, L., A. P. Roberts, C. J. Rowan, Y. Tang, P. Pruner, Q. Chen, and C-S. Horng, Low-temperature magnetic properties of greigite (Fe_3S_4), *Geochem., Geophys., Geosyst.*, *10*, Q01Y04, doi:10.1029/2008GC002276, 2009.

Signed: ……………………………………………………

Date: ……………………………………………………...

Acknowledgements

Many people will be remembered for their support throughout my PhD work. First, I thank Andrew Roberts, for his excellent supervision, friendship and encouragement and help to me through hard times. I have directly benefitted from *Mr Greigite*'s knowledge of greigite and from many meetings with him. I appreciate his efforts in reading different versions of my manuscripts and his many probing questions. I also thank Adrian Muxworthy for his advice throughout this project and for giving me feedback on papers. I have benefited from his knowledge of rock magnetism.

Thanks are given to the chemists and physicists with whom I have worked. The unique expertise of Yan Tang and Qianwang Chen in synthesizing perfect greigite samples has made possible previously impossible investigations. This really made it worth my *17 hours' standing on a train*. Special thanks are given to Yan for her long hours of work in the disgusting H_2S environment. I thank Mark Weller and Stefan Hunger for the initial test of greigite synthesis. I thank Brian Rainford for guiding me through the mysterious neutrons and large-scale physics facilities in France and the UK, and for patiently lecturing me on solid state physics. I thank his excellent inputs into papers and for allowing me to use his high-field VSM. I am grateful to Gerrit van der Laan for his inspiration and discussion concerning XMCD data acquisition and interpretation and for sending me XMCD data for magnetite.

I thank Stefan Hunger and Liane Benning for providing a synthetic fine-grained greigite sample, Chorng-Shern Horng for providing the purest known natural greigite sample, Chris Rowan for providing natural SP greigite samples, Petr Pruner for arranging field work in the Sokolov brown coal basin in the Czech Republic and for identifying greigite-rich layers.

I thank the Institute for Rock Magnetism, University of Minnesota, for providing two visiting fellowships. Peat Sølheid and Thelma Berquó undertook Mössbauer measurements and helped with data interpretation. I thank Mike Jackson, Julie Bowles, Brian Carter-Stiglitz, Peat Sølheid, Thelma Berquó, Amy Chen, Bruce Moskowitz, and Subir Banerjee for their help, discussions and hospitality. Thanks also go to the Institut Laue-Langevin, Grenoble, for providing access to costly neutron beam time. I thank Ross Stewart and Clemens Ritter for help with neutron scattering experiments and for processing neutron diffraction data. I thank the Daresbury

Laboratory in the UK and the Lawrence Berkeley National Laboratory in the USA for also providing access to expensive beam time for synchrotron radiation measurements. Richard Pattrick is thanked for organizing the XMCD experiment. Vicky Coker and Neil Telling helped with XMCD measurements.

At NOCS, I appreciate technical assistance from Richard Pearce for SEM and elemental analyses, Ross Williams for XRD measurements and analyses, Paul Gooddy for providing access to chemicals, and Bob Jones and John Ford for sample preparation and for allowing me to use space for magnetic separation. I also thank Chris Rowan, Qingsong Liu, Greig Paterson, and Xiang Zhao for many stimulating discussions on palaeomagnetism.

I am grateful for financial support from a Dorothy Hodgkin Postgraduate Award, which was funded by the U.K. Natural Environment Research Council and Hutchison Whampoa Limited. The Royal Society also provided additional travel grants.

I can not end without thanking my wife Yuan and my parents for their support and understanding, and my little son Zhichen for the happiness that he brought in cheering me up when writing this thesis.

Chapter 1

Introduction

1.1. Introduction

The geomagnetic field, which is generated by the motions of conducting fluids in the Earth's deep interior, is not static: both the direction and intensity of the field vary with time. Palaeomagnetism is the study of records of ancient geomagnetic fields. Palaeomagnetism has made fundamental contributions to Earth Science, for example, by enabling establishment and ongoing refinement of global plate tectonics, by providing the geomagnetic polarity timescale for quantitative analysis of a wide range of geological processes, and by providing an understanding of the Earth's magnetic field and deep-Earth dynamo processes. Unravelling past field variations is possible because terrestrial magnetic minerals in rocks and sediments can fossilize a record of the ancient magnetic field and can retain stable magnetizations over geological time scales.

Rock magnetism is the study of the magnetic properties of magnetic minerals in rocks, sediments, soils, and organisms. It underpins our understanding of how magnetic grains record the directions and intensities of ancient magnetic fields and a wide range of geological and environmental processes (e.g., Nagata, 1961; Dunlop and Özdemir, 1997). While palaeomagnetism reveals the history of the geomagnetic field, rock magnetism explains how magnetic minerals record the ambient field. A small number of fundamental magnetic parameters control the magnetic properties of a magnetic mineral and therefore dictate how well a mineral records the geomagnetic field. A detailed understanding of the recording fidelity of magnetic minerals can only be properly understood by determining their fundamental magnetic properties. In contrast to magnetite (Fe_3O_4) and other terrestrial magnetic minerals, such as titanomagnetite ($Fe_{3-x}Ti_xO_4$, $0 \leq x \leq 1$), hematite (α-Fe_2O_3), maghemite (γ-Fe_2O_3), goethite (α-FeOOH) and pyrrhotite (Fe_7S_8), which have been known for decades, the fundamental magnetic properties for the ferrimagnetic iron sulphide mineral, greigite (Fe_3S_4), remain unknown.

Greigite is a strongly magnetic rock-forming mineral. Doss (1912a, b) had postulated the existence of a magnetic iron sulphide that was different from pyrrhotite and named it melnikovite. This name was often considered to be synonymous for greigite by mineralogists (e.g., Lepp, 1957; Gruzdev et al., 1972; Lein et al., 1978). Yamaguchi and Katsurai (1960) had previously synthesized a magnetic iron sulphide Fe_3S_4 in the laboratory, which was later confirmed to be greigite (Uda, 1965). Despite this earlier work, greigite was only formally named in 1964, when it was identified in

Miocene lake sediments from California by Skinner et al. (1964), who determined the precise composition of greigite and named the newly identified mineral in honour of Dr. J.W. Greig of the Pennsylvania State University. Immediately after its discovery, greigite attracted wide interest in chemistry (e.g., Uda, 1965; Morice et al., 1969; Yamaguchi and Wada, 1969; Vaughan and Ridout, 1971; Nakazawa and Sakaguchi, 1972; Goodenough, 1978), physics (e.g., Coey et al., 1970; Yamaguchi and Wada, 1970; Spender et al., 1972), material science (Nakazawa et al., 1973) and earth science (e.g., Radusinović, 1966; Gruzdev et al., 1972; Lein et al., 1978; Vaughan and Craig, 1978).

For a long time after it was discovered, greigite was considered to be a rare mineral that occurs only in modern sedimentary environments. This is because greigite is metastable and is expected to fully react to form pyrite (FeS_2) (e.g., Berner, 1984). On the basis of geochemical predictions, greigite should not persist in the geological record (e.g., Berner, 1984), which would make it palaeomagnetically unimportant. This assumption has been repeatedly demonstrated to be incorrect. Greigite has attracted renewed consideration since it was rediscovered in sediments by Snowball and Thompson (1988). In the last two decades, greigite has been increasingly identified in anoxic marine and lacustrine sedimentary environments (e.g., Snowball and Thompson, 1988, 1990; Hilton, 1990; Krs et al., 1990; Snowball, 1991; Tric et al., 1991; Horng et al., 1992a, b, 1998; Roberts and Turner, 1993; Reynolds et al., 1994; Florindo and Sagnotti, 1995; Jelinowska et al., 1995; Housen and Musgrave, 1996; Roberts et al., 1996; Jelinowska et al., 1998; Sagnotti and Winker, 1999; Jiang et al., 2001; Liu et al., 2004; Rowan and Roberts, 2005, 2006; Frank et al., 2007; Babzinski et al., 2007; Ron et al., 2007; Vasiliev et al., 2007; Fu et al., 2008; Rowan et al., 2009). In some cases, greigite has been the only magnetic mineral identified over stratigraphic thicknesses of hundreds of metres and in outcrops that cover hundreds of km^2, as found in Taiwan, Italy, New Zealand, Hungary, Romania and Israel. More widespread identification of greigite is largely due to the sensitivity of modern magnetic analyses and developments of rock-magnetic criteria for identifying greigite (e.g., Snowball and Thompson, 1990; Roberts, 1995; Dekkers and Schoonen, 1996; Torii et al., 1996; Sagnotti and Winkler, 1999; Dekkers et al., 2000; Rowan and Roberts, 2006). Pyrite is ubiquitous in sediments and rocks that have undergone reductive diagenesis under sulphate-reducing conditions (Berner, 1984). Greigite, as a common precursor to pyrite (e.g., Benning et al., 2000; Hunger and Benning, 2007), will therefore have been present at some point in time within the majority of the world's muds and mudstones. Even geochemically insignificant traces of greigite can retain a detectable and important palaeomagnetic signal. Kao et al. (2004) demonstrated that widespread greigite preservation is likely if abundant reactive iron is available to react with sulphide during pyritization reactions. If organic carbon supply is diluted by terrigenous sediment and abundant reactive iron exhausts the available sulphide supplied by anaerobic decomposition of the organic matter, pyritization will be arrested and the intermediate reaction product, greigite, will be preserved. Preservation of greigite therefore depends on the balance between organic carbon supply, sulphide production and reactive iron concentration. Greigite will not always be preserved in significant concentrations. Nevertheless, it is now recognized as a commonly occurring terrestrial magnetic mineral. Its presence within sedimentary sequences can significantly affect palaeomagnetic and environmental magnetic records. This makes it crucial to determine the fundamental magnetic parameters for greigite.

1.2. Greigite formation in natural environments

Greigite forms authigenically in sulphate-reducing sedimentary diagenetic environments as a precursor to pyrite in association with bacterial degradation of organic matter (e.g., Berner, 1984; Wang and Morse, 1996; Wilkin and Barnes, 1997). In the chemical reaction process, bacteria reduce sulphate $\left(SO_4^{2-}\right)$ to enable decomposition of organic matter to release sulphide (H_2S or HS^-), which reacts with detrital iron-bearing minerals to produce elevated dissolved iron concentrations in the sedimentary pore waters (Canfield and Berner, 1987; Canfield et al., 1992). The dissolved iron and sulphide then react to form pyrite via intermediate phases, such as greigite (Fig. 1.1). Greigite can grow rapidly as a precursor to pyrite in the laboratory (e.g., Wilkin and Barnes, 1997; Benning et al., 2000), as well as in natural environments (e.g., Pye et al., 1981; Raiswell, 1997; Reynolds et al., 1999). In addition to the classical view of early greigite formation as a precursor of pyrite through a variety of geochemical pathways during steady state early diagenesis (e.g., Schoonen and Barnes, 1991; Wang and Morse, 1996; Wilkin and Barnes, 1997; Benning et al., 2000), neoformed greigite can grow at any time during diagenesis when sulphide and reactive iron are present (Roberts and Weaver, 2005). Such remagnetizations of greigite-bearing sediments commonly occur in association with formation and migration of gas hydrates in sedimentary environments (Larrasoaña et al., 2007). Greigite therefore has potential as a tracer for the former presence of hydrates within a sedimentary sequence (Housen and Musgrave, 1996; Enkin et al., 2007; Larrasoaña et al., 2007). These studies demonstrate the potential palaeomagnetic complexity associated with sedimentary greigite formation.

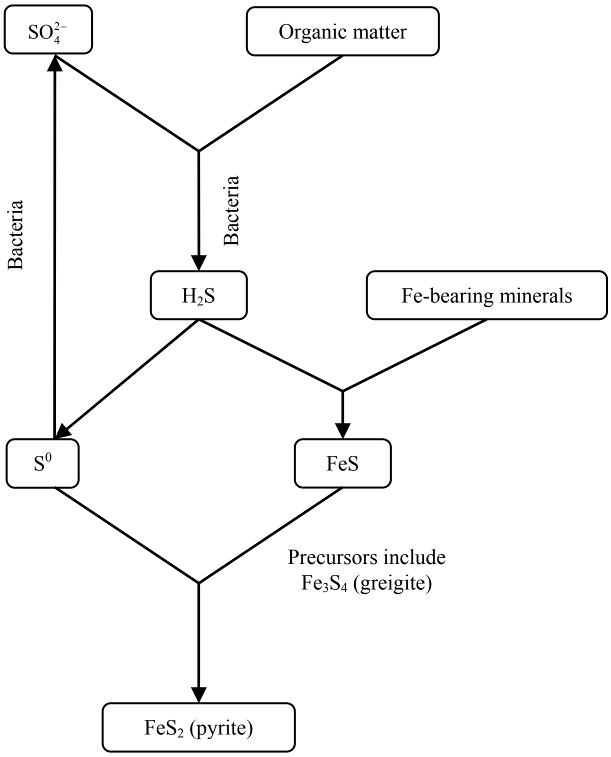

Figure 1.1. Illustration of pyritization reactions in which sedimentary pyrite forms, after Berner (1984). Greigite usually forms in sulphate-reducing diagenetic sedimentary environments as a precursor to pyrite.

In addition to inorganic formation of sedimentary greigite, magnetotactic bacteria that produce greigite magnetosomes also occur widely in modern anoxic marine environments (e.g., Farina et al., 1990; Mann et al., 1990; Heywood et al., 1991; Bazylinski et al., 1993, 1995; Pósfai et al., 1998a, b; Lins et al., 2007) and have been recently also found as magnetofossils (Vasiliev et al., 2008). These magnetotactic bacteria mineralize intracellular magnetosomes, which are membrane-enclosed, single domain (SD) magnetic particles that consist of either magnetite or greigite. Magnetosomes are arranged in chains along the symmetry axis of bacterial cells. The ambient magnetic field exerts a torque on the permanent magnetic dipole of the magnetic chains in magnetotactic bacterial cells. The force allows the bacterium to be oriented and to move along the magnetic field direction – a phenomenon referred to as magnetotaxis. Biogenic greigite can contribute to the remanent magnetization of sediments through preservation of magnetosomes as fossils after the death of magnetotactic bacteria (e.g., Snowball, 1991; Kasama et al., 2006; Vasiliev et al., 2008). Biogenic greigite has also been identified in soils (e.g., Fassbinder and Stanjek, 1994).

1.3. Recording of the geomagnetic field by sedimentary greigite

Sedimentary greigite records the ambient geomagnetic field when it authigenically grows through the SD blocking volume, which creates a chemical remanent magnetization (CRM). Greigite would normally be expected to form shortly after deposition, during early diagenetic sulphate reduction. The CRM acquired by greigite should therefore provide a reliable syn-depositional palaeomagnetic record (e.g., Tric et al., 1991; Roberts and Turner, 1993). In rapidly deposited sediments, the zone of sulphate reduction would be so close to the sediment-water interface that such a magnetization would be temporally indistinguishable from a detrital remanent magnetization (DRM) carried by magnetite. However, in contrast, several recent studies have identified inconsistent polarity records (e.g., Florindo and Sagnotti, 1995; Horng et al., 1998; Jiang et al., 2001; Sagnotti et al., 2005), which can be attributed to late diagenetic growth or neoformation of greigite (Jiang et al., 2001; Roberts and Weaver, 2005). Greigite can grow at any time during diagenesis when sulphide and reactive iron are present; multiple mechanisms can give rise to this situation via disruption of the diagenetic steady state (Roberts and Weaver, 2005). Detailed studies indicate that paired samples from the same stratigraphic level can record opposite polarities. Jiang et al. (2001) interpreted such ‘contradictory polarities’ to result from greigite growth at different times during diagenesis, with the overall polarity being the weighted vector sum of each individual magnetization acquired at different times. For rocks older than the last geomagnetic reversal at 780 kyr, normal or reversed polarity composite magnetizations could be recorded with neither providing a reliable syn-depositional magnetization. While this hypothesis satisfactorily explains contradictory polarities, other problems cannot be so easily explained. Scanning electron microscope (SEM) observations of sedimentary greigite (e.g., Jiang et al., 2001; Roberts and Weaver, 2005; Roberts et al., 2005; Rowan and Roberts, 2005, 2006; Rowan et al., 2009) demonstrate that greigite commonly grows within framboids and as larger aggregates, with close packing of individual crystals. Such packing gives rise to strong magnetostatic interactions among magnetic particles, which has been verified using first-order reversal curve (FORC) diagrams (e.g., Roberts et al., 2000, 2006; Rowan and Roberts, 2006; Florindo et al., 2007; Vasiliev et al., 2007). This raises the question as to whether palaeomagnetic records carried by greigite are contaminated by recording complexities associated with inter-particle magnetic interaction or whether they reflect real geomagnetic variability. These possibilities can only be properly understood by undertaking modelling of magnetization at the micron scale. To be able to do such modelling, it is crucial to know the fundamental magnetic properties of greigite.

1.4. Magnetic properties of greigite: what is known and what is unknown?

The high sensitivity of modern rock magnetometers has enabled palaeomagnetism to play a crucial role in recognizing that greigite is much more common in sedimentary sequences than is suggested by geochemical expectation, starting with the work of Snowball and Thompson (1988). Numerous partial accounts of the magnetic properties of greigite have been reported since 1988. Comprehensive analyses have not been possible because of the metastable nature of greigite. By analysing the most diverse collection of greigite samples then available, Roberts (1995) concluded that greigite commonly occurs in a stable SD state, that its magnetic properties are controlled by magnetocrystalline anisotropy, that it is thermally unstable at elevated temperatures, and that, unlike magnetite, it has no low-temperature magnetic transition. Thermal instability controls the high temperature magnetic properties of greigite, which precludes determination of the Curie temperature (T_C), which must lie above 322°C (Roberts, 1995). Rowan and Roberts (2006) found that much natural greigite, in addition to occurring in the ideal stable SD state, occurs as ultra-fine particles that are so small that thermal vibrations overcome the magnetic energy so that no stable magnetization can be retained by part of the grain size distribution at room temperature. Such fine particles exhibit superparamagnetic (SP) behaviour. Authigenic formation of greigite tends to produce SP and SD magnetic grain size distributions (Rowan and Roberts, 2006). Natural pseudo-single-domain (PSD) and multi-domain (MD) greigite have not been widely reported in the literature, although isolated examples are known (e.g., Hoffmann, 1992; Moskowitz et al., 1993).

Despite numerous reports of the magnetic properties of greigite, many of its fundamental magnetic properties remain unknown. The crystal structure of greigite has been well determined to have the inverse spinel structure using X-ray diffraction (XRD) (e.g., Skinner et al., 1964; Spender et al., 1972), but its magnetic structure (i.e., how the electron spins are ordered in the crystal and what are the spin states) is not determined. Greigite was assumed to have the same magnetic structure as that of magnetite because of their similar composition. However, the assumed magnetic structure of greigite can not be reconciled with the previously reported low saturation magnetization (M_s) value. Published estimates of M_s should be treated with suspicion because of difficulties in obtaining pure greigite samples. Importantly, there has been no direct experimental determination of the magnetic structure of greigite. Similarly, the electronic structure of greigite (i.e., cation distribution and valence states of iron), is not clear. In addition to doubts about published M_s values, other fundamental magnetic parameters, e.g., the exchange constant, magnetocrystalline anisotropy constants, magnetostriction constants, and the Curie temperature, remain undetermined for greigite. Until recently, we have only had a reasonable knowledge of the magnetic properties of SD and SP greigite. No systematic study of PSD/MD greigite has been reported. There is also no report of the grain-size dependence of magnetic properties for greigite. Understanding the magnetic characteristics and palaeomagnetic recording fidelity of any magnetic mineral also requires knowledge of the critical SD grain-size range, which remains undetermined for greigite. From this brief summary, it is clear that we lack fundamentally important knowledge of the mineral physics and chemistry of greigite, which is crucial for underpinning interpretation of magnetizations carried by greigite in natural environments.

1.5. Thesis objectives

The widespread occurrence of greigite in global geological records, and its importance as a carrier of palaeomagnetic and palaeoenvironmental information, makes it important to understand its fundamental magnetic properties to correctly interpret palaeomagnetic signals carried by greigite. As part of this work, I have investigated the previously unknown fundamental magnetic properties of greigite. The principal objectives of this thesis are summarized as follows.

- To synthesize high quality greigite to enable key questions to be addressed concerning the fundamental magnetic properties of greigite.

- To experimentally determine the fundamental magnetic properties of greigite. The magnetic structure of greigite was investigated using a combination of analyses, including neutron scattering, X-ray magnetic circular dichroism (XMCD), and Mössbauer spectroscopy. A range of fundamental magnetic parameters for greigite, e.g., M_s, T_C and the exchange constant were investigated using magnetic techniques.

- To characterize the rock magnetic behaviour of greigite. The magnetic properties of greigite have been studied in this work for the whole range of domain states across the grain size spectrum from SP to MD behaviour. The grain-size dependence of the magnetic properties of greigite was investigated for the first time. A comprehensive study of the low-temperature magnetic properties of greigite using a range of low-temperature measurement techniques is also presented. The effects of magnetostatic interactions have been assessed using FORC diagrams. The magnetic properties of synthetic and natural greigite samples are compared.

By working with Dr Yan Tang and Prof. Qianwang Chen at the Department of Materials Science and Engineering, University of Science and Technology of China, we have produced highly pure greigite samples in the laboratory using a new hydrothermal synthesis method (Tang et al., 2007). I have also collected natural greigite samples from a range of locations that include eastern New Zealand (Rowan and Roberts, 2005, 2006), the Brown coal basin of west Bohemia in the Czech Republic (Krs et al., 1990; Hoffmann, 1992), the upper Pliocene Valle Ricca section near Rome in Italy (Florindo and Sagnotti, 1995; van Dongen et al., 2007) and southwestern Taiwan (Jiang et al., 2001). This unique collection of synthetic and natural greigite samples is ideal for investigating the fundamental magnetic properties of greigite.

1.6. Thesis outline

Basic theories of magnetism and the experimental methods used in this study are described in Chapters 2 and 3, respectively. The main results are presented in Chapters 4 to 7. A first study of the magnetic characteristics of PSD/MD greigite is presented in Chapter 4, which is also the first study of the grain-size dependent magnetic properties of greigite (this work has been published in *Geophysical Research Letters*). A detailed description of the new hydrothermal method for synthesizing greigite and the mineralogical and magnetic characteristics of the synthetic greigite samples are presented in Chapter 5. This chapter also provides the first robust determination of a range of fundamental magnetic parameters for greigite, including the first accurate measurements of M_s and the exchange constant (this work has been published in the *Journal of Geophysical Research – Solid Earth*). In Chapter 6, determination of the magnetic structure of greigite, using neutron powder diffraction and polarized neutron diffraction, is presented. This work reveals the spin arrangement and clarifies the origin of magnetism in greigite (this work has been accepted for publication in the *Journal of Geophysical Research – Solid Earth*). In Chapter 7, a comprehensive study of the magnetic behaviour of greigite below room temperature is presented, which demonstrates the usefulness of low-temperature rock magnetometry to study greigite in sediments (this work has been published in *Geochemistry, Geophysics, Geosystems*). Chapter 8 comprises the overall conclusions of this study and provides suggestions for future work. Details concerning greigite synthesis and XMCD results are presented in the Appendix.

Chapter 2

Theory of magnetism

In this chapter, the textbooks of Moskowitz (1991), Butler (1992), and Dunlop and Özdemir (1997) provide useful general references in addition to the explicit citations.

2.1. Introduction

In order to understand the fundamental magnetic properties of greigite, a detailed description of the principles of magnetism is needed. This chapter describes the basic theory of magnetism that relates to this study. First, a microscopic view of the origin of magnetism at atomic scales and the physical principles of magnetism are presented, followed by a description of the different types of magnetic materials. To understand the exchange constant, it is useful to have a basic knowledge of the spin wave in magnetically ordered materials, as well as Bloch's magnetization Law. These subjects are therefore discussed, followed by a brief summary of some macroscopic magnetic properties of rocks, such as magnetic anisotropy, magnetic domain states, and types of remanent magnetization.

2.2. Origin of magnetism

Magnetism has been known to humans from ancient times. It was firstly described by the ancient Greek philosophers and Chinese, who found that lodestone, the mineral magnetite, is strongly magnetic. In the 2nd century BC, the Chinese invented the first compass, which comprises a magnetic lodestone rotating on a bronze plate. The English physician, William Gilbert, who is regarded as the father of electricity and magnetism, published the famous book '*De Magnete*' in 1600, which significantly improved our knowledge of magnetism. He was the first to describe the similarities between the field lines of a bar lodestone and the geomagnetic field. The modern theory of magnetism was developed through the pioneering work of Coulomb, Oersted, Faraday, and Maxwell. Coulomb found that magnetic forces follow similar laws as electric forces. Oersted discovered that an electric current produces a magnetic field. Faraday discovered the phenomenon of electromagnetic induction, while Maxwell formulated the theory of electromagnetism in terms of his now famous equations. This classic theory of magnetism was a macroscopic description. It was the discovery of the electron by Thomson in the late nineteenth century and the subsequent development of Bohr's atomic theory that enabled development of a microscopic explanation of magnetism. A brief history of magnetism, from the early discovery of magnetic materials up to quantum theory, is given by Mattis (1981).

Magnetism is produced by a circular current or a magnetic dipole. The magnetic moment **M** is defined as the rotational force experienced by the electron in a magnetic field of unit strength acting perpendicular to its magnetic axis. In a microscopic view at the atomic or sub-atomic level, magnetism originates from two types of electron motions in atoms or ions – one is the orbital motion of electrons around a nucleus, and the other is the spin of electrons (Cracknell, 1975). The magnetic moment associated with the orbital motion of an electron in an atom is:

$$\mathbf{M_L} = -(e/2m_e)\mathbf{L}, \tag{2.1}$$

where **L** is the angular momentum of the electron, e is the charge of the electron, and m_e is the mass of the electron. The constant, $e/2m_e$, is referred to as the gyromagnetic ratio. The magnetic moment in the z direction is:

$$(e/2m_e)L_z = (e\hbar/2m_e)m_l = \mu_B m_l, \tag{2.2}$$

where $\hbar$ is the Planck constant, μ_B is called the Bohr magneton, and m_l is the magnetic quantum number. The total angular momentum is zero for a complete shell of electrons in an atom or ion. Only incomplete shells of electrons contribute to the orbital magnetic moment. The spins of electrons will also contribute to the magnetic moment of an atom or ion. The algebraic properties of the spin angular momentum operator **S** results in eigenvalues of S^2 to be $s(s + 1)\hbar^2$ (where s is the spin quantum number associated with the spin angular momentum of an electron). Only a value of ½ is allowed for s. The z component of the spin angular momentum is $S_z = m_s\hbar$, where $m_s = \pm 1/2$, is the secondary spin quantum number. The magnetic moment associated with the spin angular momentum is:

$$\mathbf{M_S} = -2(e/2m_e)\mathbf{S}. \tag{2.3}$$

Only unpaired electrons in an atom or ion contribute to the total spin magnetic moment. The total magnetic moment from a combination of orbital and spin motion is produced through spin-orbital interaction:

$$\mathbf{M_J} = -g(e/2m_e)\mathbf{J}, \tag{2.4}$$

where **J** is the total angular momentum operator, and g is the Landé g factor.

Magnetization **M** is the magnetic moment per unit volume or per unit mass. The magnetic field **H** is a vector field that permeates space and that can exert a magnetic force on moving electric charges and on magnetic dipoles. When placed in a magnetic field, magnetic dipoles tend to align their axes to be parallel with the magnetic field.

The potential energy of alignment of magnetic moments with the applied magnetic field is:

$$E = -\,\mathbf{M}\cdot\mathbf{H} = -\,MH\cos\theta, \tag{2.5}$$

where θ is the angle between **M** and **H**. In the SI system, the magnetic induction **B** is:

$$\mathbf{B} = \mu_0\,(\mathbf{H} + \mathbf{M}), \tag{2.6}$$

where $\mu_0 = 4\pi \times 10$ Henries/m is the permeability of free space. The magnetic susceptibility χ is the ratio of the magnetization to the applied magnetic field:

$$\chi = \mathbf{M}/\mathbf{H}, \tag{2.7}$$

where χ can be regarded as the ability of a magnetic material to become magnetized. In Equation 2.7, χ is a scalar, which indicates that **M** is parallel to **H**. For magnetically anisotropic materials, the magnetic susceptibility is expressed as a tensor $\boldsymbol{\chi}$.

2.3. Types of magnetic materials

2.3.1. Diamagnetism

Diamagnetism occurs in materials that develop a magnetic moment antiparallel to the direction of an applied field (Fig. 2.1a). Diamagnetism arises from the orbital motion of electrons, where the tiny atomic current loop produces a magnetic field that aligns opposite to the applied field according to Lenz’s Law. All materials exhibit diamagnetism. Diamagnetism is generally a weak effect. Diamagnetic materials have negative susceptibility because of their repulsive nature with respect to the applied magnetic field. There are no permanent dipole moments in diamagnetic materials.

2.3.2. Paramagnetism

Unlike diamagnetic materials, paramagnetic materials have permanent magnetic moments of individual atoms, ions, or molecules, which originate from the spins of unpaired electrons or the orbital motions of electrons, or a combination of both effects. The magnetic moment do not interact, therefore the moments are randomly oriented due to thermal motion at zero magnetic field (Fig. 2.1b). In the presence of an external magnetic field, these randomly oriented magnetic moments tend to align parallel to the

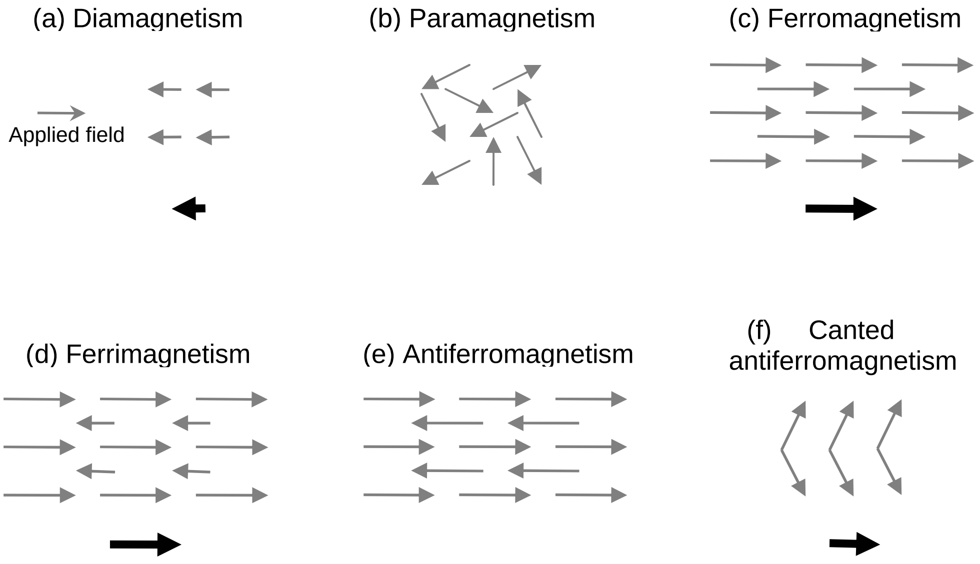

Figure 2.1. Illustration of the spin structures of different types of magnetic materials. Black arrows indicate the net magnetization. The net magnetization is zero in zero field in (b) and (e).

magnetic field. The magnetization of paramagnetic materials is proportional to the applied magnetic field. After removing the applied field, the total magnetization drops to zero because of thermal fluctuation that causes the spins to become randomly oriented and therefore to have no remanence. Langevin developed a simple theory of paramagnetic magnetization for an assembly of atoms. In a magnetic field, the individual magnetic moments will align parallel to the field while this alignment is opposed by thermal fluctuations. This dynamic process will have an equilibrium state. Using Boltzmann statistics, the magnetization **M** at the equilibrum state is:

$$\frac{\boldsymbol{M}}{\boldsymbol{M}_s}=\frac{\int_0^{\pi}\exp\left(\boldsymbol{mB}\cos\theta/kT\right)\cos\theta\sin\theta d\theta}{\int_0^{\pi}\exp\left(\boldsymbol{mB}\cos\theta/kT\right)\sin\theta d\theta}, \tag{2.8}$$

where k is the Boltzmann constant, θ is the angle between the individual magnetic moment $\boldsymbol{m}$ and the applied field $\boldsymbol{B}$, and T is temperature. By replacing $y = \boldsymbol{mB}/kT$ and $x = \cos\theta$, Equation 2.8 is conventionally rewritten as:

$$\frac{\boldsymbol{M}}{\boldsymbol{M}_s}=\frac{\int_0^{\pi}xe^{xy}dx}{\int_0^{\pi}e^{xy}dx}=\left(\coth y-1/y\right)=L\left(y\right), \tag{2.9}$$

where *L*(*y*) is called the Langevin function. The paramagnetic susceptibility χ_p is then:

$$\chi_p = \frac{M}{H} = \frac{M_s L(y)}{H} \approx \frac{\mu_0 n m^2}{3kT} = \frac{\mu_0 {M_s}^2}{3nkT} = \frac{C}{T}, \tag{2.10}$$

where *C* is a constant. This is Curie's Law, which describes the temperature dependence of paramagnetic susceptibility. A precise description of paramagnetic susceptibility requires use of quantum mechanics, which is, however, beyond the scope of this thesis. The simple Langevin theory described above predicts the principal properties of paramagnetism.

2.3.3. Ferromagnetism, antiferromagnetism and ferrimagnetism

In addition to an induced magnetization that is produced in the presence of an applied field magnetic field, some materials also have a remanent magnetization that persists after removal of the applied field. These substances are ferromagnetic materials. Ferromagnetic substances have a large permanent magnetic moment in the absence of an external magnetic field, unlike diamagnetic and paramagnetic substances. In ferromagnetic materials, the magnetic moments of the individual atoms, ions or molecules are spontaneously aligned parallel to some particular direction through the exchange interaction between the neighbouring spins – a quantum mechanical effect of increasing or decreasing the energy of two or more fermions when their wave functions overlap. That is, the magnetic moments are long-range ordered (Fig. 2.1c).

Ferrimagnetism and antiferromagnetism were proposed by Néel (1948). In ferrimagnets, the magnetic moments of the atoms in different sublattices are antiparallel coupled. However, the opposing moments are not equal, which results in a net magnetization (Fig. 2.1d). Magnetite is a classical example of a ferrimagnet. In magnetite, the *A* sublattice contains Fe^{3+}, while the *B* sublattice contains both Fe^{2+} and Fe^{3+}. The magnetic moments on the two sites have antiparallel ordering. In antiferromagnets, the magnetic moments are antiparallel coupled and the opposing moments are identical (Fig. 2.1e), which results in a zero net magnetization. In some antiferromagnets, the opposing moments are not completely antiparallel, which gives rise to a canted antiferromagnetism and produces a net magnetization (Fig. 2.1f). Hematite is the prime example of a canted antiferromagnet.

The spontaneous magnetization describes the appearance of an ordered spin state at zero applied magnetic field for ferro-/ferri-/antiferromagnets. The spontaneous magnetization M_s is defined as the net magnetization within one domain. In ferrimagnets, M_s corresponds to the net magnetization of the sublattice magnetizations. M_s depends on temperature. At absolute zero, the magnetic moments align perfectly because of the absence of thermal energy. As temperature increases, M_s will decrease due to increasing thermal energy. Thermal energy will eventually overcome the exchange interaction and randomize the magnetic moments so that M_s disappears at a critical temperature – the Curie temperature for ferro-/ferrimagnets – and at the Néel temperature for antiferromagnets, respectively. Above T_C, ferro-/ferrimagnetic materials transfer to the disordered paramagnetic state. Below T_C, the spontaneous magnetization follows approximately the Brillouin function:

$$M_s(T) = N_A g s \mu_B B(\eta) = M_s(0) B(\eta), \tag{2.11}$$

where $B(\eta) = \frac{2s+1}{2s}\coth\left[\left(\frac{2s+1}{2}\right)\eta\right] - \frac{1}{2s}\coth\left(\frac{1}{2}\eta\right)$ is the Brillouin function, with $\eta = \frac{g\mu_B H}{kT}$. N_A is the total number of magnetic moments, g is the Landé g-factor as described above, and $M_s(0)$ is the spontaneous magnetization at zero temperature.

For ferrimagnets, the spontaneous magnetization is given by the sum of the sublattice magnetizations M_A and M_B. Different variations of temperature dependence of $M_A(T)$ and $M_B(T)$ give rise to several types of ferrimagnetism. If the exchange interaction is dominated by the AB interactions, the $M_A(T)$ curve is similar to the $M_B(T)$ curve. This gives rise to Q-type ferrimagnetism (Fig. 2.2a), which is similar to the case for ferromagnets. R-type ferrimagnetism (Fig. 2.2b) is found in many ferrites, such as $NiFe_2O_4$, where one of the sublattice curves undergoes little change at low temperatures. $M_s(T)$ curves for P-type ferrimagnets (Fig. 2.2c) have a hump, which results from different $M_A(T)$ and $M_B(T)$ variations. N-type ferrimagnets (Fig. 2.2d), such as chromite, originate from extremely different $M_A(T)$ and $M_B(T)$ curves, so that M_s changes sign below T_C. This produces ‘self-reversal’ during thermal treatment.

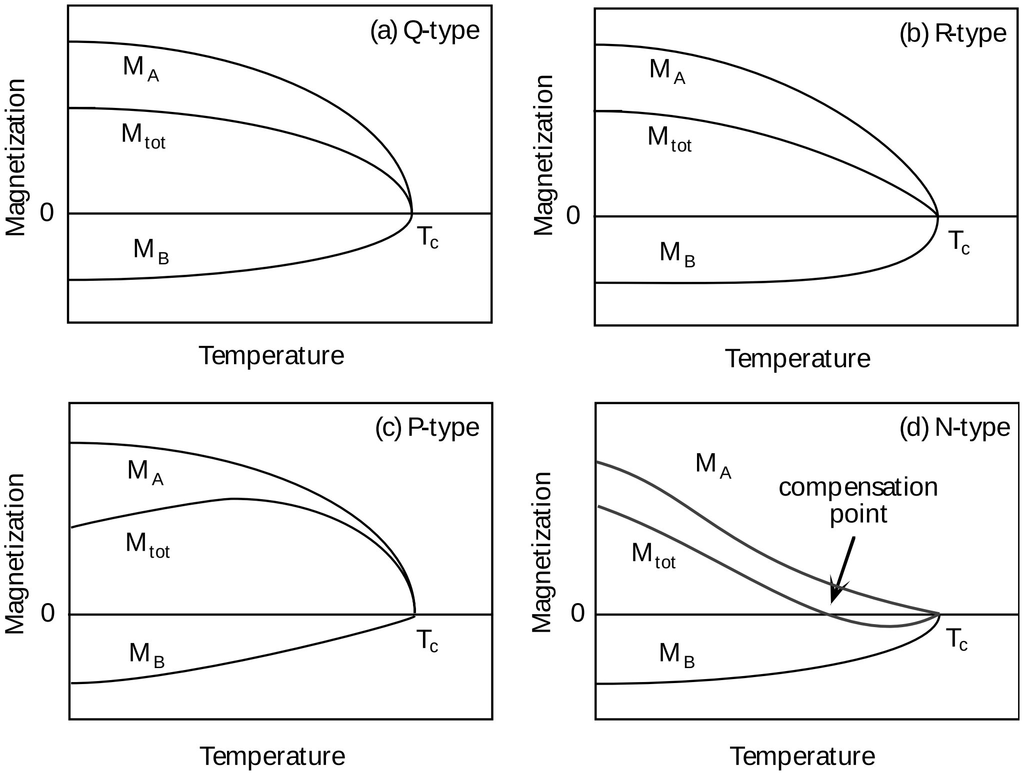

Figure 2.2. Types of ferrimagnets with different temperature dependences resulting from different temperature variations of the sublattice magnetizations, after Dunlop and Özdemir (1997).

2.4. Spin waves

2.4.1. Phonons and magnons

In crystalline materials, atoms are not bound in place, but oscillate around their equilibrium positions. Because of interactions among neighbouring atoms, the synchronized vibrations of the whole group of atoms produce wave-like behaviour. A simple treatment of the lattice vibration using classical mechanics produces normal modes, where each part of the lattice oscillates with the same frequency. This phenomenon is referred to as the lattice vibration. The normal modes have wave-like behaviour, but no particle-like properties. A quantum mechanical treatment of the vibrational motion defines a phonon, which is a quantized mode of the lattice vibration within crystalline solids. A phonon is a quasiparticle, which does not exist but is produced to simplify the quantum mechanical many-body problem in systems of interacting particles. The macroscopic properties of condensed matter, such as thermal properties and electrical conductivity, can therefore be treated using phonons.

The classical Heisenberg model is used in statistical physics to model ferromagnetism and other phenomena. In this model, the Hamiltonian of the ferromagnetic system is:

$$H = -\sum_{i,j} J_{ij} \vec{S}_i \cdot \vec{S}_j \,, \tag{2.12}$$

where J_{ij} is the exchange coupling between spins, with $J_{ij} = J$, if i and j are neighbours; otherwise $J_{ij} = 0$. The effective exchange constant is defined as $A = J_{ij} S^2/a$, where S is the spin, and a is the spacing between spins. Due to exchange coupling, the eigenmodes of the spin system possess in the magnetic lattice a wave-like character. For magnetically ordered materials, in addition to the lattice vibration, there is a further degree of freedom – the reorientation of the spins away from the uniform alignment direction in the magnetic lattice. As an analogy to the lattice vibration, the interaction between neighbouring spins will also produce wave-like behaviour, which is referred to as a spin wave (Fig. 2.3). The magnon is defined by the quantum mechanical treatment of the spin motion. A magnon, like a phonon, is also a quasiparticle. Magnons are boson modes of the spin lattice. The complex system of the magnetic lattice is then treated as an aggregation of magnons, where the total energy of magnons describes the energy of the magnetic lattice. A comprehensive description of the spin wave can be found in Keffer (1966).

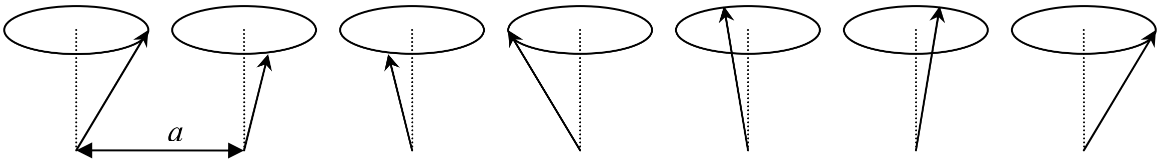

Figure 2.3. Sketch of the spin wave in ferromagnets. where a represents the lattice parameter. This is the simplest case of a linear one-dimensional chain. All the spins have a fixed direction, while there is a constant angular difference between neighbouring spins.

Each magnon has a definite precession frequency ω and wavelength λ, and a wave vector $\boldsymbol{k}$ in the magnetic crystal. As in the case of the phonon, the dispersion relation of spin waves, that is the relationship between ω and k, can be deduced by searching for the wave-like solutions of the motion equations. A semiclassical treatment of the dispersion relation is described below. A treatment using quantum mechanics is provided by Keffer (1966), which is not shown here.

For a ferromagnetic system as shown in Fig. 2.3, the interaction energy u of the spins $\vec{S}$ at position l and $l+1$ is:

$$u(l,l+1) = -J\vec{S}(l)\cdot\vec{S}(l+1)\,. \tag{2.13}$$

The torque between the two spins is:

$$\vec{T}(l,l+1) = J\vec{S}(l)\times\vec{S}(l+1)\,. \tag{2.14}$$

The equation of motion is:

$$\frac{d}{dt}\vec{S}(l) = J(\vec{S}(l)\times\vec{S}(l-1)+\vec{S}(l)\times\vec{S}(l+1))\,. \tag{2.15}$$

In rectangular coordinates, this motion equation gives three scalar equations in the x, y, and z directions. Supposing the precession axis is in the z direction:

$$\vec{S}_x(l),\vec{S}_y(l) << \vec{S}_z(l) \approx S\,. \tag{2.16}$$

Considering a wave-like solution of the spins:

$$\begin{cases} S_x(l) = A\exp(-i\omega t + ikla) \\ S_y(l) = B\exp(-i\omega t + ikla)\,. \\ S_z(l) \approx S \end{cases} \tag{2.17}$$

Putting these solutions in Equation 2.17 into the motion Equation 2.15 produces linear equations. Setting the secular determinant to zero gives the dispersion relation:

$$\omega = \pm 2JS(1-\cos ka)\,. \tag{2.18}$$

From Equation 2.18, ω has a periodic dependence on k with a period of $2\pi/a$. Restricting k to the first Brillouin zone, the Taylor expansion of the cosine term gives a parabolic dispersion relation:

$$\hbar\omega = Dk^2, \tag{2.19}$$

where D is the spin wave stiffness, which describes the ‘strength’ of spin waves. Several techniques can be applied to directly observe the spin waves, e.g., inelastic neutron scattering, Brillouin scattering and spin-wave resonance.

2.4.2. Bloch’s Law

Bloch's Law describes the temperature dependence of the spontaneous magnetization. The spontaneous magnetization decreases as temperature increases by increasing excitation of spin waves. Increasing thermal excitation of spin waves reduces the spontaneous magnetization from the maximum of the ground state at zero K. Using Bose-Einstein statistics, the average number of magnons is:

$$\langle n_i \rangle = \frac{1}{\exp(h\omega_i / 2\pi k_B T) - 1}, \tag{2.20}$$

where ω_i is the frequency of magnon i, h is Planck’s constant, k_B is the Boltzmann constant, and T is temperature. If the total spin is changed by $h/2\pi$, the change associated with the magnetic moment is $2\mu_B$. The magnetization at temperature T is therefore:

$$M(T) = M(0) - \Delta M(T) = M(0) - 2\mu_B \sum_{\vec{k}_i} \langle n_i \rangle (T), \tag{2.21}$$

where $M(0)$ represents the magnetization at absolute zero temperature. Transforming the sum above into an integral gives:

$$\sum_{\vec{k}_i} \langle n_i \rangle (T) = \int \frac{D(\omega)}{\exp(h\omega / 2\pi k_B T) - 1} d\omega, \tag{2.22}$$

where $D(\omega)$ is the density of levels in the frequency space and is given by $D(\omega)d\omega = \frac{V}{2\pi^2} k^2 dk$. Replacing $x = \frac{h\omega}{2\pi k_B T}$ in Equation 2.22 gives:

$$\sum_{\vec{k}_i} \langle n_i \rangle (T) = \frac{V}{4\pi^2 (2\pi D / h)^{3/2}} T^{3/2} \int_0^{h\omega_{\max} / 2\pi k_B T} \frac{x^{1/2}}{e^x - 1} dx, \tag{2.23}$$

At low temperatures, where $T \rightarrow 0$, the integral in Equation 2.23 is replaced by its limiting value. Equation 2.21 is then transformed to:

$$M(T) = M(0) - AT^{3/2}, \tag{2.24}$$

where A is a coefficient, which is related to the spin wave stiffness D. This is the Bloch $T^{3/2}$ magnetization law. As temperature increases, the spin wave excitation causes the spontaneous magnetization to decrease. By measuring the temperature dependence of magnetization at low temperatures, the spin wave stiffness D can be determined, from which the exchange constant can be derived.

2.5. Magnetic anisotropy

Many magnetic materials have preferred magnetization directions. These directions are referred to as the magnetic 'easy' direction. By contrast, some directions of magnetization are referred to as the 'hard' direction. Magnetic anisotropy is defined as the dependence of the internal energy on the direction of the spontaneous magnetization. Crystal anisotropy is produced by the crystal symmetry of magnetic materials. The simplest form of crystal anisotropy is the uniaxial anisotropy, which has only one easy direction of magnetization. The uniaxial anisotropy energy is rotationally symmetric with respect to the easy axis and depends on the relative orientation of magnetization. The expansion series of the uniaxial anisotropy has the form:

$$E = K_0 + K_1 \sin^2\theta + K_2 \sin^4\theta + K_3 \sin^6\theta + \ldots, \tag{2.25}$$

where θ is the angle between the magnetization and the easy axis, and K_1, K_2, K_3 … are the anisotropy constants.

Magnetocrystalline anisotropy is the energy necessary to deflect the magnetization in a single crystal from the easy direction to the hard direction. The origin of magnetocrystalline anisotropy arises from the spin-orbit interaction, which is the weak coupling between *d*-electron spins and the crystal lattice. The spins have more freedom to orient along the applied magnetic field, but the orbital moments may still remain coupled to the crystal lattice. The orientation of magnetization with respect to the crystal axes determines the magnetic anisotropy energy. For materials with cubic symmetry, the anisotropy energy can be expressed in terms of the direction cosines as a polynomial expansion series:

$$E = K_1\left(\alpha_1^2\alpha_2^2 + \alpha_2^2\alpha_3^2 + \alpha_1^2\alpha_3^2\right) + K_2(\alpha_1^2\alpha_2^2\alpha_3^2) + \ldots, \tag{2.26}$$

where $(\alpha_1, \alpha_2, \alpha_3)$ are the direction cosines of the internal magnetization with respect to the three principle axes of the cube, and K_1 and K_2 are the first- and second-order magnetocrystalline anisotropy constants, respectively. Higher terms can be considered negligible in the series expansion.

Shape anisotropy, which is also known as magnetic dipolar anisotropy, originates from dipolar interaction. Shape anisotropy depends on the shape of the particles, as well as on the saturation magnetization. Magnetized grains have magnetic charges at their surfaces, which produce demagnetizing fields. For an elongated grain, this field is larger along the short axes of magnetization. The long axis is therefore the easy axis of magnetization (Fig. 2.4). A spherical particle will therefore have no shape anisotropy. The shape anisotropy energy is proportional to M_s (i.e., materials with larger M_s exhibit larger shape anisotropy).

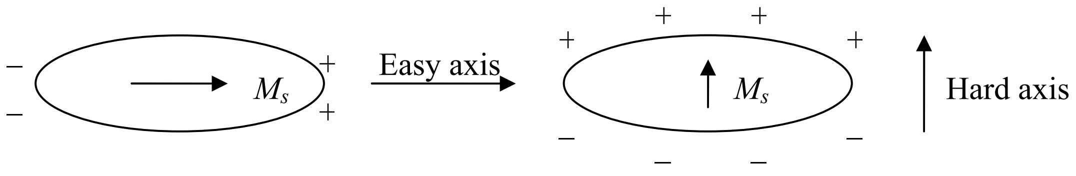

Figure 2.4. Illustration of shape anisotropy. The long axis of the grain is the easy axis of magnetization, after Butler (1992).

The mechanical stress present within magnetic grains will also produce magnetic anisotropy, which is known as magnetostrictive anisotropy. Magnetostrictive anisotropy is an induced anisotropy that originates from the spin-orbit coupling, as is the case for crystal anisotropy. Fundamentally, it is the strain dependence of crystalline anisotropy. The symmetry of the strain determines the magnetostriction anisotropy symmetry. The magnetization process can change the dimension of a magnetic material due to the strain produced by the applied field – a phenomenon referred to as magnetostriction. Conversely, the internal stress within magnetic grains can also change the magnetization.

2.6. Magnetic domain states

In magnetically ordered particles, the total magnetization E_{total} is controlled by various energies:

$$E_{\text{total}} = E_{\text{exchange}} + E_{\text{dipolar}} + E_{\text{anisotropy}} + E_{\text{Zeeman}}, \tag{2.27}$$

where E_{exchange} is the exchange energy, E_{dipolar} is the dipolar energy, $E_{\text{anisotropy}}$ is the anisotropy energy, and E_{Zeeman} is the external energy. The magnetic behaviour is therefore governed by these energies. The magnetization configuration of a magnetic particle will have a minimum E_{total} at any equilibrium state. The magnetic properties will depend on many factors, particularly grain size, which provides variable magnetic behaviour depending on the different magnetic domain state. As grain size increases, the magnetization changes from exhibiting SP, to SD, to PSD, and to MD behaviour.

2.6.1. Single-domain state

SD particles have uniform magnetization throughout the grain. The magnetic domain was postulated by Weiss (1907). He discovered that in ferromagnets, some areas have uniformly oriented moments even in the absence of an applied external field. He proposed that the alignment of the magnetic moments is caused by an internal field – which is referred to as the Weiss mean field. This field is essentially the interaction between neighbouring moments. SD theory was developed by Kittel (1946) and Néel (1949, 1955). Kittel (1946) originally presented a theory for the SD structure of fine ferromagnetic grains and showed how SD particles response to an external magnetic field. This theory predicts that the coercivity of SD particles is determined by the crystalline and shape anisotropies, and is therefore much higher than the coercivity of MD particles (Fig. 2.5).

Theoretical understanding of the stability of SD particles is based on Néel's relaxation Equation (Néel, 1949):

$$\tau = \tau_0 \exp\left(-K_{\text{eff}} V/2kT\right), \tag{2.28}$$

where τ is the relaxation time, τ_0 is the pre-exponential factor corresponding to the resonance relaxation time of the spin system, K_{eff} is the effective anisotropy energy, which has different expression depending on the type of anisotropy, V is grain volume, k is Boltzmann's constant, and T is absolute temperature. The Néel (1949) relaxation

Equation reveals the volume dependence of the relaxation time. τ is small for extremely small particles, whose remanence decays rapidly, but it increases rapidly as the grain size becomes larger. At a critical grain volume, τ is sufficiently long that a stable magnetic remanence is preserved. Thus, in theory, SD grains are highly magnetically stable (Néel, 1955), which has been confirmed in many experiments (e.g., Dunlop and Özdemir, 1997). It is the long relaxation time of SD particles that gives rise to geologically stable magnetizations that makes palaeomagnetism such a useful technique in earth science, and that makes possible the analysis of magnetizations that are stable on billion-year timescales. Hysteresis processes in SD particles are controlled by the rotation of magnetization, which requires relatively large energies. SD grains are therefore magnetically 'hard', and are characterized by high coercivity and remanence. SD grains have a high ratio of saturation remanence to saturation magnetization. For randomly oriented grains, M_{rs}/M_s = 0.5 and 0.87, respectively, for assemblages of grains with single and multiple axes of easy magnetization. This property makes SD grains an ideal recorder of the geomagnetic field, whose remanence can be stable over long geological times.

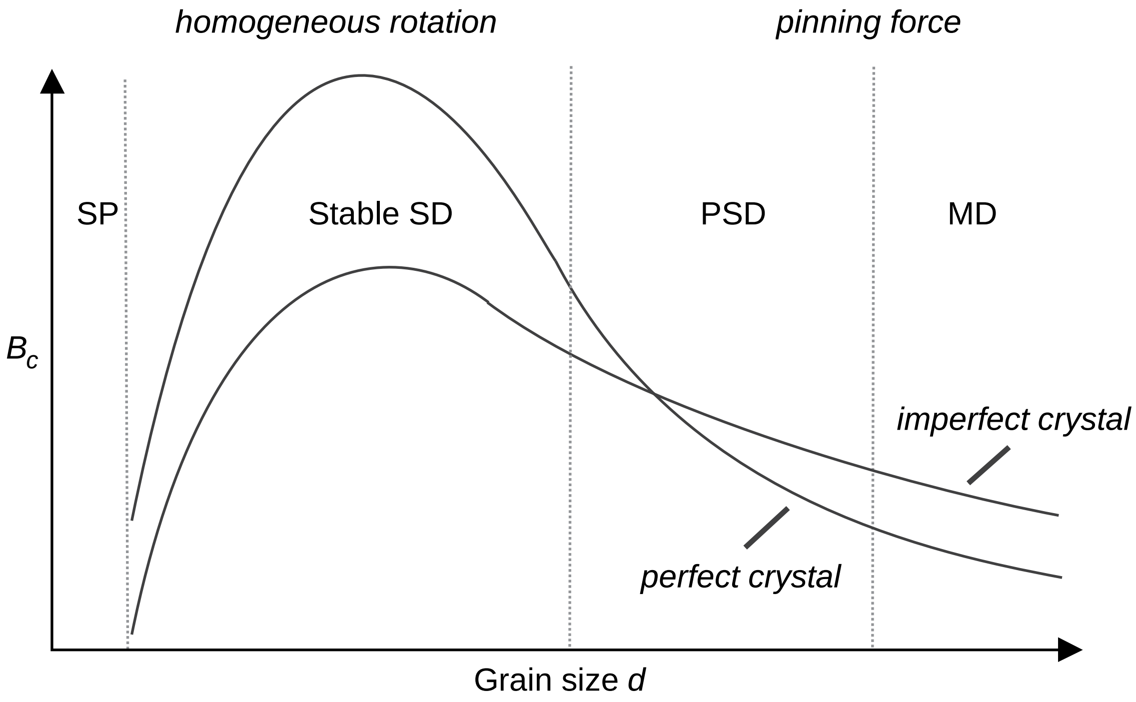

Figure 2.5. Schematic representation of the change in coercivity B_c as a function of grain size d for various domain states, after Kronmüller and Fähnle (2003).

2.6.2. Superparamagnetic state

Néel's relaxation Equation (Equation. 2.28) predicts that the relaxation time τ would become small for small grains. At a critical point, τ is so small that thermal energy overcomes anisotropy energy. At this point, the thermal energy is insufficient to overcome the exchange interaction between neighbouring spins, but it is sufficient to change the direction of magnetization within the entire grain. Thermal fluctuation therefore randomizes the magnetization. This phenomenon is referred to as superparamagnetism. SP particles exhibit similar behaviour as paramagnetic materials, which is why it is called superparamagnetism. SP particles have no remanence. They can only be magnetized in an applied field, which is described by the Langevin function (Equation. 2.9). Essentially, SP particles are SD grains with uniform magnetization, but this magnetization is not stable. In order to distinguish between these types of SD particles, the term stable single domain (SSD) is often used to refer to SD particles with stable magnetization, while SP is used to describe superparamagnetism. However, SD is often used in place of SSD and unstable SD behaviour is referred to as SP behaviour.

2.6.3. Multi-domain state

As a particle becomes larger, the demagnetizing energy (Equation. 2.27) increases significantly due to increasing surface area. At a critical point – the critical SD threshold size – the particle is no longer in a minimum energy state with uniform magnetization. To reduce the demagnetizing energy, and therefore the total energy of the system, the magnetization of the particle will be divided into separate magnetic domains, each with uniform magnetization (Fig. 2.6). Each domain is separated by a domain wall (Fig. 2.6). Such a particle is referred to as a MD grain. MD behaviour was predicted by Landau and Lifschitz (1935) and that concept was later developed by Kittel (1949).

The change in magnetization between adjacent domains is accommodated as magnetic spins rotate within a domain wall (Fig. 2.7). This continuous change of spin orientation within a thin domain wall is favoured because a rapid change of spins is needed to overcome the large exchange energy. Two types of domain wall have been proposed: the Bloch wall and Néel wall (Fig. 2.7). In the Bloch wall, the spins rotate out of the plane of magnetization, while in the Néel wall, the rotation of the spins is confined within the plane of magnetization. A Bloch wall normally nucleates in the centre of a domain structure and a Néel wall normally occurs at the surface of grains because the in-plane rotation is energetically favoured near the grain surface. For a 180° domain wall, the domain wall width δ_w is given by (Kittel, 1949):

$$\delta_w = \pi\sqrt{\frac{A}{K}}, \tag{2.29}$$

where A is the exchange constant, and K represents the magnetic anisotropy. δ_w is controlled by two competing energies: the exchange energy makes the domain wall thicker, while the anisotropy energy makes the domain wall thinner.

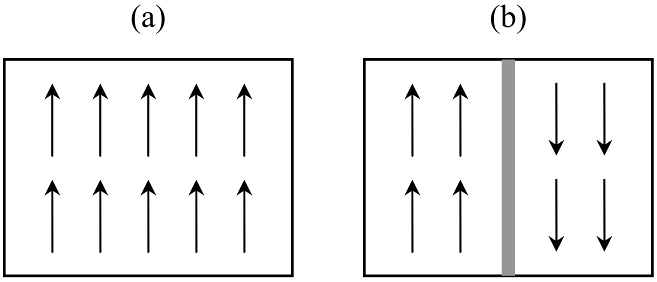

Figure 2.6. Illustration of (a) the SD state, and (b) the MD state. Arrows indicates the direction of magnetization. The shaded area is referred to as a domain wall. For this magnetic particle, the magnetization configuration in (b) is favoured because nucleation of a domain wall reduces the total energy of the particle.

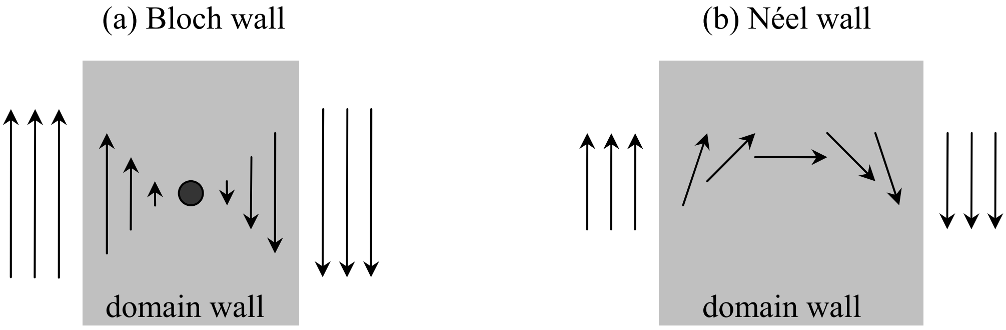

Figure 2.7. Illustration of (a) a Bloch wall, and (b) a Néel wall, after Kronmüller and Fähnle (2003). The Bloch wall continuously rotates out of the plane of magnetization, while the Néel wall continuously rotates within the plane of magnetization.

2.6.4. Pseudo-single-domain state

In theory, MD grains are magnetically unstable. Above the critical SD grain size threshold, where domain walls begin to appear, the saturation remanence should drop sharply. However, experiments demonstrate that there is no sharp boundary between SD and MD grains. There is a grain size interval with intermediate M_{rs}/M_s and coercivity, and with stable remanence. This fraction with stable remanence decreases with increasing grain size. Small MD grains that are magnetically stable are usually referred to as pseudo-single domain grains, as proposed by Stacey (1963). PSD grains contain a small number of domains and can have a substantial magnetic moment. Micromagnetic modelling predicts that PSD grains have non-uniform magnetizations, such as vortex structures (e.g., Williams and Dunlop, 1989). PSD grains can carry stable remanences over geological timescales, and can therefore carry meaningful palaeomagnetic information. For magnetite, the PSD size interval is approximately 1-10 μm. PSD grains are abundant in most igneous and sedimentary rocks that contain magnetite and titanomagnetite.

2.7. Types of remanence

The most important characteristic of ferro-/ferri-/canted antiferro-magnetic materials is that they can retain a magnetization after removal of an applied field. It is this remanent magnetization that enables magnetic minerals to record the ancient geomagnetic field. The remanent magnetization carried by magnetic minerals can be classified into different types depending on the mechanisms of magnetic recording. These types of remanence are briefly described below following the textbooks of Butler (1992) and Dunlop and Özdemir (1997).

2.7.1. Thermoremanent magnetization

Thermoremanent magnetization (TRM) is acquired when magnetic minerals cool from high temperatures in a small magnetic field through T_c (precisely, the TRM is acquired at the blocking temperature of the grain, which will be below T_c). Near T_c, thermal fluctuation makes the magnetic barriers so small that a low-intensity field such as the Earth's magnetic field can produce a significant remanent magnetization. Igneous rocks, such as mid-ocean ridge basalt and volcanic rocks, and other baked materials, such as archaeological hearths, usually acquire a TRM. In SD grains, a TRM is usually stable over geological timescales.

2.7.2. Detrital remanent magnetization

Detrital remanent magnetization (DRM) is acquired when sediments are deposited. The magnetic grains within the sedimentary detritus are aligned more or less parallel to the geomagnetic field during deposition of the sediment. DRM, which is acquired by marine, lake and terrestrial sediments, is common and is usually weak. A cryogenic magnetometer is often employed to measure such weak magnetizations.

2.7.3. Chemical remanent magnetization

A chemical remanent magnetization (CRM) is acquired through the formation of magnetic minerals below their respective blocking temperatures in the presence of a magnetic field. The chemical reactions that cause the formation of magnetic minerals can involve alteration of existing magnetic minerals or precipitation of new magnetic minerals. CRM commonly occurs in sedimentary rocks, such as through diagenetic formation of iron sulphides in anoxic environments or as a result of hematite pigmentation and cementation in oxic red beds.

2.7.4. Viscous remanent magnetization

When magnetic minerals are exposed to a weak magnetic field, they will gradually acquire a viscous remanent magnetization (VRM). In zero field, the remanence of a magnetic mineral will gradually decrease because of thermal relaxation. In a small magnetic field, the magnetic moments that have undergone thermal relaxation will become gradually aligned with the magnetic field and produce a VRM. In palaeomagnetism, VRM is a secondary magnetization, which is usually regarded as an undesirable signal. VRM is usually relatively weak, and is normally erased by thermal or alternating field (AF) demagnetization to reveal the primary remanent magnetization of a rock.

2.7.5. Isothermal remanent magnetization

Isothermal remanent magnetization (IRM) is induced by applying a magnetic field for a short period of time at a given temperature. Saturation isothermal remanent magnetization (SIRM) is the IRM acquired in a saturating field. SIRM is usually large and unstable because it is not in the most favoured energy state. IRM is usually induced in the laboratory and is relatively uncommon in nature. An IRM can be induced in nature through lightning strikes (Cox, 1961).

2.7.6. Anhysteretic remanent magnetization

Anhysteretic remanent magnetization (ARM) is a laboratory-induced remanence. ARM is acquired using a combination of two fields: a large AC field and a small DC bias field. As the AC field decreases from a maximum value to zero, the magnetization becomes preferentially oriented in the direction of the DC bias field. TRM is acquired by decreasing the thermal energy. As an analogue for TRM, ARM is acquired by decreasing the external field energy. The ARM is therefore used in many rock magnetic studies as an analogue for TRM.

Chapter 3

Experimental methods

3.1. Introduction

In order to determine the fundamental magnetic properties of greigite, a wide range of experimental methods has been used in this study. These methods include neutron scattering, synchrotron radiation X-rays, and Mössbauer spectroscopy to probe the magnetic structure, electronic structure, and valence state of iron in greigite, and a range of rock-magnetic techniques to investigate the magnetic properties of greigite, and its magnetic domain state dependence. Details of each respective set of techniques are given below.

3.2. Neutron scattering

3.2.1. Basic properties of neutrons

The neutron, discovered by Chadwick (1932), is a subatomic particle with zero charge, mass m = 1.0087, spin s = ½, and magnetic moment μ = -1.9132 nuclear magnetons. The wavelength (λ) of thermal neutrons is comparable to the mean atomic separation in solids, which makes them suitable for probing the structure of condensed matter. Neutrons have a spin, like a micro-magnet, which is sensitive to the magnetic properties of atoms. Neutrons therefore provide a unique tool for studying magnetism on the atomic scale. Neutrons are electrically neutral, which means that interactions between neutrons and matter are confined to the short-range nuclear and magnetic interactions. Neutrons are therefore non-destructive and can penetrate deep into matter. These unique properties make neutrons a powerful probe of condensed matter. There are also disadvantages with using neutron radiation. First, neutron sources are large and costly facilities. There are few facilities for neutron scattering in the world and access to beam-time is limited. Second, neutron sources are relatively weak compared to light or X-rays. Therefore, relatively large quantities of samples are required, typically milligrams for single crystals and grams for powders. Third, it is difficult to focus neutrons compared to light or X-rays. Despite these minor drawbacks, the unique properties of neutrons make neutron scattering techniques widely useful in almost all modern scientific disciplines. The Nobel Prize for Physics in 1994 was awarded to Bertram N. Brockhouse ("for the development of neutron spectroscopy") and Clifford G. Shull ("for the development of the neutron diffraction technique") "for pioneering contributions to the development of neutron scattering techniques for studies of condensed matter". This highlights the significance of neutron scattering in modern experimental physics.

3.2.2. Neutron sources

Neutrons are produced in two main ways: a nuclear reactor or a pulsed spallation source. Nuclear fission in a reactor can produce high flux neutrons, which has been used for power generation and research. Neutrons are released by the fission of uranium-235. Each fission releases 2 - 3 neutrons, one of which is needed to sustain the chain reaction. Currently, the most powerful reactor neutron source in the world is the 57 MW HFR (High-Flux Reactor), which commenced operation in 1972 at the Institut Laue-Langevin (ILL) in Grenoble, France, where neutron scattering experiments were made for this study. At ILL, high flux neutrons (1.5×10^{15} n/cm^2 s) are produced by a nuclear reactor.

A spallation source is a high-flux source in which accelerated protons hit a target material, prompting the emission of neutrons. Particle accelerators and synchrotrons are used to generate intense and high-energy proton beams, which are then directed at a target composed of heavy nuclei. Provided that protons have sufficient kinetic energy, they are able to overcome the intrinsic long-range electrostatic and short-range nuclear forces and effectively blast the target nuclei apart. The most powerful spallation neutron source in the world is the ISIS Facility at the UK Rutherford Appleton Laboratory near Oxford, which commenced operation in late 1984. It is based around a 200 mA, 800 MeV, proton synchrotron that operates at 50 Hz, with a tantalum target that releases approximately 12 neutrons for each incident proton.

3.2.3. Neutron scattering techniques

Neutron scattering involves measuring the deflection of neutron radiation as a probe of the structure and magnetism of target materials. This is possible because neutrons interact with atomic nuclei and the magnetic fields of unpaired electrons. Neutron scattering can be divided into two categories: elastic and inelastic scattering. In neutron elastic scattering, neutrons interact with the matter but do not leave it in an excited state. The emitted neutrons have the same energy as incident neutrons. Neutron inelastic scattering involves energy transfer from the energetic excitation or relaxation of incident neutrons to the matter through interactions. Therefore, the energy of scattered neutrons is either partially lost or enhanced. The neutron scattering experiments undertaken in this study are elastic scattering experiments because it is currently not possible to produce the large single crystals of greigite needed for inelastic neutron scattering experiments. Detailed information about the scattering techniques used in this study is described below.

3.2.3.1. Neutron powder diffraction

Neutron diffraction is a crystallographic method for determining the atomic and magnetic structure of condensed matter (e.g., Bacon, 1975). When passing through a material, neutrons are scattered from nuclei and unpaired electrons through magnetic interactions, from which structural information can be obtained. Neutron diffraction is similar to X-ray diffraction, but with a different radiation. X-rays interact primarily with the electron cloud surrounding the nuclei, while neutrons interact with the nuclei and magnetic moments of unpaired electrons. Neutrons can therefore reveal, in addition to the crystal structure, complementary information about the microscopic magnetic structure of magnetic materials.

Neutrons, like all quantum particles, exhibit wave phenomena. Diffraction occurs when a wave encounters an obstacle with comparable size to the wavelength. When neutrons are slowed down and selected by speed, they can have wavelength near 1 Å, which is the typical separation between atoms in solids. When such a neutron beam encounters a crystalline sample, it will diffract. The neutron beam will scatter at defined angles according to the Bragg Law:

$$n\lambda = 2d\sin\theta, \tag{3.1}$$

where λ is the wavelength of the incident neutrons, d is the atomic distance, θ is the incident angle, and n is an integer. For a typical neutron diffraction experiment (Fig. 3.1), the sample is placed in a neutron beam. The detector records how many neutrons have changed their direction of propagation and measures the intensity of the scattered neutron pattern around the sample.

The instruments used for neutron powder diffraction analysis in this study are the high-intensity neutron powder diffractometer D1B and the high-resolution neutron powder diffractometer D1A (Fig. 3.2) at the ILL. These two diffractometers essentially have the same function, but different resolution. A spectrum can be obtained rapidly on the D1B (a few minutes) and relatively slowly on the D1A (a few hours), while D1A has higher resolution. A vanadium sample container was used because the nuclei of vanadium hardly scatter neutrons.

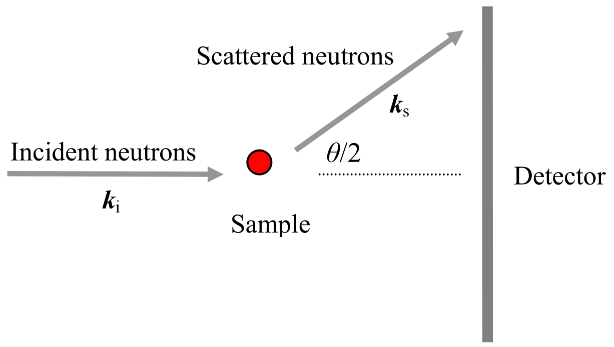

Figure 3.1. Basic set-up for neutron scattering experiments. $\boldsymbol{k}_{\mathrm{i}}$ and $\boldsymbol{k}_{\mathrm{s}}$ are the wave vectors of the incident and scattered neutrons, respectively. The scattering vector $\boldsymbol{Q}$ is defined as the modulus of the resultant between $\boldsymbol{k}_{\mathrm{i}}$ and $\boldsymbol{k}_{\mathrm{s}}$ and is given by $Q = |k_i - k_s| = (4\pi n/\lambda) \sin(\theta/2)$.

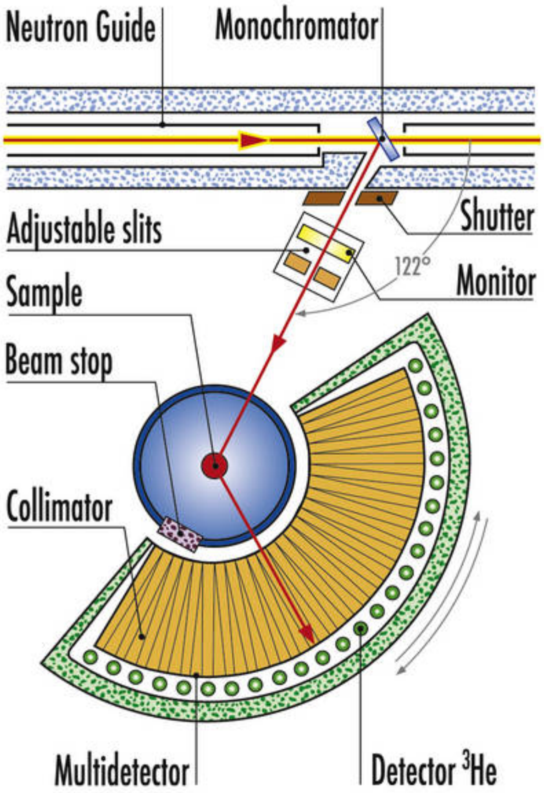

Figure 3.2. Instrument layout of the high-resolution neutron powder diffractometer D1A at the ILL, Grenoble, France (source: http://www.ill.eu/d1a/home/).

3.2.3.2. Polarized neutron diffraction

Hot neutrons from a nuclear reactor have random spin orientations. Polarized neutrons have had their spins oriented in a single direction using neutron polarization techniques. In addition to the functions provided by normal neutrons, polarized neutrons allow unambiguous separation of the nuclear, magnetic and nuclear-spin-incoherent scattering over a large range of $\boldsymbol{Q}$ values. Polarized neutron beams can be used for neutron diffraction experiments in addition to unpolarized beams. At the ILL, supermirrors are used to polarize the spin of neutrons. The supermirror consists of superposed thin layers of materials with contrasting reflecting powers, such as nickel or titanium, deposited on a substrate.

Greigite decomposes below its Curie point (e.g., Roberts, 1995), therefore it is not possible to measure neutron diffraction patterns above and below T_C to separate the magnetic component of the Bragg peaks. In this study, polarized neutron diffraction was used to isothermally separate the nuclear and magnetic scattering. Polarized neutron diffraction, which in principle should enable more accurate detection of the magnetic structure, is used to clarify the magnetic structure determination from neutron powder diffraction. Polarized neutron diffraction analyses were made on the neutron diffuse scattering spectrometer D7 (Fig. 3.3) at the ILL.

3.3. Mössbauer spectroscopy

Mössbauer spectroscopy is a spectroscopic technique based on the Mössbauer effect – recoil-free gamma-ray emission and absorption, from which information about chemical, structural, magnetic and time-dependent properties of materials can be obtained. The Mössbauer effect was discovered by the German physicist Rudolph Mössbauer in 1957, for which he received the Nobel Prize in Physics in 1961. Since its discovery, Mössbauer spectroscopy has proved to be a versatile and precise technique with widespread use in many scientific disciplines, including physics, chemistry, geology and biology (e.g., Greenwood and Gibb, 1971).

3.3.1. The Mössbauer effect

Before discovery of the Mössbauer effect, it was difficult to observe the resonance of gamma-rays (created by nuclear transitions) largely because of two major effects: the extremely small hyperfine interactions between the nucleus and its environment, and the recoil of nuclei when emitting or absorbing gamma rays (Fig. 3.4a). Mössbauer discovered that when the atoms are within a solid matrix, the effective mass of the nucleus is therefore much larger, which makes the recoiling energy small (Fig. 3.4b). The gamma-ray energy is so small that the recoil of the nucleus is too low to be transmitted as a phonon due to the quantum property of the lattice vibration, which produces a recoil-free gamma-ray emission and absorption. This recoil-free emission and absorption of gamma rays is referred to as the Mössbauer effect, which allows observation of gamma-ray resonance and produces Mössbauer spectra.

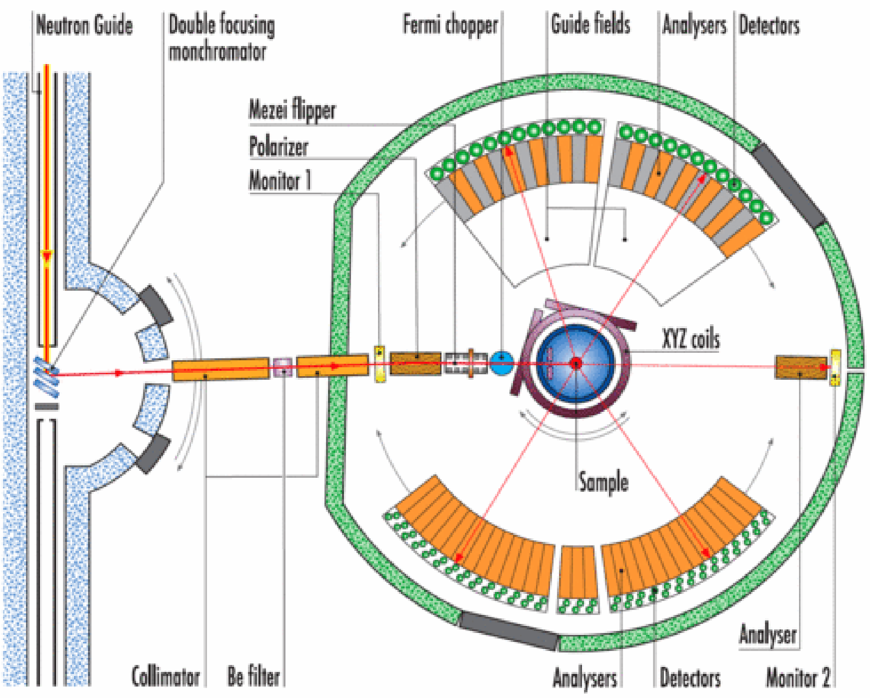

Figure 3.3. Instrument layout of the neutron diffused diffractometer D7 at the ILL, Grenoble, France (source: http://www.ill.eu/d7/home/). A supermirror is used to polarize the incident beam of cold neutrons. In this study, a thin sheet (0.1 mm) of unmagnetized iron was used to depolarize the scattered beam to avoid analyzing polarization of the scattered beam.

3.3.2. Hyperfine interactions

Hyperfine interactions are the interactions between a nuclear and its surrounding environment, which can change the energy level of nuclear transitions and therefore affect the shape of Mössbauer spectra. Hyperfine interactions are extremely small compared to the energy level of a nucleus. Before discovery of the Mössbauer effect, it was difficult to observe these small interactions because of the large background energies. The extremely high energy resolution of the Mössbauer effect enables observation of these interactions. Isomer shift, quadrupole splitting and magnetic splitting are three types of hyperfine interactions. The nuclear Hamiltonian can be written as (Greenwood and Gibb, 1971):

$$H = H_0 + E_0 + M_1 + M_2, \tag{3.2}$$

where E_0, M_1 and M_2 are the electric monopole interaction, the magnetic dipole interaction and the electric quadrupole interaction, respectively. H_0 represents all other terms except for the hyperfine interactions.

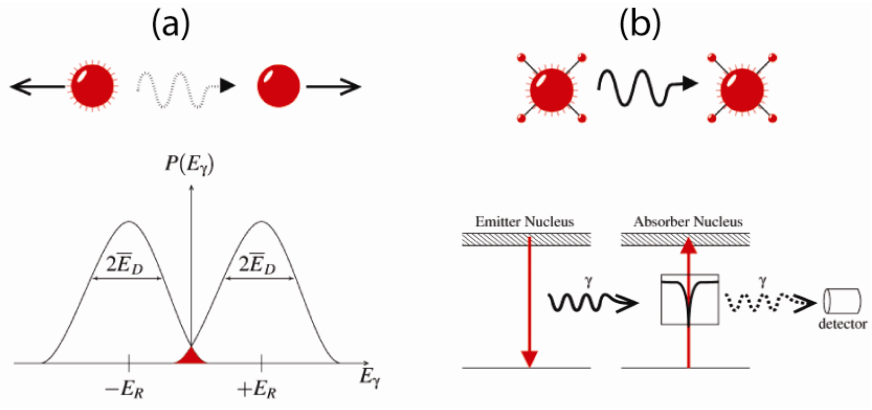

Figure 3.4. (a) Recoil of free nuclei due to conservation of momentum when emitting or absorbing a gamma ray. Because of the recoil, the resonant overlap is too small, which prevents resonance. (b) The Mössbauer effect. In a solid matrix, the emitted and absorbed gamma rays have the same energy, which produces the gamma-ray resonance. From the Royal Society of Chemistry (source: http://www.rsc.org/Membership/Networking/InterestGroups/MossbauerSpect/intro.asp).

The chemical isomer shift δ is produced by the difference in electron densities around the nucleus. It originates from the Coulomb interaction of the nuclear-charge distribution over a finite nuclear radius in the excited and ground states and the electron-charge density at the nucleus (Gonser, 1975). The s electron density of the resonating nuclei in the source and in the absorber will be different. The Coulomb interaction changes the levels of the ground and excited states. This difference in density changes the Mössbauer transition energy and therefore produces a shifted Mössbauer spectrum (Fig. 3.5a). Mössbauer spectroscopy is a relative method because δ cannot be measured directly. A suitable reference for a specific source or an absorber is therefore needed. The isomer shift can probe the valence state of a compound. For example, Fe^{2+} has a lower *s* electron density around the nucleus due to the greater screening of the *d* electrons, therefore δ in Fe^{2+} is larger than in Fe^{3+}.

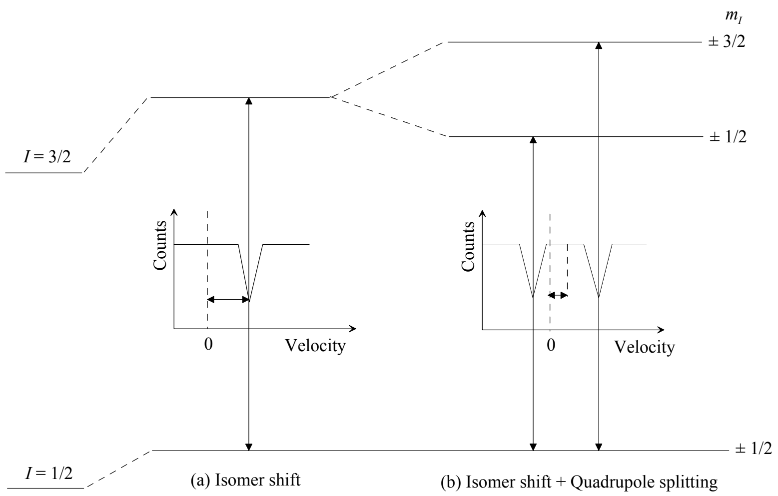

(a) Isomer shift

(b) Isomer shift + Quadrupole splitting

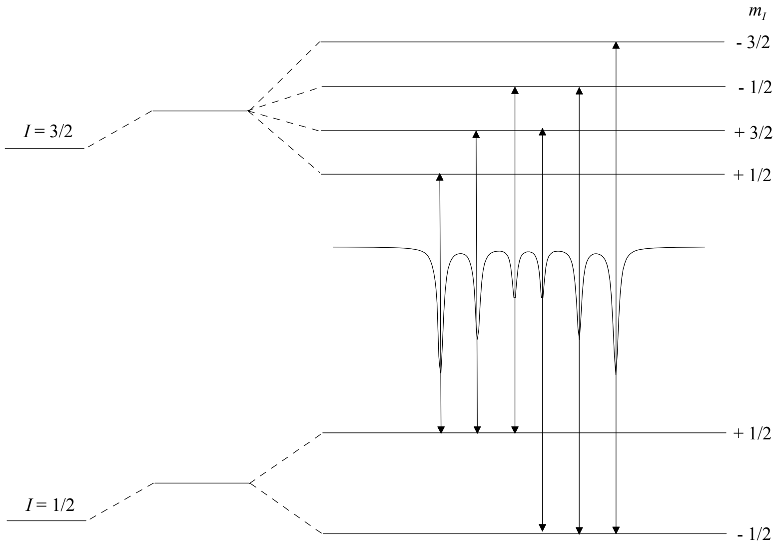

(c) Magnetic splitting

Figure 3.5. Illustration of hyperfine interactions: (a) isomer shift, (b) isomer shift + quadrupole splitting and (c) magnetic splitting. This demonstrates how the three main hyperfine interactions change energy levels and how these effects influence the Mössbauer spectra. After Greenwood and Gibb (1971).

Nuclei in states with an angular momentum quantum number $I > 1/2$ have a non-spherical charge distribution. This produces a nuclear quadrupole moment. An asymmetric charge distribution around the nucleus or a ligand arrangement will cause an asymmetrical electric field at the nucleus. The electric quadrupole interaction will give rise to splitting in the nuclear energy levels and produces a two-line shape of a Mössbauer spectrum (Fig. 3.5b).

The magnetic field at the nucleus produces the magnetic hyperfine interaction, which originates from the dipole interaction between the nuclear spin moment and a magnetic field. The magnetic field can originate either within the atom, within the crystal via exchange interactions, or as a result of applying an external magnetic field. The Hamiltonian for the magnetic hyperfine dipole interaction is (Greenwood and Gibb, 1971):

$$\mathbf{H} = -\boldsymbol{\mu}\cdot\boldsymbol{H} = -g\mu_N\boldsymbol{I}\cdot\boldsymbol{H}, \tag{3.3}$$

where $\boldsymbol{H}$ represents the total magnetic field, $\boldsymbol{\mu}$ is the nuclear magnetic moment, μ_N is the nuclear Bohr magneton, $\boldsymbol{I}$ is the nuclear spin and g is the nuclear g-factor. The eigenvalues of this Hamiltonian are:

$$E_M = -g\mu_N H m_I, \tag{3.4}$$

where m_I is the magnetic quantum number representing the z component of $\boldsymbol{I}$. The magnetic field splits the nuclear level of spin $\boldsymbol{I}$ into $(2\boldsymbol{I} + 1)$ equispaced non-degenerate substates, which, coupled with the selection rule ($\Delta m_I = 0, \pm 1$), produces six-line Mössbauer spectra for a 3/2 → 1/2 transition (Fig. 3.5c).

3.3.3. Mössbauer spectroscopy applied to magnetism

Mössbauer spectroscopy is a versatile technique that is not only used in physics, but that also has applications in almost all natural sciences. In this study, Mössbauer spectroscopy is used for chemical, structural, and magnetic property investigations. The application of Mössbauer spectroscopy in magnetism is briefly discussed below. More information can be found in text books by Greenwood and Gibb (1971) and Gonser (1975).

3.3.3.1. Magnetic characterization studies

Mössbauer spectroscopy is frequently used for magnetic characterizations, such as determination of the magnetic ordering temperature, phase identification, identification of phase transitions, and determination of ion distributions (e.g., Gonser, 1975). Determination of the magnetic ordering temperature is achieved by measuring the temperature variation of the internal magnetic field. Assuming that H_{int} is proportional to the magnetization, one can determine the ordering temperature by extrapolating to $H_{\mathrm{int}} = 0$. Phase identification is based on characteristic hyperfine parameters observed in a Mössbauer spectrum, similar to X-ray diffraction. Phase transitions can be detected by determining the temperature dependence of hyperfine parameters. Mössbauer spectroscopy also provides a useful tool for determining relative site populations of cations.

3.3.3.2. Magnetic structure studies

Mössbauer spectroscopy can be used to determine types of magnetic ordering, i.e., ferromagnetic, ferrimagnetic, or antiferromagnetic, by applying an external magnetic field to a polycrystalline material to observe variations in hyperfine transition intensities. The spin distribution of magnetic materials with low magnetic anisotropy will align parallel/antiparallel to the external field. If the wave vector $\boldsymbol{k}$ is parallel to the applied field, the hyperfine transitions will disappear due to their $\sin^2\theta$ angular dependence. For ferrimagnets, the magnetic fields within sublattices align either parallel or antiparallel to the external field. The hyperfine interactions will therefore increase or decrease with increasing external field. These characteristics can be used to determine ferrimagnetic ordering. For polycrystalline antiferromagnets, application of an external magnetic field will have little effect on the relative line intensities because of weak spin polarization, but the absorption lines will broaden because of the random orientation of external and internal magnetic fields. More information about magnetic structure can be obtained using the angular dependence of absorption line intensities when using polarized γ-ray sources on single crystals of ordered magnetic materials (Gonser, 1975).

3.3.3.3. Characterization of superparamagnetic behaviour

Not all compounds that contain unpaired valence electrons will display a magnetic hyperfine splitting. The observation time-scale of the vectors $\boldsymbol{I}$ and $\boldsymbol{H}$ in the Hamiltonian Equation 3.3 is of the order of 10^{-8} s. Electronic spin relaxation involves the change of directions of electronic spins that generate $\boldsymbol{H}$. When the electronic spins relax on a time-scale comparable with the nuclear transition, it will produce more complicated spectra. In paramagnetic materials, the spin relaxation is rapid, which produces ***H*** with a time-average of zero and therefore no magnetic splitting is observed. The two main processes that cause spin-flipping of paramagnetic ions are electronic spin-spin interactions of neighbouring ions and electronic spin-lattice interactions. Spin-spin processes involve energy transfer between interacting spins via dipole and exchange spin relaxation. Spin-lattice relaxation involves transfer of Zeeman energy of the spin system to phonon modes of the lattice via spin-orbit coupling. For magnetically ordered materials, the observed magnetic hyperfine spectra are interpreted using spin waves. If the fluctuation rate of the spin waves is slow compared to the precession frequency of the nucleus in the field ***H***, the full six-line pattern will be observed. If the spin relaxation frequency is of the order of the Larmor frequency, the spin-wave time-average is time dependent and an inward collapse of the hyperfine spectrum will occur. If the fluctuation rate is extremely rapid, the nucleus will experience only a time-averaged zero field and a symmetric quadrupole pattern will be observed. In summary, SP assemblages and paramagnetic materials will display two-line quadrupole Mössbauer patterns because of rapid spin relaxation, while materials with stable magnetizations will display the six-line magnetic hyperfine splitting.

3.4. X-ray absorption spectroscopy and X-ray magnetic circular dichroism

In X-ray absorption, a core electron transits to an empty state above the Fermi level by absorbing a photon. For 3*d* transition metal elements, such as Fe, Co and Ni, their magnetic properties are largely determined by the 3*d* valence electrons. The excitation of core electrons into empty states above the Fermi energy in the absorption process therefore determines the electronic and magnetic properties of the empty valence levels. X-ray absorption spectroscopy (XAS) is a spectroscopic technique based on the energy dependent absorption of X-rays, from which information about the elemental composition, chemical environment of the atoms, and the magnetic state of materials can be obtained.

X-ray magnetic circular dichroism (XMCD) represents the difference spectrum of two X-ray absorption spectra, one taken with left-circularly polarized light, and one with right-circularly polarized light (Hippert et al., 2006). The *d* shell has a spin moment associated with the imbalance of spin-up and spin-down electrons or holes. By employing the right- or left- circularly polarized photons whose angular momenta are transferred to the excited photoelectron, the X-ray absorption process is then spin dependent and the difference in the number of *d* electrons or holes with up- and down-spins can be measured. The photoelectron carries the transferred angular momentum as a spin or as an angular momentum, or both. Right- and left-circular photons will transfer opposite momenta to the electron, which therefore produces photoelectrons with opposite spins. Spin flips are forbidden in electric dipole transitions, therefore spin-up (spin-down) photoelectrons from the *p* core shell can only be excited into spin-up (spin-down) *d* hole states. Hence, the spin-split valence shell acts as a detector for the spin of the excited photoelectron and the transition intensity is proportional to the number of empty *d* states. XMCD is a sensitive probe of electronic and magnetic properties of condensed matter, such as spin and orbital magnetic moments.

For Fe, the absorption spectra for XAS and XMCD are usually measured at the *L*-edge where 2*p* electrons are excited to 3*d* states by an X-ray of ~700 eV. The *L*-edge X-ray absorption spectra of the transition metals and oxides are dominated by two main peaks separated by about 15 eV. The two main structures are called the L_3 (lower energy) and L_2 (higher energy) absorption edges. Since the L_3 and L_2 levels have opposite spin-orbit coupling, the spin polarization will be opposite at the two edges. XMCD measurements are usually undertaken at synchrotron radiation facilities where intense X-ray beams are produced. XMCD spectra for greigite in this study were obtained using the Synchrotron Radiation Source at the Daresbury Laboratory, UK.

3.5. Rock magnetic techniques

3.5.1. Hysteresis

Ferromagnetic/ferrimagnetic/canted antiferromagnetic substances have non-reversible magnetization and remanent magnetization, which give rise to magnetic hysteresis properties. A hysteresis loop is measured by recording the sample magnetization between a negative and a positive magnetic field (Fig. 3.6a). Hysteresis parameters (B_c, B_{cr}, M_{rs}, and M_s, where B_c is the coercivity, B_{cr} is the coercivity of remanence, M_{rs} is the saturation remanent magnetization and M_s is the saturation magnetization) are indicators of the magnetic properties of the measured magnetic particle assemblage. At magnetic saturation, the domain magnetizations are perfectly aligned with $\boldsymbol{B}$. After removing the field, the magnetization will relax to the nearest easy magnetic axis. M_{rs} is the magnetization that remains when the applied field is reduced to zero after applying a saturating field. M_{rs} depends on the number and orientation of the magnetic easy axes and on the type of magnetic anisotropy. If the magnetic easy axis is parallel to the applied field, M_{rs} will equal M_s. If it is perpendicular, M_{rs} will reduce to zero. In cubic crystals with positive K_1, the easy direction is aligned along the $\langle 100 \rangle$ crystallographic axis and the domain magnetization will lie along one of the three $\langle 100 \rangle$ directions. Averaging M_s gives a M_{rs} of $0.832M_\mathrm{s}$. For systems with uniaxial anisotropy and positive K_1, the remanent magnetization for a hemicircle in a two-dimensional system and a hemisphere in a three-dimensional system gives a M_{rs} of $0.637M_\mathrm{s}$ and $0.5M_\mathrm{s}$, respectively. B_c is the field at which the remanent magnetization is reduced to zero. It is the point of magnetization reversal, where the barrier between two magnetization states is reduced to zero by the applied field. It is an indicator of energy gradients which oppose magnetization changes. Generally, SD magnetic materials or materials with few domains have higher coercivities compared to those with more domains (Fig. 2.5). For SD particles, the hysteresis mechanism is controlled by the rotation of spontaneous magnetization. When the applied magnetic field overcomes the magnetic anisotropy energy, the spontaneous magnetization will rotate to align with the applied field. For MD grains, the hysteresis properties are controlled by domain wall movements, as well as by the rotation of spontaneous magnetization (Fig. 3.7). The magnetization process is dominated by domain wall motion, while the remanence is dominated by domain wall pinning from crystal defects, i.e., vacancies, dislocations and grain boundaries, which can increase the coercivity (Fig. 2.5).

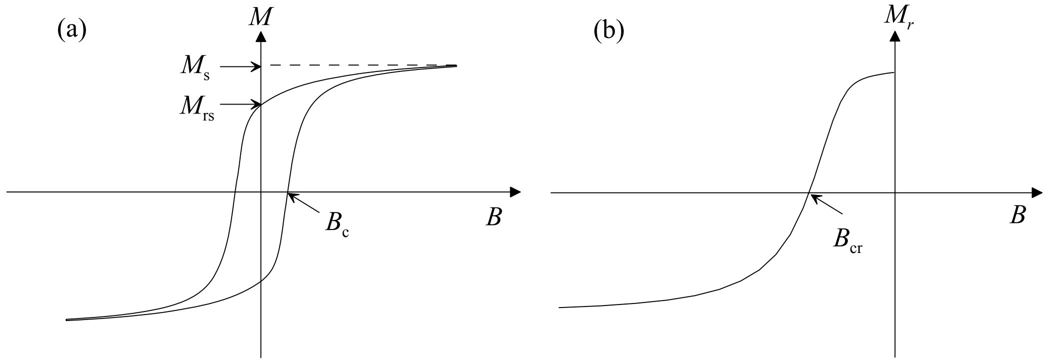

Figure 3.6. Response of magnetization for magnetically ordered materials to applied fields: (a) hysteresis loop; (b) back-field demagnetization curve for an isothermal remanent magnetization. Typical hysteresis parameters are indicated.

Hysteresis properties depend on many factors, such as stoichiometry, grain size, domain state, oxidation state, magnetic anisotropy, stress, and temperature. It is these dependences that make hysteresis measurements useful in rock magnetic investigations. The scheme of the Day plot provided by Day et al. (1977), where the ratio B_{cr}/B_c is plotted against the ratio M_{rs}/M_s, has been widely used in palaeomagnetic studies as an indicator of domain state for (titano-)magnetite (Fig. 3.8). Dunlop (2002) showed that mixtures of magnetite domain states follow different trends on a Day plot. Natural samples often contain mixtures of domain states or mixtures of magnetic minerals. This produces, in addition to different hysteresis parameters, hysteresis loops with various shapes, including wasp-waisted or potbellied loops (e.g., Roberts et al., 1995; Tauxe et al., 1996; Fabian, 2003), from which more information about the magnetic properties of samples can be obtained.

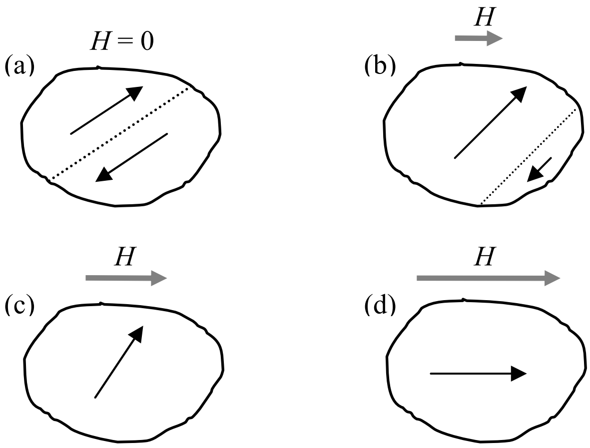

Figure 3.7. The magnetization process in a two-domain grain: (a) the demagnetized state, (b) domain wall movement under small applied fields, (c) disappearance of the domain wall as a result of increased applied field, making the MD grain into a SD grain, and (d) the saturated state. Arrows within the grains represent the spontaneous magnetization of the respective domains. The dashed line represents the domain wall, which moves under forcing of the applied field and is eventually annihilated by the field.

3.5.2. First-order reversal curve diagrams

First-order reversal curves (FORCs) are partial hysteresis loops that are measured by cycling between a positive saturation field and a reversal field (Mayergoyz, 1986). A sample is first saturated in a large positive applied field. The field is then decreased to a reversal field B_a. The magnetization M (B_a, B_b) is measured for a series of field values B_b between B_a and the saturation field (Fig. 3.9). The same measurement procedure is repeated for different B_a values to acquire a set of FORC measurements (Fig. 3.10a). A FORC distribution is calculated as the mixed second derivative (Pike et al., 1999; Roberts et al., 2000):

$$\rho(B_a, B_b) = -\frac{\delta^2 M(B_a, B_b)}{\delta B_a \delta B_b}. \tag{3.5}$$

A FORC diagram is a contour plot of the FORC distribution in the transformed coordinate system $\{B_i, B_c\}$ (where $B_i = (B_a + B_b)/2$, $B_c = (B_a - B_b)/2$). FORC diagrams provide useful magnetic information about measured samples: the distribution along the B_c axis indicates the coercivity distribution, while the vertical spread along the B_i axis indicates the magnetostatic interaction field distribution (Pike et al., 1999; Roberts et al., 2000) (Fig. 3.10b).

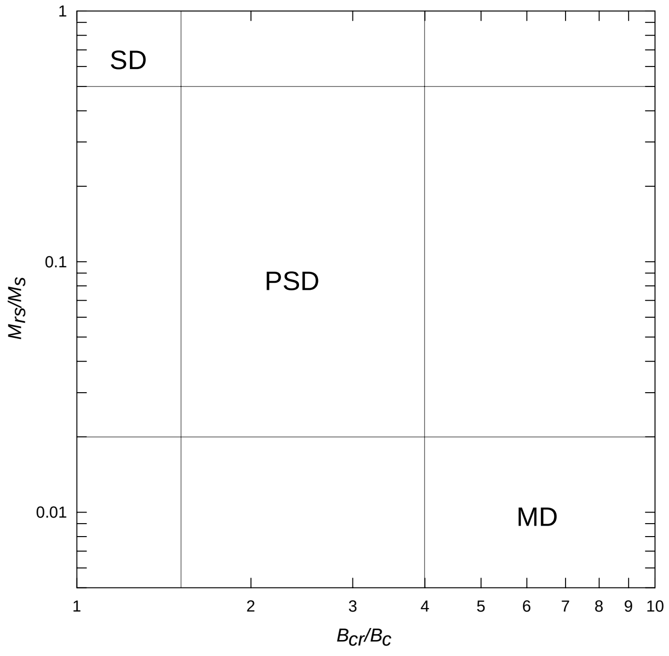

Figure 3.8. The Day plot, with experimentally determined regions for SD, PSD and MD magnetite (Day et al., 1977). Hysteresis data lie in different domain-state regions: small SD grains have high M_{rs}/M_s values and low B_{cr}/B_c values, whereas large MD grains have low M_{rs}/M_s values and high B_{cr}/B_c values.

The conventional method to calculate FORC distribution employs a least squares fit to M (B_a, B_b) over a square grid of data points (Pike et al., 1999; Roberts et al., 2000). The magnetization is fitted using a second-order polynomial function:

$$M(B_a, B_b) = a_1 + a_2 B_a + a_3 B_a^2 + a_4 B_b + a_5 B_b^2 + a_6 B_a B_b. \tag{3.6}$$

The value of the FORC distribution is $-a_6$. The smoothing factor (Roberts et al., 2000) determines the size of the square grid. While smoothing reduces experimental noise, it can also affect the FORC distribution (Roberts et al., 2000). Other methods for calculating FORC diagrams include the reversible-ridge method (Pike, 2003) and the locally weighted polynomial regression method (Harrison and Feinberg, 2008). FORC diagrams in this thesis were produced using either FORClab (Winklhofer and Zimanyi, 2006) or FORCinel (Harrison and Feinberg, 2008).

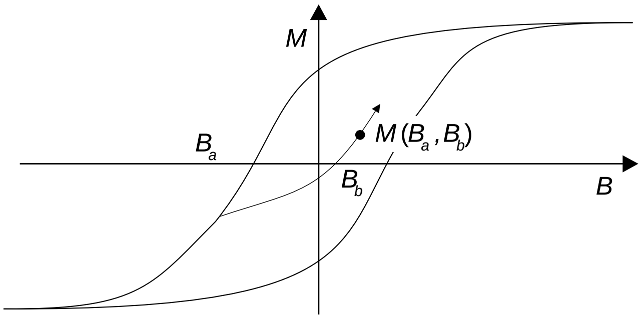

Figure 3.9. Example of a FORC measurement. The magnetization is measured at a series of field values (B_b) between a reversal field B_a and positive saturation.

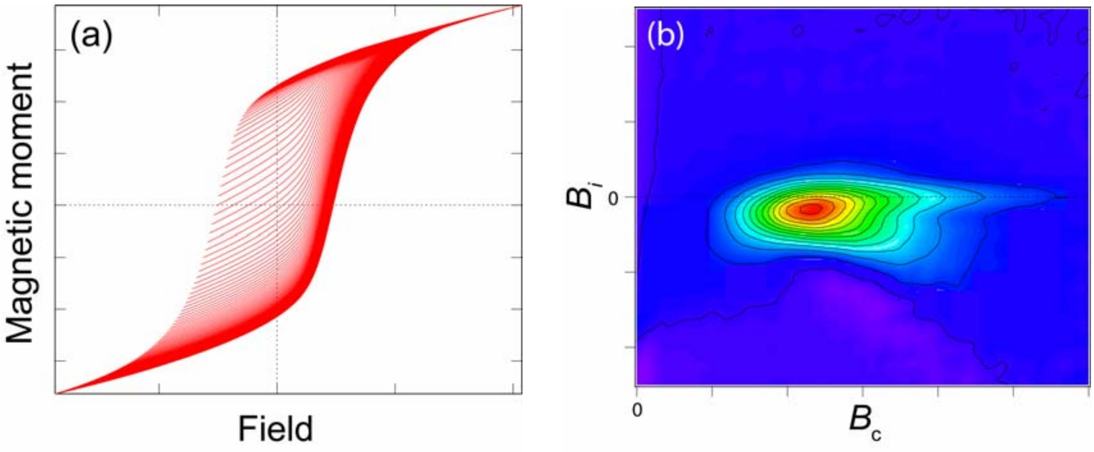

Figure 3.10. (a) An example of a set of FORC measurements. (b) The corresponding FORC diagram, which indicates the coercivity distribution along the B_i axis and the strength of magnetic interactions within the measured sample along the B_c axis.

Chapter 4

Magnetic characteristics of synthetic pseudo-single-domain and multi-domain greigite

---

This chapter was published in *Geophysical Research Letters*, Volume 34, Chang, L., A. P. Roberts, A. R. Muxworthy, Y. Tang, Q. Chen, C. J. Rowan, Q. Liu and P. Pruner, Magnetic characteristics of synthetic pseudo-single-domain and multi-domain greigite (Fe_3S_4), L24304, doi:10.1029/2007GL032114. Copyright (2007), with permission of the American Geophysical Union.

Abstract We report the magnetic properties of pure synthetic pseudo-single-domain (PSD) and multi-domain (MD) greigite and the grain size dependence of the magnetic properties of greigite for the first time. The dominantly PSD-like and MD-like behaviour are demonstrated by hysteresis, first-order reversal curve diagrams, low-temperature cycling (LTC) of room temperature saturation isothermal remanent magnetization (SIRM) and low-temperature SIRM warming curves. Variations in a range of magnetic properties clearly correlate with grain size. Characteristic PSD/MD behaviour is preserved at low temperatures, which, coupled with the small decrease in remanence during warming, rule out the presence of substantial superparamagnetic behaviour in the studied samples. LTC-SIRM measurements indicate a continuous demagnetization of remanence during cooling. Knowledge of this expanded range of magnetic properties of greigite should be widely useful in environmental magnetic and palaeomagnetic studies.

4.1. Introduction

Greigite is a ferrimagnetic iron sulphide mineral that forms in sulphate-reducing conditions as a precursor to pyrite in association with bacterial degradation of organic matter (Berner, 1984). It is now recognized as a widespread magnetic mineral in many marine and lake sedimentary environments (e.g., Roberts and Weaver, 2005, and references therein). The widespread occurrence of greigite makes understanding its magnetic properties important in many palaeomagnetic and environmental magnetic studies (e.g., Snowball, 1991; Rowan and Roberts, 2006). However, unlike its iron oxide spinel counterpart, magnetite, whose magnetic properties are well established, the magnetic properties of greigite are relatively poorly known. For example, no systematic study of the PSD and MD magnetic properties and no grain size dependence of magnetic properties have been reported for greigite.

Greigite commonly occurs in the SD state in sediments (Roberts, 1995). Rock magnetic results from Neogene marine sediments from eastern New Zealand demonstrate the widespread occurrence of SP behaviour in many greigite-bearing sediments (Rowan and Roberts, 2006). This natural greigite has fine grain size of normally less than a few hundred nanometres. MD behaviour has been occasionally reported for natural greigite. For example, Hoffmann (1992) reported greigite from a brown coal basin in the Czech Republic (Krs et al., 1990) that has a grain size of 4-8 μm and MD-like magnetic properties. First-order reversal curve (FORC) measurements for a natural greigite sample from the same sequence (Fig. 4.1c) provide evidence of a mixture of SD and MD grains (Roberts et al., 2006). Coarse-grained greigite with MD properties can therefore be preserved over geological timescales in some settings. Synthetic greigite has been reported to consist of fine grains, normally in the nanometer size range (e.g., Uda, 1965; Dekkers and Schoonen, 1996; Chen et al., 2005), and are dominated by SP behaviour (e.g., Spender et al., 1972; Roberts, 1995). However, no synthetic PSD/MD greigite has been reported in the literature due to difficulties in synthesizing large greigite particles. We report the first magnetic data for synthetic PSD/MD greigite and provide a domain state dependent magnetic property framework for synthetic and natural greigite.

4.2. Samples

Greigite samples were synthesized using a new hydrothermal method (Tang et al., 2007) by reacting iron chloride ($FeCl_3{\cdot}6H_2O$) with thiourea (CH_4N_2S) and formic acid (HCOOH) at 170°C for 8 hours. The black powders consist of pure crystalline greigite (see Chapter 5 and Appendix A). Twenty-one batches of pure greigite were produced (S171 – S711, Table 4.1), and subjected to magnetic measurements shortly after synthesis. Iron sulphide nodules, containing SD greigite, from the Valle Ricca section near Rome (Florindo and Sagnotti, 1995), and greigite-bearing Neogene marine sediments from eastern New Zealand, which contain variable mixtures of SP and stable SD properties (Rowan and Roberts, 2006), and a sample with mixed natural SD and MD greigite (Roberts et al., 2006) from the Czech Republic (locality numbers 4077-81 (D16) in Fig. 1 of Krs et al. (1990)) were also analysed to compare results with those from the synthetic PSD/MD samples, and to enable comparison of magnetic properties across a range of grain sizes for greigite.

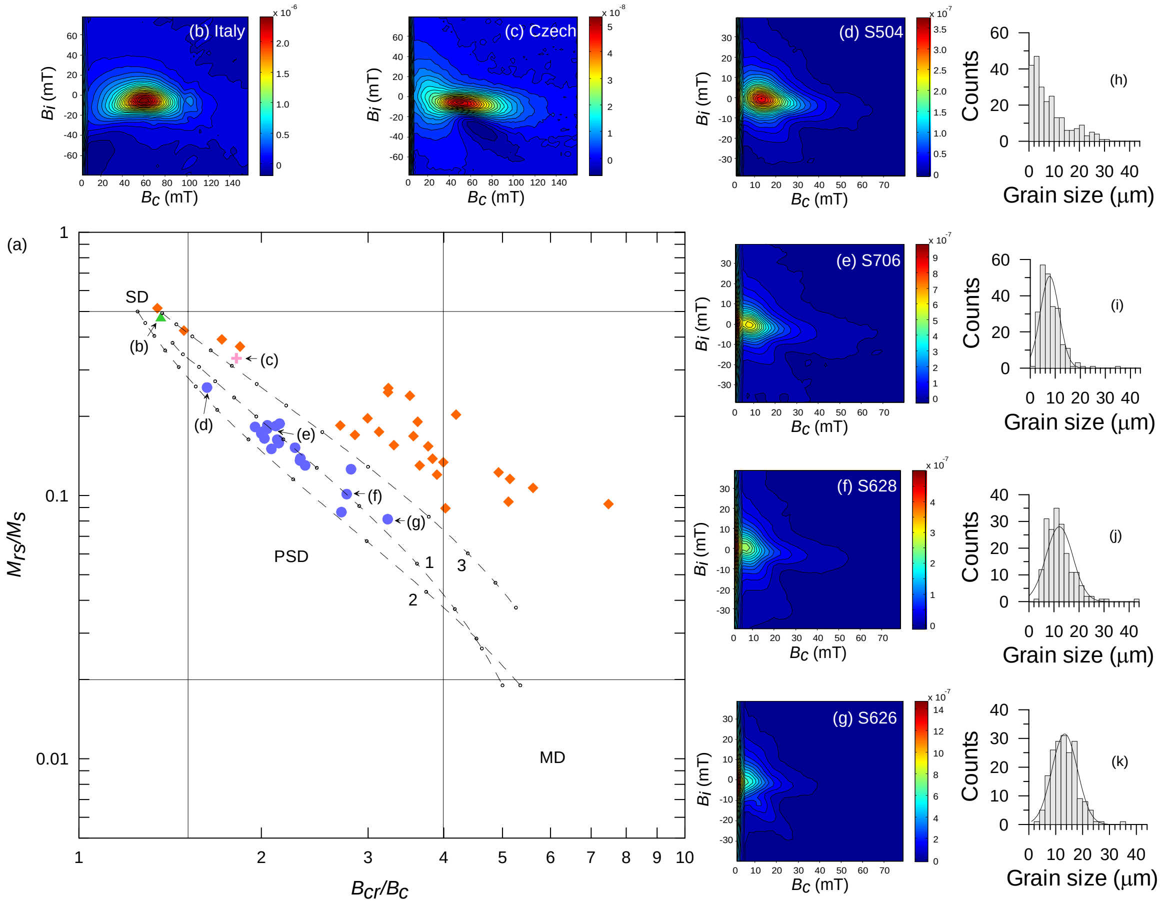

Figure 4.1. (a) Hysteresis data plotted after Day et al. (1977), (b-g) FORC diagrams for samples in (a), and (h-k) grain size distributions for the synthetic greigite samples. Hysteresis ratios (solid circles) follow theoretical SD-MD mixing curves (1, 2 and 3; Dunlop (2002)). Decreasing M_{rs}/M_s and increasing B_{cr}/B_c are matched by increasing average grain size, consistent with progressive evolution of the FORC diagrams. Data for natural greigite samples are plotted for comparison. ‘Italy’ (triangle) is a typical natural SD sample (see (b)) from a greigite-bearing nodule from the Valle Ricca section, near Rome, Italy (Florindo and Sagnotti, 1995). ‘Czech’ (cross) is a natural greigite sample containing a mixture of SD, PSD and MD grains (see (c)) from the Czech Republic (cf. Krs et al., 1990). ‘New Zealand’ (solid diamonds) are Neogene marine sediments from eastern New Zealand that contain significant concentrations of SP grains, which follow SP-SD mixing curves (Roberts and Rowan, 2006).

Table 4.1. Room-temperature hysteresis parameters of the studied greigite samples.

Samples	B_c (mT)	B_{cr} (mT)	M_{rs}/M_s	B_{cr}/B_c	Mean grain size (μm)
S171	4.1	11.4	0.101	2.766	
S426	7.9	16.7	0.184	2.113	
S504	11.9	19.3	0.257	1.627	< 4
S510	8.1	16.6	0.179	2.046	8.8 ± 4.6
S519	7.4	15.7	0.163	2.125	
S622	6.9	15.7	0.152	2.273	
S624	7.0	14.0	0.172	1.999	
S625	6.5	13.1	0.165	2.024	
S626	4.1	13.5	0.081	3.232	13.2 ± 4.5
S627	6.3	14.6	0.136	2.317	
S628	5.1	14.4	0.126	2.812	12.0 ± 4.8
S629	6.9	14.0	0.175	2.016	
S630	5.4	12.6	0.138	2.320	11.4 ± 5.3
S702	7.0	15.1	0.188	2.144	7.6 ± 3.7
S703	7.0	15.0	0.161	2.137	
S705	7.1	14.5	0.185	2.046	
S706	7.3	14.2	0.182	1.953	7.8 ± 3.8
S707	5.7	11.9	0.150	2.078	
S709	6.7	14.3	0.158	2.137	
S710	5.9	13.9	0.130	2.363	
S711	4.8	13.0	0.087	2.711	
Italy	49.9	68.1	0.478	1.365	
Czech	30.9	56.3	0.332	1.820	

4.3. Methods

Hysteresis loops and back-field magnetizations were measured to determine the B_c, B_{cr}, M_{rs} and M_s using a Princeton Measurements Corporation vibrating sample magnetometer (VSM). FORCs were also measured on the VSM (140 FORCs per sample; averaging time = 200 ms) and FORC distributions were calculated based on the algorithm of Pike (2003) using a smoothing factor of 3 (Roberts et al., 2000). Low-temperature cycling (LTC) of a room-temperature saturation isothermal remanent magnetization (SIRM) (LTC-SIRM) and low-temperature SIRM warming after zero-field cooled (ZFC) and field cooled (FC) treatments were made with a Quantum Designs magnetic properties measurement system (MPMS). For LTC-SIRM, the samples were imparted with a room-temperature SIRM; the remanence was then measured from room temperature to 10 K and back to room temperature in zero-field. For SIRM warming curves, samples were cooled to 10 K either in a 5 T field or in zero-field. A 5 T field was applied to the samples at 10 K and was switched off to impart a low-temperature SIRM. The remanence was then measured during warming in zero-field. SEM observations were used to characterize the morphology and grain size (using a LEO 1450VP SEM, operated at 10-20 keV with an acceleration voltage of 17-20 pA). Grain size distributions were determined by measuring the long-dimension of ~200 grains for each sample (most grains are equi-dimensional).

4.4. Results

Room-temperature hysteresis parameters (Table 4.1) indicate that the synthetic samples are magnetically soft compared with natural SD greigite samples (cf. Roberts, 1995). Typical FORC diagrams for the studied synthetic samples (Fig. 4.1g, 4.2c-e) have divergent contours, which are characteristic of MD behaviour (e.g., Roberts et al., 2000; Pike et al., 2001b). In addition to MD-like behaviour, samples at the finer end of the grain size spectrum (Fig. 4.1h) have FORC distributions with concentric inner contours resembling those expected for PSD grains (Roberts et al., 2000) (Fig. 4.1d, 4.2a, b). As is the case for magnetite (Roberts et al., 2000; Muxworthy and Dunlop, 2002), the FORC distribution peak shifts to lower coercivities (Fig. 4.1d-g) as the mean grain size increases (Fig. 4.1h-k). A FORC diagram for a greigite-bearing Miocene lacustrine sediment from the Czech Republic (Krs et al., 1990) contains a peak in the FORC distribution at B_c ~60 mT (Fig. 4.1c), with concentric and vertically spread inner contours and outermost contours that diverge rather than converge at lower coercivities, as would be expected for a MD distribution (Fig. 4.1c). Roberts et al. (2006) interpreted this FORC diagram as containing evidence for bi-modal mixtures of SD and MD grains. The studied synthetic greigite samples extend these observations to coarser grain sizes, where the FORC diagrams consist of clearly divergent contours (Fig. 4.1d-g), which suggest the dominance of PSD/MD particles. Low-temperature FORC distributions for selected PSD and MD synthetic samples are almost indistinguishable from room-temperature FORC diagrams (Fig. 4.2), unlike PSD magnetite, for which the FORC distribution splits into two sets of concentric contours at low temperatures (e.g., Carvallo and Muxworthy, 2006; Smirnov, 2006), which is probably associated with induced anisotropy effects (Smirnov, 2006). It should be noted, however, that it is still unclear whether the observed splitting of the FORC distribution occurs across the entire PSD size range in magnetite. Nevertheless, the lack of a low-temperature magnetic transition for greigite (e.g., Spender et al., 1972; Roberts, 1995) could explain the low-temperature stability of the FORC diagrams for PSD/MD greigite (Fig. 4.2). Low-temperature FORC diagrams also provide further evidence that the low coercivities of these samples result from the presence of dominantly PSD/MD behaviour rather than thermally activated SD behaviour. Zero-field LTC (300 K → 10 K → 300 K) of a room-temperature SIRM (Fig. 4.3a) reveals no discontinuities, unlike magnetite. The SIRM continuously demagnetizes during cooling from 300 to 10 K for the synthetic samples, and the remanence is irreversible during warming with respect to cooling. The remanence at room temperature after LTC for samples S706 and S504 is ~73% and 79% of the initial SIRM, respectively. For typical SD sedimentary greigite from Italy (Florindo and Sagnotti, 1995), SIRM gradually increases upon cooling from 300 to 10 K (Fig. 4.3a), although upon warming the process is not completely reversible with respect to cooling, as SIRM gradually decreases to ~96% of the initial room-temperature SIRM value. The Czech Republic sample (Krs et al., 1990; Hoffmann, 1992) with mixed MD and SD grains (Roberts et al., 2006) has intermediate behaviour between the SD and PSD/MD extremes during LTC (Fig. 4.3a). In magnetite, demagnetization during ZFC of remanence (SIRM, anhysteretic remanence and /or thermoremanence) has been well documented (Petrova and Trukhin, 1961; Markov et al., 1983) to depend on domain state; small SD grains do not demagnetize, while larger

MD magnetite demagnetizes irreversibly upon cooling to above the Verwey transition. This irreversible demagnetization has been associated with domain re-ordering, i.e., domain wall re-equilibration or domain nucleation due to temperature-dependent changes in magnetocrystalline anisotropy and trans-domain processes (Muxworthy et al., 2003). The studied synthetic greigite samples undergo continuous demagnetization of SIRM during ZFC of LTC (Fig. 4.3a). This decrease is probably due to identical PSD/MD processes that cause the remanence to decrease on cooling in magnetite. The observed demagnetization during LTC for the synthetic greigite samples provides further indirect evidence of the dominance of PSD/MD behaviour. In contrast, almost no magnetic memory is lost for the Italian SD greigite sample. The remanence increase for SD samples during cooling is probably associated with the change in M_s with temperature.

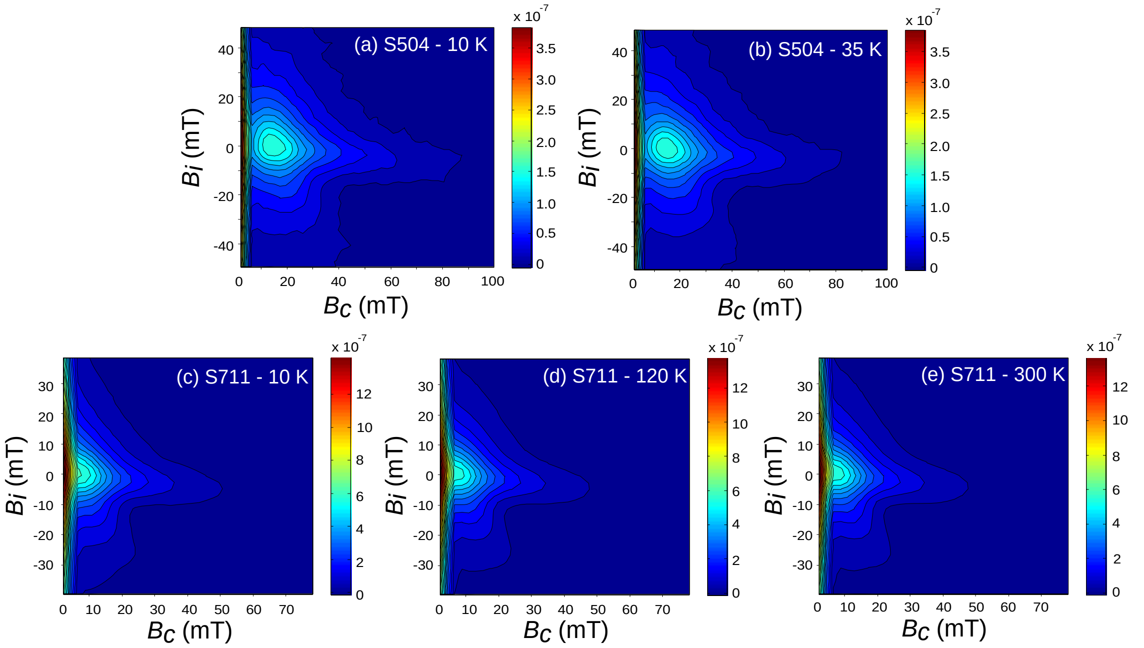

Figure 4.2. Low-temperature FORC diagrams for a dominantly PSD greigite sample (S504) at (a) 10 K and (b) 35 K, and for a dominantly MD greigite sample (S711) at (c) 10 K, (d) 120 K, and (e) 300 K.

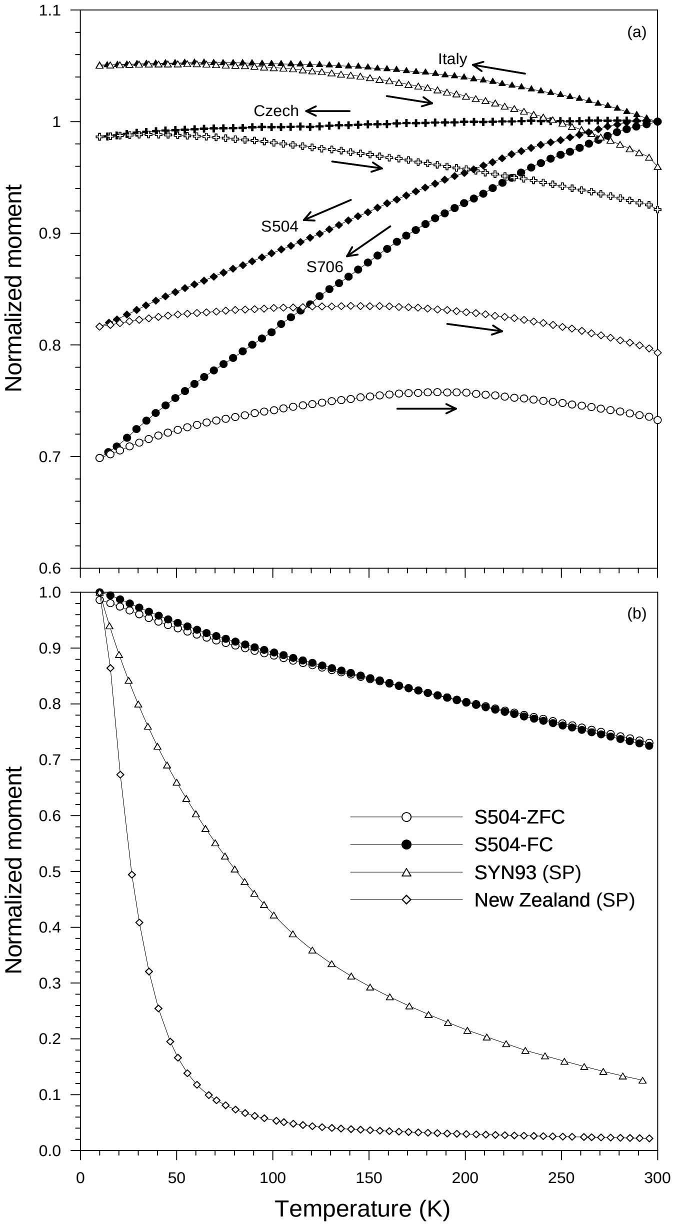

Figure 4.3. (a) Normalized zero-field cooling (solid symbols) and warming (open symbols) of SIRM for greigite samples. Circles, synthetic sample S706; diamonds, synthetic sample S504; triangles, 'Italy'; crosses, 'Czech'. (b) Normalized SIRM warming curves for synthetic greigite sample S504 during zero-field warming from 10 K to 300 K after ZFC (open circles) and FC (solid circles) treatments. SIRM warming curves are also plotted for a synthetic SP greigite sample (triangles) (Roberts, 1995; Figure 4) and for sedimentary greigite with dominant SP behaviour from eastern New Zealand (Rowan and Roberts, 2006).

The lack of a low-temperature transition or even a magnetic isotropic point (where the magnetocrystalline anisotropy is zero and changes signs) in low-temperature SIRM warming curves (Fig. 4.3b) is consistent with the findings of Moskowitz et al. (1993) and Roberts (1995). The synthetic PSD/MD greigite samples undergo a small remanence drop during warming, unlike greigite samples with substantial SP behaviour, which undergo a large decrease in remanence (cf. Fig. 4 of Roberts (1995)). The SIRM decrease for PSD/MD greigite during warming can be attributed to domain wall unpinning (Moskowitz et al., 1998). Sedimentary greigite from New Zealand with dominant SP behaviour undergoes a large low-temperature decrease in remanence (Fig. 4.3b), in agreement with the interpretation of Rowan and Roberts (2006). For magnetite, ZFC and FC SIRM warming curves diverge below the Verwey transition due to magnetocrystalline anisotropy re-orientation (e.g., Moskowitz et al., 1993). However, for greigite, which apparently has no crystallographic transition, the two curves overlap, which is consistent with the results of Moskowitz et al. (1993) for one natural greigite sample.

4.5. Discussion and Conclusions

The studied synthetic greigite samples are dominated by PSD/MD magnetic behaviour, as demonstrated with FORC diagrams, LTC-SIRM and low-temperature SIRM warming measurements. SEM observations reveal that the studied synthetic samples have a broad grain size distribution with a maximum grain size of ~44 μm (Fig. 4.1h-k). Compared to magnetite, the observed grain-size ranges for the synthetic greigite samples span those expected for PSD and MD grains. On a Day plot (Day et al., 1977), data for the synthetic samples fall on a trend calculated for mixtures of SD and MD magnetite (Dunlop, 2002), although strict numerical comparison between greigite and magnetite can not be made. By contrast, data from sedimentary greigite samples from New Zealand (Rowan and Roberts, 2006) follow a trend that resembles theoretical SP-SD mixing curves (Dunlop, 2002). Differences in magnetic properties amongst the studied synthetic greigite samples are related to the different grain size distributions (Fig. 4.1h-k). Sample S626 (mean grain size d = 13 ± 5 μm) has low M_{rs}/M_s (0.08) and high B_{cr}/B_c (3.23) values (Fig. 4.1a), and the FORC distribution has clearly divergent contours (Fig. 4.1g). By contrast, sample S504 (d < 4 μm) contains finer particles attached to the surface of large greigite crystals (Fig. 4.1h) and yields higher M_{rs}/M_s (0.26) and lower B_{cr}/B_c (1.63) values (Fig. 4.1a). The FORC distribution for this sample also contains concentric contours, which indicate the presence of PSD grains (Fig. 4.1d). This is consistent with the relatively smaller fraction of remanence lost during LTC for sample S504 compared to sample S706 (d = 8 ± 4 μm) (Fig. 4.3a).

This study demonstrates that synthetic PSD/MD greigite can be produced in the laboratory, just as coarse-grained sedimentary greigite can sometimes be preserved in natural environments (Hoffmann, 1992). Rowan and Roberts (2006) found that SP behaviour may be common in rapidly-deposited marine sediments, which means that use of classic SD properties to identify greigite (cf. Roberts, 1995) will lead to widespread underestimation of its presence in sediments. Likewise, our results for PSD/MD greigite indicate that its coercivity overlaps with that of PSD/MD magnetite and the lack of a low-temperature transition in greigite can also overlap the low-temperature behaviour for maghemite or partially oxidized magnetite, which means that the presence of PSD/MD greigite in sediments is also likely to be underestimated unless additional high- and low-temperature measurements are made. Regardless, characterization of the full range of magnetic properties of greigite, to which this paper contributes, is necessary to enable identification of greigite in natural environments and will lead to a better understanding of greigite diagenesis. Such an improved understanding of the magnetic properties and occurrence of greigite will be important for a range of environmental magnetic and palaeomagnetic studies.

Chapter 5

Fundamental magnetic parameters from pure synthetic greigite

This chapter was published in the *Journal of Geophysical Research – Solid Earth*, Volume 113, Chang, L., A. P. Roberts, Y. Tang, B. D. Rainford, A. R. Muxworthy, and Q. Chen, Fundamental magnetic parameters from pure synthetic greigite (Fe_3S_4), B06104, doi:10.1029/2007JB005502, 2008. Copyright (2008), with permission of the American Geophysical Union.

Abstract Pure ferrimagnetic greigite has been synthesized by reacting ferric chloride with thiourea and formic acid at 170°C. Sample purity was confirmed by X-ray diffraction, neutron diffraction and Mössbauer spectroscopy, coupled with magnetic measurements. Scanning electron microscope observations indicate clear cubo-octahedral and polyhedral crystal morphologies. The grain sizes are as large as 44 μm. Detailed low- and high-temperature magnetic measurements document the previously poorly known magnetic properties of greigite. The synthetic greigite samples are dominated by pseudo-single-domain and multi-domain behaviour. The saturation magnetization (M_s) at room temperature is ~59 Am^2kg^{-1} (3.13 μ_B per formula unit), which is higher than any value previously reported for greigite in the literature largely because of the high purity of this sample compared to others. No low-temperature magnetic transition has been detected; however, a local coercivity minimum is observed at around 130 K, which is probably associated with domain walls present in the studied samples. The high-temperature magnetic properties of greigite are dominated by chemical decomposition above around 250°C, which precludes determination of the Curie temperature, but our evidence indicates that it must exceed 350°C. Based on the Bloch spin wave expansion, the spin wave stiffness of greigite was determined for the first time as ~193 meV·$Å^2$ from low-temperature M_s measurements, with the corresponding exchange constant J_{AB} of ~1.03 meV.

5.1. Introduction

Greigite is an iron thiospinel that was first formally discovered in lake sediments from California by Skinner et al. (1964). Greigite was inferred to have the inverse spinel structure, the same as its iron oxide counterpart, magnetite (Skinner et al., 1964). Greigite has attracted considerable attention owing to its magnetic and electrical properties (e.g., Coey et al., 1970; Spender et al., 1972; Vaughan and Tossell, 1981; Goodenough and Fatseas, 1982; Braga et al., 1988; Vandenberghe et al., 1991; Letard et al., 2005; Pearce et al., 2006; Rickard and Luther, 2007). In nature, greigite forms under anoxic, sulphate-reducing conditions and is being increasingly identified in anoxic marine and lake sedimentary systems and is now recognized as a widespread magnetic mineral (Roberts and Weaver, 2005, and references therein). As a recorder of the ancient geomagnetic field and environmental processes, greigite can be important for palaeomagnetic and environmental magnetic studies (e.g., Snowball and Thompson, 1988, 1990; Snowball, 1991; Tric et al., 1991; Roberts and Turner, 1993; Roberts et al., 1996; Jiang et al., 2001; Roberts et al., 2005; Rowan and Roberts, 2006; Babinszki et al., 2007; Ron et al., 2007; Vasiliev et al., 2007). Magnetotactic bacteria that produce greigite magnetosomes are also a potentially widespread source of greigite in nature (e.g., Farina et al., 1990; Mann et al., 1990; Heywood et al., 1991; Bazylinski et al., 1993, 1995; Pósfai et al., 1998a, b; Kasama et al., 2006a, b). As a precursor to pyrite in the Fe-S system, greigite is significant in the pyritization process and in Fe-S geochemistry (e.g., Berner, 1984; Benning et al., 2000; Hunger and Benning, 2007). Greigite is therefore of interest in multiple disciplines, including geophysics, geochemistry, physics, biology and material science.

The magnetic properties of greigite have been extensively studied. Coey et al. (1970) found that greigite is ferrimagnetic with the Néel spin configuration, which should have a net magnetic moment of $\geq 4\ \mu_B$ considering the spin-only values for the ionic moments. Coey et al. (1970) could not account for the measured magnetic moment of only $(2.2\pm0.2)\ \mu_B$ per formula unit (f.u.). They inferred that electron hopping occurs between high-spin ferric and ferrous iron in octahedral sites. Spender et al. (1972) presented two alternative band schemes to account for the semiconductor properties of greigite. Goodenough and Fatseas (1982) investigated the valence state of iron using the Mössbauer ^{57}Fe isomer shift. They argued that the reduction of the magnetic moment in greigite compared to that predicted for the Néel spin configuration might be due to a charge transfer from the $S^{2-}\ 3p^6$ valence band to the octahedral site Fe $3d^6$ bands or to a delocalization of the Fe $3d$ electrons that form bonds with S atoms. Braga et al. (1988) made spin-polarized multiple-scattering calculations to investigate the electronic structure of greigite. Their calculations indicate that both the Fe^{2+} and Fe^{3+} high-spin configurations are expected in greigite and that the net magnetic moment per formula unit is ~3.02 μ_B/f.u.. Letard et al. (2005) measured X-ray magnetic circular dichroic spectra on greigite and attributed differences in the spectra between greigite and magnetite to the presence of iron vacancies in greigite. Numerous other magnetic properties of greigite have also been reported in many palaeomagnetic, rock magnetic and environmental magnetic studies (e.g., Snowball and Thompson, 1988, 1990; Snowball, 1991; Hilton, 1990; Tric et al., 1991; Hoffmann, 1992; Roberts and Turner, 1993; Fassbinder and Stanjek, 1994; Roberts, 1995; Dekkers and Schoonen, 1996; Roberts et al., 1996; Sagnotti and Winkler, 1999; Dekkers et al., 2000; Rowan and Roberts, 2006; Roberts et al., 2006).

Despite the importance of greigite, and the many published studies of its magnetic properties, its fundamental magnetic characteristics remain relatively poorly known. For example, published values for the M_s of greigite at room temperature are much lower than for magnetite (Table 5.1). This might be a result of difficulties in producing pure greigite samples because greigite is an intermediate product in reactions that form pyrite (Berner, 1984). Greigite therefore normally occurs in association with pyrite in natural environments. Natural greigite usually grows on the surface of other iron-bearing minerals (Jiang et al., 2001; Roberts and Weaver, 2005), which makes it extremely difficult to separate magnetically from the other minerals and therefore to obtain pure natural samples. Although various methods have been proposed to synthesize greigite in the laboratory, including hydrothermal (Yamaguchi and Katsurai, 1960; Uda, 1965; Yamaguchi and Wada, 1969; Dekkers and Schoonen, 1996), anhydrous (Nakazawa and Sakaguchi, 1972), toluene-thermal (Qian et al., 1999), solution-based hydrothermal (Chen et al., 2005), and modified hydrothermal processes (He et al., 2006), it is difficult to produce pure synthetic greigite because most procedures simultaneously produce other iron sulphides such as mackinawite and pyrite. Most greigite syntheses suffer either from back reaction on cooling back to room temperature or from the fact that greigite can easily react to pyrite in the presence of sulphidic sulphur because of its metastability. Additionally, synthetic greigite samples for which magnetic results have been reported in the literature usually have small particle sizes and/or poor crystallinity.

Other magnetic properties of greigite also remain poorly understood. For example, the magnetic structure of greigite is not clear. Greigite, unlike magnetite, which undergoes a crystallographic phase transition at ~118 K (Verwey, 1939), has had no similar low-temperature transition detected (Coey et al., 1970; Spender et al., 1972; Moskowitz et al., 1993; Roberts, 1995; Chang et al., 2007). Moreover, the easy axis of magnetization for greigite is the [100] crystallographic axis instead of the [111] crystallographic axis for magnetite at room temperature (Yamaguchi and Wada, 1970; Heywood et al., 1991; Bazylinski et al., 1993). That is, the magnetocrystalline anisotropy is cubic with the first anisotropy constant positive, as is the case for metallic iron. To the authors' knowledge, the exchange constants and anisotropy constants have not been previously reported, although Diaz-Ricci and Kirschvink (1992) modelled various domain state configurations for greigite based on rough estimates of these parameters, assuming magnetite-like behaviour. Thermal decomposition of greigite at

Table 5.1. Summary of grain sizes and M_s values reported in the literature for greigite.

Greigite sample	Lattice parameter/(Å)	Morphology & Grain size	Domain state	M_s	Reference
Sediment	9.876	400-500 nm	?	?	Skinner et al. (1964)
Synthetic	9.90	30-50 nm	SP	24 Am^{2}kg^{-1}	Uda (1965)
Synthetic	9.85	Spherical ~50 nm	?	?	Yamaguchi & Wada (1969)
Synthetic	9.86	10-15 nm	SP dominated	2.0 ± 0.3 μ_B/f.u.	Coey et al. (1970)
Synthetic	9.83 - 9.87	~9-14 nm	SP dominated	2.2 ± 0.3 μ_B/f.u.	Spender et al. (1972)
Synthetic	?	Platelet, needle & disk-like <65 nm	?	?	Horiuchi et al. (1974)
Magnetosomes	?	75 nm	SD	?	Mann et al. (1990)
Magnetosomes	?	50-90 nm	SD	?	Heywood et al. (1991)
Sediment	9.88	< 4-8 μm	PSD/MD	~20 Am^{2}kg^{-1}	Hoffmann (1992)
Synthetic	?	<150-400 nm	SP & SD	3~29 Am^{2}kg^{-1}	Dekkers and Schoonen (1996)
Magnetosomes	?	rectangular, arrowhead-shaped 30-120 nm	SD	?	Pósfai et al. (1998a, b)
Synthetic	?	25 nm	?	?	Qian et al. (1999)
Synthetic	?	10 nm wide acicular, 100 nm irregular	SD	19.7 & 38.5 Am^{2}kg^{-1}	Chen et al. (2005)
Synthetic	?	plates, polyhedral, ~3 μm	PSD/MD?	28.6 & 44.7 Am^{2}kg^{-1}	He et al. (2006)
Magnetosomes	?	rectangular, random shapes	SD	?	Kasama et al. (2006a, b)
Synthetic	9.872	cubo-octahedral, polyhedral 13 μm (<1-44 μm)	PSD/MD dominated	59 Am^{2}kg^{-1} 3.13 μ_B/f.u.	This study; Chang et al. (2007)

elevated temperature has precluded determination of its Curie temperature.

In this paper, we report magnetic results for hydrothermally synthesized pure greigite samples with good crystallinity produced using a new method (Tang et al., 2007). These greigite samples appear to be the purest samples yet synthesized and have much larger grain sizes than any previously reported. We have therefore used these samples to determine some of the fundamental magnetic parameters for greigite that were previously either unknown or poorly constrained.

5.2. Greigite synthesis and mineralogical and magnetic characterization

Greigite samples were synthesized using a new hydrothermal method proposed by Tang et al. (2007) in which ferric chloride is reacted with thiourea and formic acid. Thiourea was used as a sulphur source to produce H_2S. All chemical reagents were analytical grade and purchased from Shanghai Chemical Reagents Company. To synthesize greigite, 3.0432 g of stoichiometric analytical grade $FeCl_3 \cdot 6H_2O$ was first dissolved in 100 ml of distilled water that had been purged with N_2 gas for at least half an hour to remove dissolved oxygen. 1.0465 g of thiourea was then added into the solution. After stirring for five minutes, 8.6 ml of formic acid was added into the mixed solution. The solution, which has pH below 4, was transferred into three Teflon-lined 60-ml stainless steel autoclaves. The hydrothermal reaction proceeded at 170°C for eight hours after sealing the autoclaves. Longer reaction times, e.g., 24 hours, result in marcasite (FeS_2) contamination (Tang et al., 2007). During synthesis, N_2 was passed through the solution to prevent oxidation. After reaction, the autoclave was naturally cooled to room temperature. The filtered black precipitates were washed first with carbon disulphide to remove residual sulphur, and were then repeatedly washed alternately with distilled water and absolute ethanol. Finally, the material was dried in vacuum at 40°C for 4 hours. A black powder was obtained.

The recipe for synthesizing greigite proposed by Tang et al. (2007) is different from the traditional hydrothermal method in which a sodium sulphide solution is mixed with Mohr's salt (ferrous ammonium sulphate) (Yamaguchi and Katsurai, 1960; Uda, 1965; Yamaguchi and Wada, 1969; Dekkers and Schoonen, 1996). In this new hydrothermal method, different iron and sulphur sources are used, and, after reaction, the autoclave is naturally cooled to room temperature rather than by quenching in cold water. Many studies suggest that quenching the reaction is essential to produce higher purity greigite samples (Uda, 1965; Yamaguchi and Wada, 1969; Dekkers and Schoonen, 1996). Regardless, this hydrothermal method and others (Qian et al., 1999; Chen et al., 2005) consistently indicate that naturally cooling can also produce high quality greigite samples.

The samples were immediately characterized by XRD analysis after synthesis using a Phillips X'pert X-ray diffractometer with high-intensity Cu-Kα radiation (λ=1.54056 Å) at a scanning speed of 0.05°/s, with a 2θ range from 10 to 70° at the Department of Materials Science & Engineering, University of Science and Technology of China, Hefei, China. The samples were also characterized using SEM observations, which were made with a LEO 1450VP SEM, operated at 10-20 keV with an acceleration voltage of 17-20 pA at the National Oceanography Centre, Southampton (NOCS), University of Southampton, U.K. Mössbauer spectra were measured at the Institute for Rock Magnetism (IRM), University of Minnesota, U.S.A., both at variable temperatures and applied fields using a conventional constant acceleration drive and a ^{57}Co source. The applied magnetic field was parallel to the γ-ray path. A least-squares fit was used to decompose the spectra into sub-spectra that correspond to different distributions of hyperfine interaction parameters. The ^{57}Fe isomer shifts are relative to α-Fe measured at room temperature. Low- and high-temperature magnetic hysteresis loops and backfield magnetizations enabled determination of B_c, B_{cr}, M_r and M_s using an automated Princeton Measurements Corporation vibrating sample magnetometer with low- and high-temperature attachments (to maximum applied fields of 1 T) at the IRM. M_s and ZFC and FC magnetization measurements were made from 5 K to room temperature using a Quantum Designs MPMS. Hysteresis loops were measured between +5 T and –5 T using the MPMS at the IRM. Thermomagnetic measurements were made at the NOCS using a variable field translation balance (VFTB), with heating up to 700°C in air, an applied field of 27 mT and a heating/cooling rate of 10°C/minute.

5.3. Results

5.3.1. Mineralogical characterization

After synthesis, the greigite samples were immediately subjected to XRD analysis to assess sample purity. Greigite is the only detectable phase (Fig. 5.1). Rietveld refinement confirms that greigite has an inverse spinel structure with a cubic close-packed sulphur array (space group $Fd\bar{3}m$). The refined crystallographic lattice parameter is comparable to values reported in the literature (Table 5.1). The low background signal and the strong and narrow diffraction peaks also indicate good crystallinity, which is further confirmed by SEM observations (Fig. 5.2). Greigite single crystals are clearly evident with variable morphology. However, most of the particles have equi-dimensional cubo-octahedral crystal habits. Elongation of the [111] or [100] crystallographic axes produces plate-like or prism-like crystals. Unusual polyhedral morphologies also occur, but they are rare. SEM observations indicate that this greigite sample has a range of grain sizes (Fig. 5.3; see also Chang et al. (2007)). This sample is much coarser-grained than other synthetic and natural greigite samples described in the literature (Table 5.1). Due to the resolution limit of the SEM, the finest greigite particles could not be counted when determining the grain size distributions. This synthetic greigite sample is also made up of mechanically soft grains, as indicated in Fig. 5.2 in which many crystals are physically crushed. This is not surprising as the hardness of greigite is in the 4-4.5 range (Mohr's scale) (Radusinović, 1966) (it should be noted that any literature estimate of the hardness of greigite will have been made from impure samples, so this estimate is probably too high because of the presence of mechanically harder minerals in an impure sample. The presence of extremely fine particles will affect the magnetic properties of the sample, especially by producing SP behaviour in ultrafine magnetic particles (Néel, 1949), which is evident in the Mössbauer and magnetic results described below.

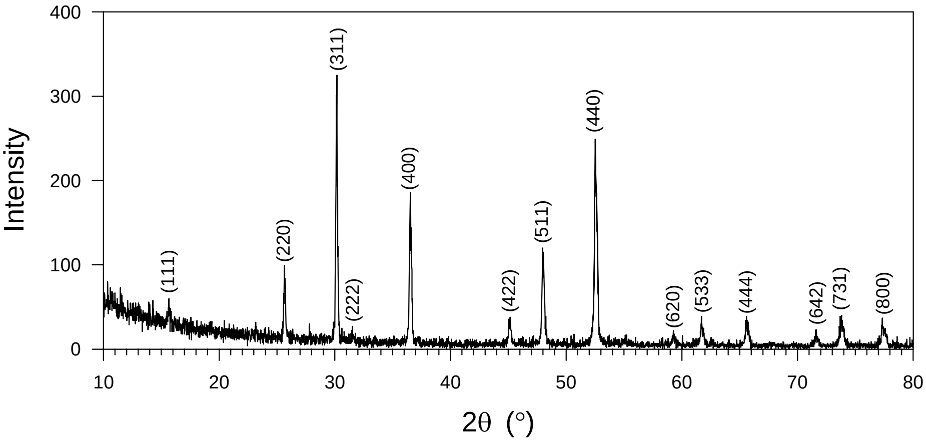

Figure 5.1. XRD pattern for the studied hydrothermally synthesized greigite sample at room temperature. The Miller indices of the main Bragg reflections are labeled.

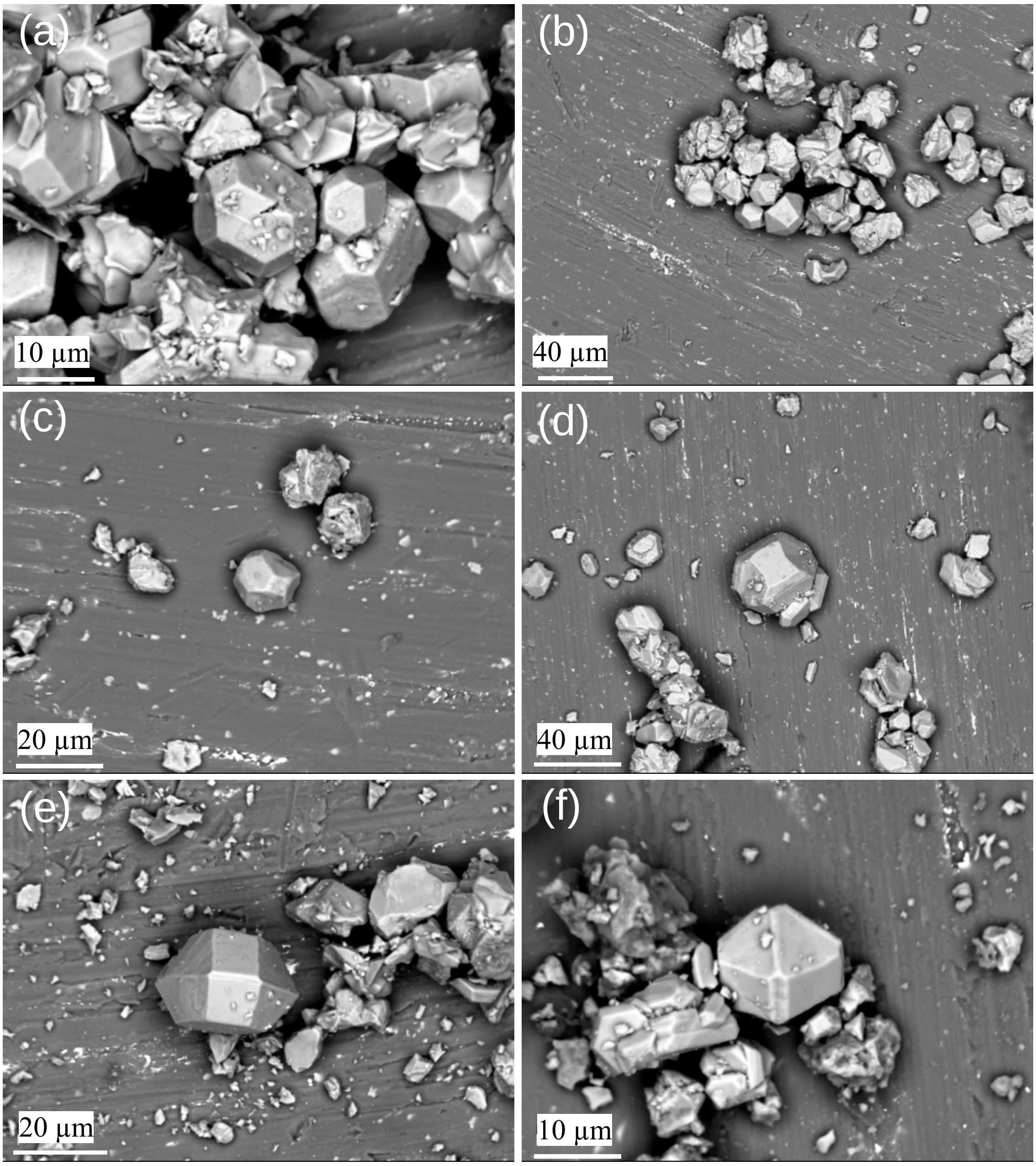

Figure 5.2. Back-scattered electron images that illustrate the morphology and particle sizes of the studied synthetic greigite samples.

The purity of the studied greigite sample is further confirmed by other complementary measurements, e.g., neutron diffraction (Chapter 6), Mössbauer spectroscopy and magnetization measurements. This confirmation is important because amorphous phases are not detectable using XRD. The synthesis of pure greigite samples in this study is significant because it is the first time that such a pure greigite sample has been synthesized. This makes it possible to rigorously determine some of the fundamental magnetic parameters for greigite for the first time.

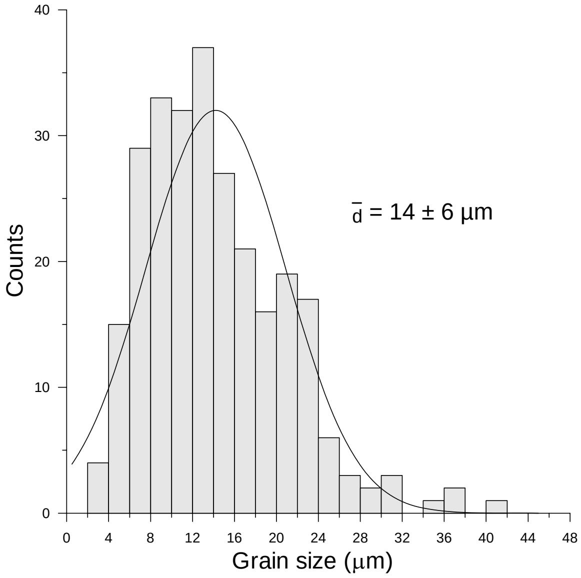

Figure 5.3. Histogram of the grain size distribution for the principal synthetic greigite sample studied in this paper, as determined from ~200 grain counts from SEM observations.

5.3.2. Mössbauer spectroscopy

Mössbauer spectra were measured for the studied greigite samples both at room temperature and at low temperatures. The experimental spectra are shown in Fig. 5.4 and the hyperfine interaction parameters, including the hyperfine field and the isomer shift obtained from analysis of the spectra, are listed in Table 5.2. At room temperature, the spectrum represents a superposition of a quadrupole doublet and two magnetic sextets. The two magnetic sextets are attributed to hyperfine interactions in the octahedral and tetrahedral sites in greigite. The quadrupole doublet is probably associated with thermally relaxed fine particles present in the measured sample. B_{eff} of the tetrahedral and octahedral sites for the studied greigite sample at room temperature is 31.2 and 31.5 T, respectively, while δ for the two sites is 0.29 and 0.53 mm/s, respectively. At 50 K, the Mössbauer spectrum is composed only of the two magnetic sextets that correspond to the two magnetic sublattices of greigite. The absence of the room temperature quadrupole doublet in the Mössbauer spectrum at low temperatures is an indication of SP behaviour in the studied samples. At 4 K, the central quadrupole doublet disappears, while the two magnetic sextets are well defined in the Mössbauer spectrum. However, another small poorly defined magnetic sextet with higher B_{eff} (~48.4 T) is fitted to the Mössbauer spectrum at 4 K. This sextet is small and broad, which makes it difficult to determine its origin. However, it is probably associated with iron oxide, e.g., the two magnetic sextet peaks of magnetite or some solid solutions in

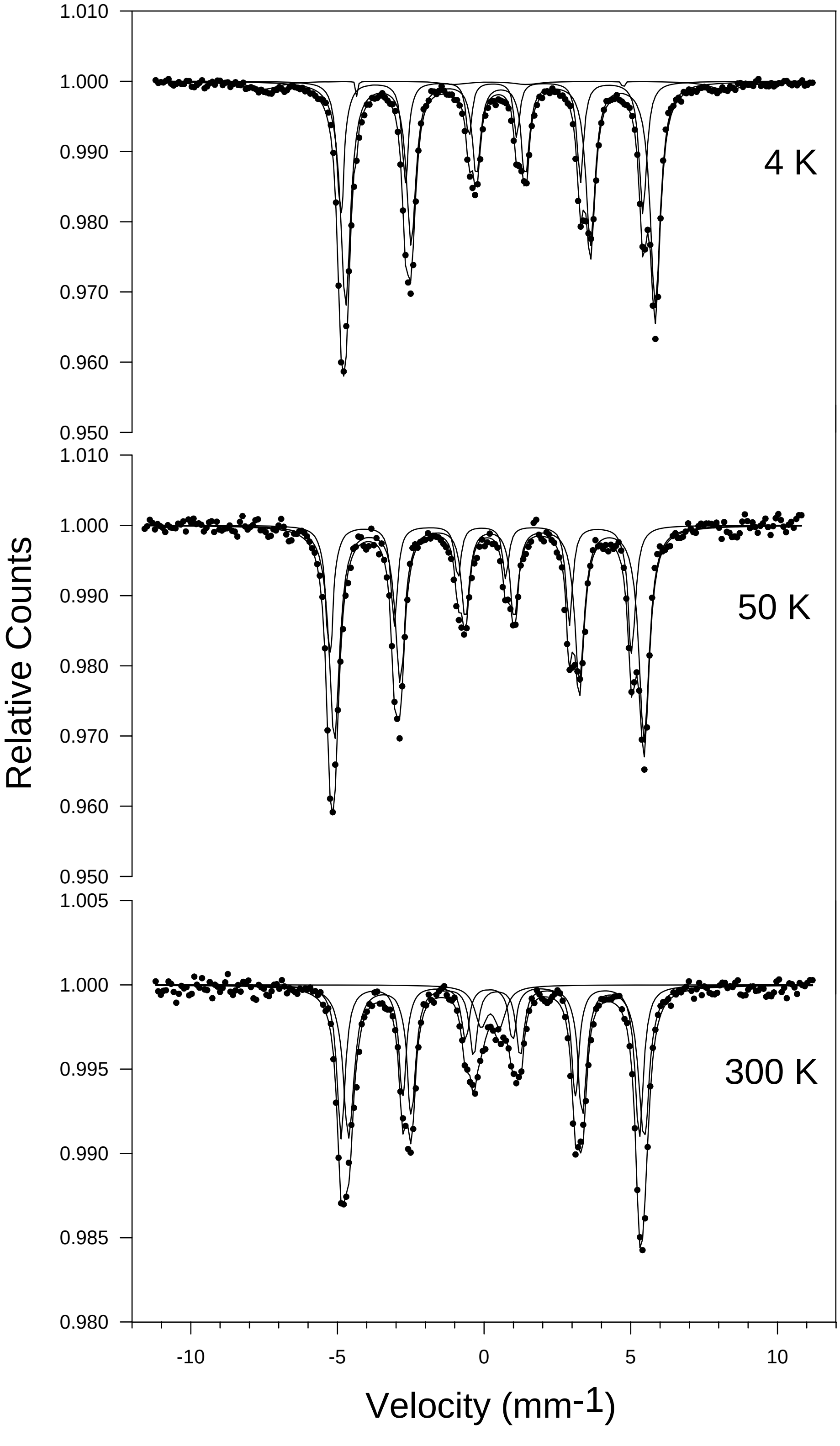

Figure 5.4. ^{57}Fe Mössbauer data (dots) for the studied greigite sample, measured with a ^{57}Co source at various temperatures (4 K, 50 K, and 300 K) in zero applied field. The curves represent the fittings for magnetic sextets and quadrupole doublets.

Table 5.2. Mössbauer hyperfine parameters for the studied greigite samples compared to published values for greigite and magnetite.

Compounds	Temperature (K)	Octahedral sites		Tetrahedral sites	
		Isomer shift (mm/s)	Hyperfine field (T)	Isomer shift (mm/s)	Hyperfine field (T)
greigite[a]	4	0.66	32.7	0.38	31.9
greigite[a]	50	0.66	32.7	0.38	31.9
greigite[a]	RT	0.53	31.5	0.29	31.2
greigite[b]	RT	0.70	31.0	0.41	31.1
greigite[c]	RT	0.53	31.3	0.28	31.3
magnetite[b]	RT	0.82	46.2	0.43	49.4

References: a. This study; b. Coey et al. (1970); Spender et al. (1972); c. Vandenberghe et al. (1991).

the magnetite-maghemite series (Schmidbauer and Keller, 2006). The surface of greigite samples can become oxidized (e.g., Letard et al., 2005; Kasama et al., 2006b), which might be responsible for the observed small magnetic sextet with a high B_{eff} in the Mössbauer spectrum at 4 K. Spender et al. (1972) observed a much more pronounced magnetic sextet with a B_{eff} of ~47 T in the Mössbauer spectrum at 4.2 K. This suggests that the degree of surface oxidation in their samples was high, which is not surprising considering the large surface area to volume ratio for the small (~9 nm) synthetic greigite particles used in their study. Any surficial iron oxides only occur in small amounts in the greigite samples studied here, as indicated by the small and poorly fitted sextet. Its presence in such small quantities should not significantly affect our results.

Applying an external field to a magnetically split Mössbauer spectrum can change the magnetic field at the nucleus and affects the magnetic hyperfine interactions (Fig. 5.5). The nuclear magnetic field (measured B_{eff}) can be expressed (Greenwood and Gibb, 1971) as:

$$B_{eff} = B_{ext} - DM + (4/3)\pi M + B_{int} = B_{ext} - DM + (4/3)\pi M + B_S + B_L + B_D, \qquad (5.1)$$

where B_{ext} is the external applied field, $-DM$ is the demagnetizing field and $(4/3)\pi M$ is the Lorentz field, which are both small. B_{int} is referred to as the internal magnetic field, which is the sum of the Fermi contact term (B_S), the orbital term (B_L) and the dipole term (B_D). B_S originates from the unbalanced spin density of s-electrons at the nucleus.

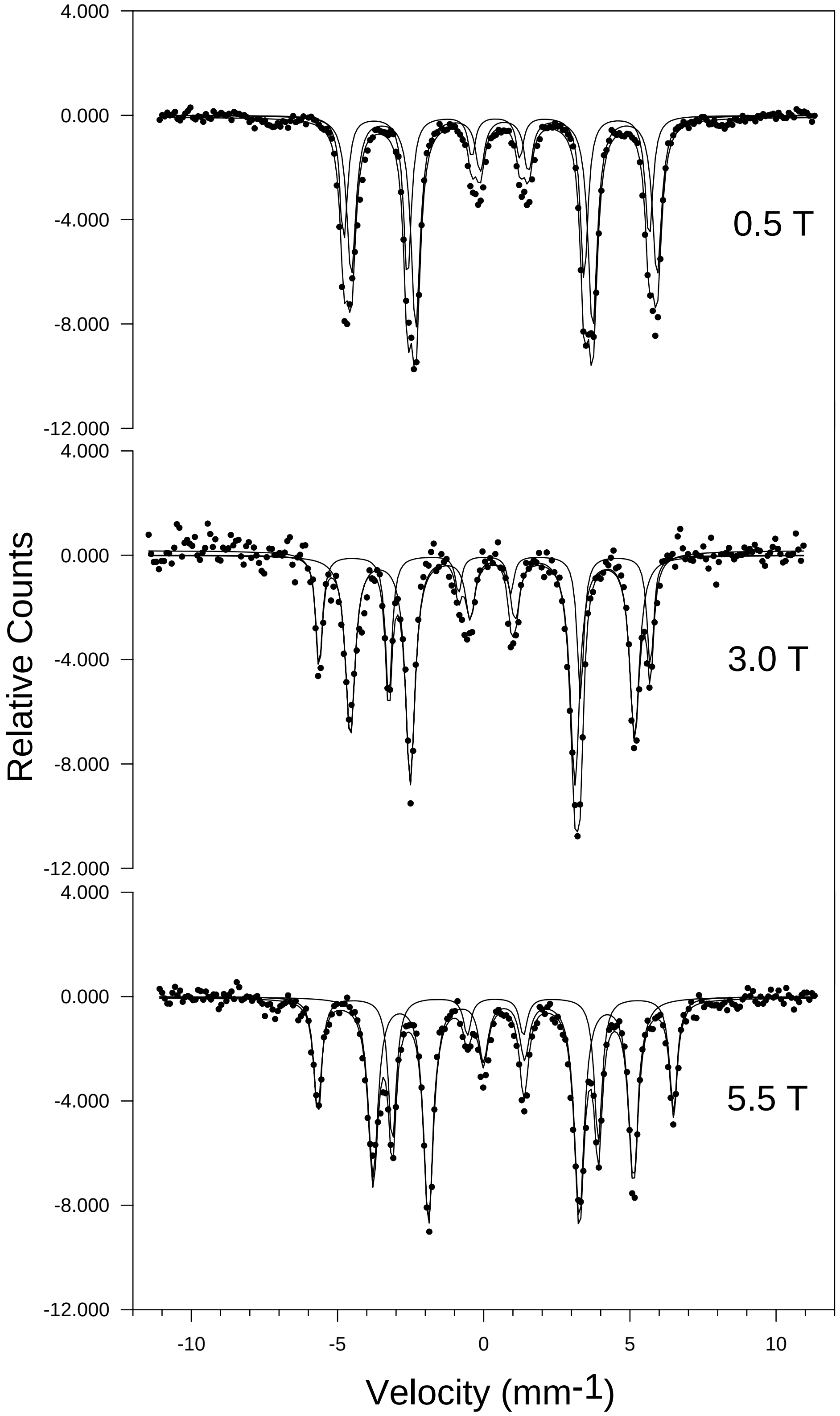

Figure 5.5. ^{57}Fe Mössbauer data (dots) and magnetic sextets (curves) for the studied greigite sample measured at 4 K under various applied fields (0.5 T, 3.0 T, and 5.5 T).

B_L arises from the orbital angular momentum of the ion. For high spin ferric compounds, this term is zero because ferric iron is an S-state ion, ^{6}S. B_D is the field produced at the nucleus by the arrangement of atomic moments throughout the crystal arising from the dipolar interaction of the nucleus with the spin moment of the atom. In cubic symmetry for transition elements, B_D is zero.

The fact that B_{eff} at the octahedral site decreases, whereas B_{eff} at the tetrahedral site increases with increasing B_{ext} (Fig. 5.6) indicates that B_{int} at the sublattices is aligned either parallel at the tetrahedral site or antiparallel to B_{ext} at the octahedral site, which reveals the ferrimagnetic nature of greigite. B_{eff} at the tetrahedral site has a smaller value (Table 5.2) due to the presence of Fe^{3+}. B_{eff} at both sites is nearly collinear with B_{ext} as predicted by Equation 5.1. A crossover of the B_{eff} is observed at ~0.5 T (Fig. 5.6), which is slightly different from previous observations (Coey et al., 1970; Spender et al., 1972).

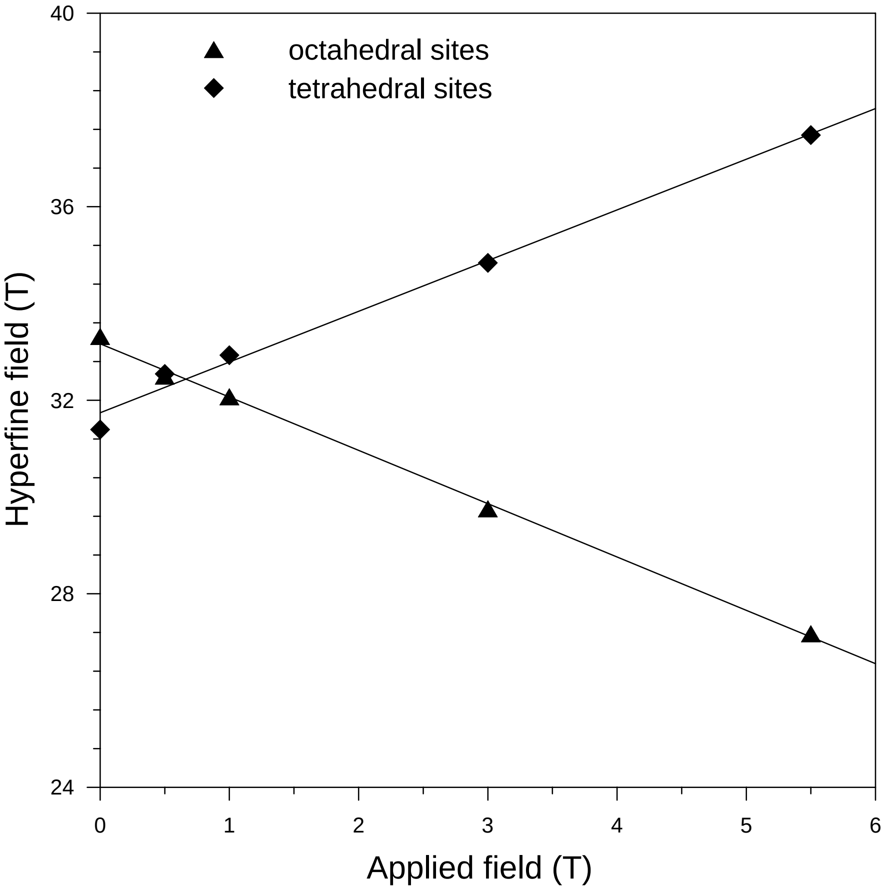

Figure 5.6. Field dependence of the sublattice hyperfine fields (solid triangles: octahedral sites; solid diamonds: tetrahedral sites).

5.3.3. Magnetic properties

5.3.3.1. Saturation magnetization and high-field behaviour

The studied greigite sample is magnetically soft, as suggested by a coercivity B_c of ~7-8 mT and a M_{rs}/M_s ratio of ~0.12 at room temperature. A hysteresis loop for the synthetic greigite sample at 5 K (Fig. 5.7) quickly approaches saturation; however, it is not fully saturated even in a 5 T field. A contribution from spin waves may be responsible for the non-saturation at high fields. Considering the non-saturation at high fields, we use a conventional method to precisely determine the M_s. Magnetization is plotted against $1/B$ (B is the applied field), and we extrapolate the magnetization to $1/B = 0$ to obtain $M(\infty)$ (Fig. 5.8). For a range of greigite samples, the M_s at room temperature is determined to be ~59 Am^{2}kg^{-1} (3.13 μ_B/f.u.) for greigite (Table 5.1). Slightly higher values are observed at lower temperatures because of decreased thermal agitation (Fig. 5.8).

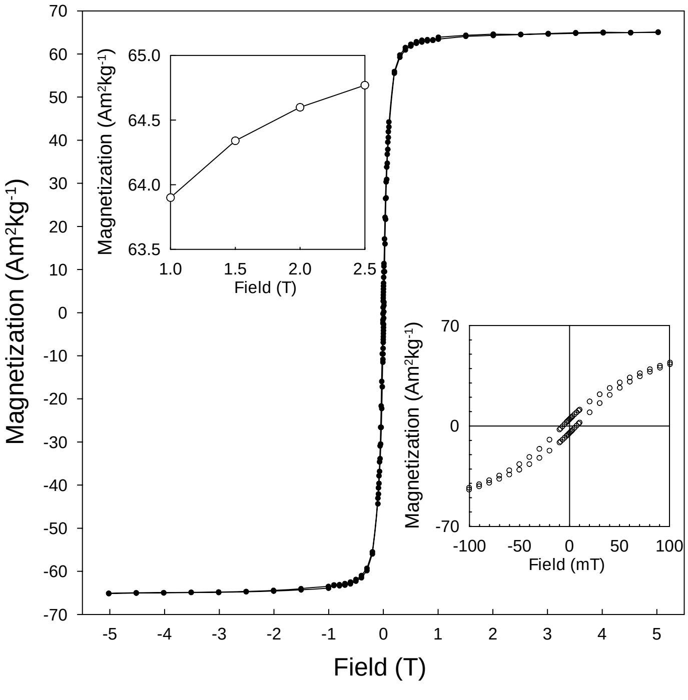

Figure 5.7. Field-dependence of magnetization for the studied greigite sample at 5 K. The insert on the bottom right-hand-side of the figure is an expansion of the central portion of the hysteresis loop, showing the coercivity and saturation remanence, while the insert on the upper left-hand-side of the figure contains the high-field approach to saturation magnetization.

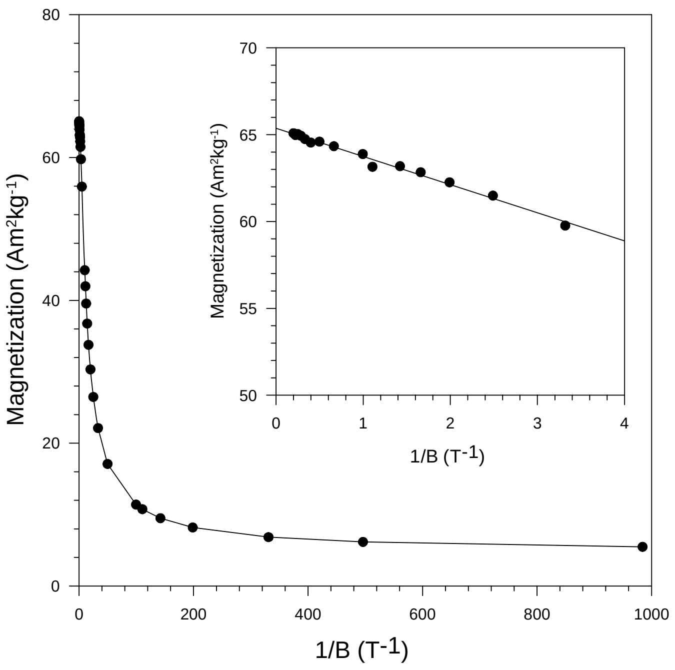

Figure 5.8. Magnetization versus 1/*B* for the studied synthetic greigite sample at 5 K. The insert is a horizontal expansion of the main figure at high fields, which indicates the approach to saturation. The same approach was used at room temperature, with extrapolation of the magnetization to 1/*B* = 0 to obtain the M_s value for a range of samples.

5.3.3.2. Low-temperature properties

No low-temperature magnetic transitions were detected in any of the low-temperature measurements. This contrasts with magnetite, which undergoes a Verwey transition at 118 K (Verwey, 1939), and is consistent with previous reports for greigite (e.g., Coey et al., 1970; Spender et al., 1972; Moskowitz et al., 1993; Roberts, 1995) and other low-temperature magnetic measurements for the same synthetic greigite samples (Chang et al., 2007). Variations in ZFC/FC magnetization curves measured in a 2 mT field are small, however, a clear maximum magnetization is observed at ~160 K in the ZFC curve (Fig. 5.9), which is likely to indicate the presence of SP behaviour in a fraction of the measured particles. M_s undergoes a 7.1% decrease from 5 K to room temperature (Fig. 5.10) due to increased thermal fluctuations. The variation of B_c is small at low temperatures (Fig. 5.11), as is often the case for natural SD greigite samples (Roberts, 1995). Despite the small change of coercivity at low temperatures, a clear local coercivity minimum was observed at ~130 K. In order to check this property, we measured low temperature hysteresis loops for three synthetic greigite samples produced using the same hydrothermal method, which provides identical results (Fig.

5.11). This confirms that the local coercivity minimum at ~130 K is a genuine magnetic property of greigite.

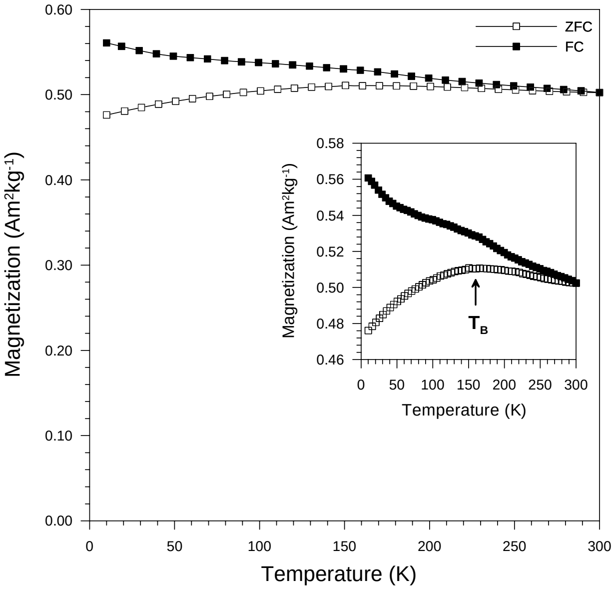

Figure 5.9. DC susceptibility versus temperature (at *B* = 2 mT) both in ZFC and FC conditions for the studied synthetic greigite sample. The insert is an expansion of the magnetization curves, which clearly indicates a blocking temperature at ~160 K due to the presence of fine grains with SP behaviour.

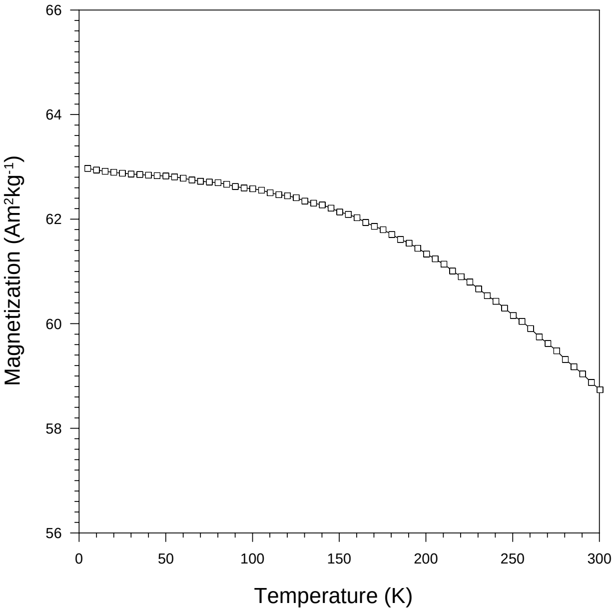

Figure 5.10. Low-temperature measurements of M_s for the studied greigite sample during warming from 5 K to 300 K measured in a field of 5 T. The M_s only decreases by 7.1% from 5 K to 300 K.

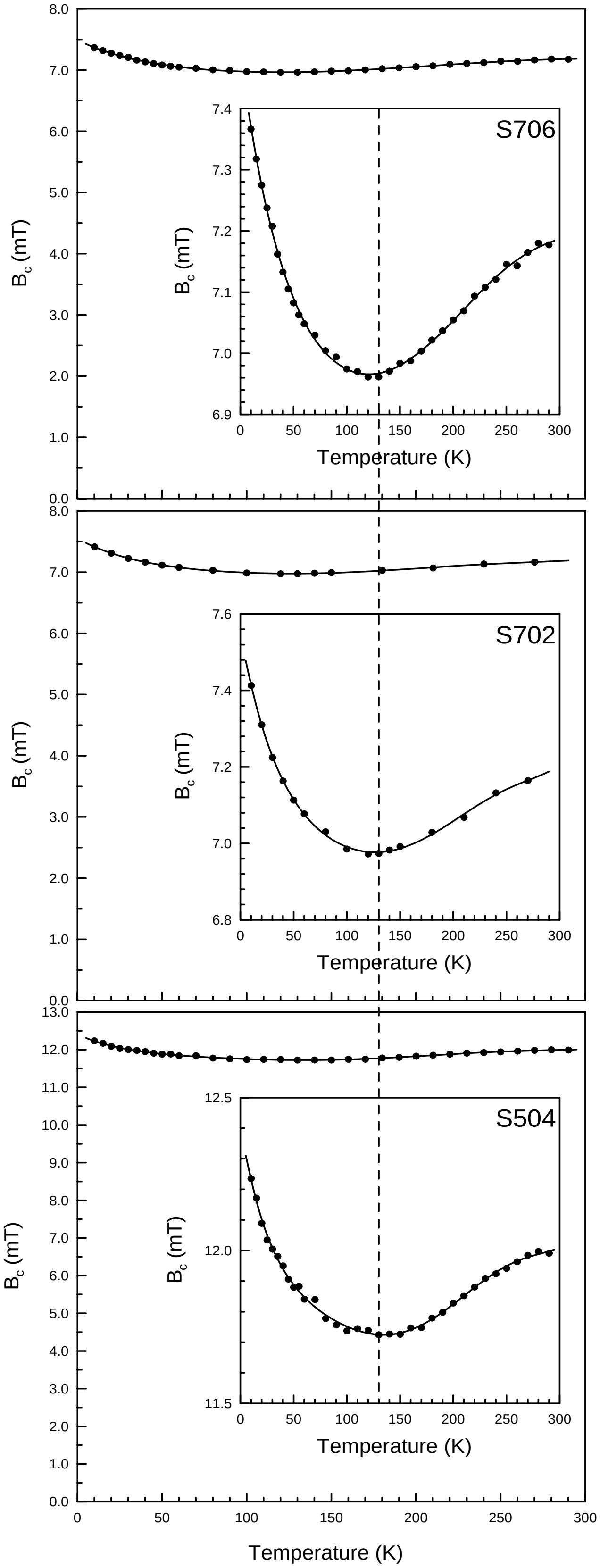

Figure 5.11. Temperature dependence of coercivity for three synthetic greigite samples at low temperatures. An apparent local coercivity minimum is observed at around 130 K for separate batches of the hydrothermally synthesized greigite.

5.3.3.3. High-temperature properties

High-temperature hysteresis data (measured in air) reveal a significant break in slope at ~250°C (Fig. 5.12), which indicates the onset of thermal decomposition of the studied greigite sample, as is widely known (e.g., Krs et al., 1992; Reynolds et al., 1994; Roberts, 1995; Dekkers et al., 2000). Both B_c and B_{cr} increase above 250°C, which indicates the formation of magnetically 'harder' phases. Thermal alteration has obscured efforts to determine the T_C of greigite.

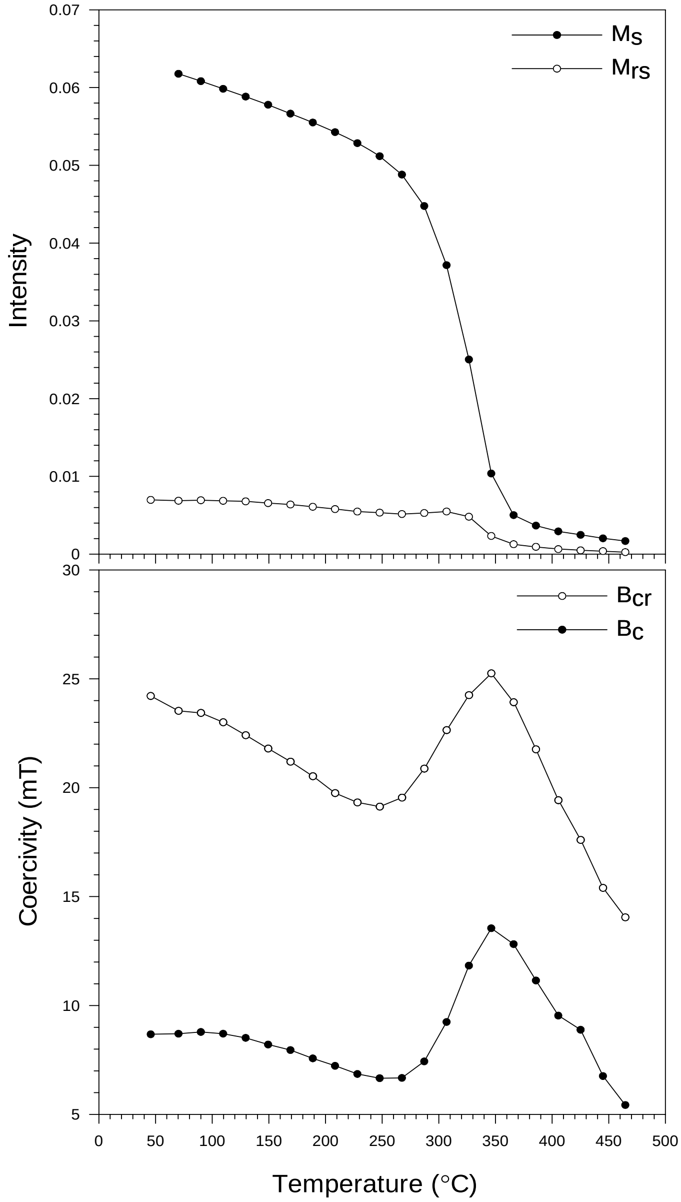

Figure 5.12. Temperature dependence of hysteresis parameters for the studied synthetic greigite sample at high temperatures. The break in slope of M_s at ~250°C indicates the onset of chemical decomposition of the synthetic greigite.

In order to investigate the possibility of a higher value for the T_C of greigite, we have measured high-temperature thermomagnetic curves for a particularly stable natural greigite sample from an iron sulphide nodule from the Valle Ricca section near Rome (cf. Bracci et al., 1985; Florindo and Sagnotti, 1995; van Dongen et al., 2007) (Fig. 5.13). Studies of Italian greigite-bearing sediments have often suggested maximum unblocking temperatures for greigite of up to 380-410°C (e.g., Florindo and Marra, 1995; Mattei et al., 1996; Sagnotti and Winkler, 1999; Sagnotti et al., 2000). The studied sample illustrates this behaviour. Its thermomagnetic curve decreases sharply at ~400°C (Fig. 5.13a). The curve eventually decreases to zero at the T_C of magnetite and is irreversible upon cooling. A peak at ~290°C is intermediate between the T_C of monoclinic pyrrhotite (Fe_7S_8) at 320°C (Dekkers, 1989) and that of hexagonal pyrrhotite (Fe_9S_{10}), which is only ferrimagnetic above ~200°C and which has a T_C of ~265°C (Schwarz and Vaughan, 1972). During a second heating, this phase has clearly fully altered to form monoclinic pyrrhotite, as indicated by an inflection at 320°C during heating and a peak at this temperature during cooling (Fig. 5.13b). Monoclinic pyrrhotite and magnetite appear to be the main magnetic phases present during the second heating run.

In order to test whether the marked decay in magnetization at ~400°C in Fig. 5.13a represents a T_C for a particularly stable greigite sample, a thermomagnetic run was measured on a sister sample to a maximum temperature of 450°C (Fig. 5.13c) in an attempt to minimize thermal alteration. The data demonstrate that thermal decomposition of greigite occurs below 450°C for this sample. The fact that the high-temperature behaviour of greigite is determined more by thermal alteration is evident from results for another sister sample that was subjected to successive thermomagnetic cycles at stepwise increasing maximum temperatures (Fig. 5.13d-f). The thermal cycling indicates progressive increases in magnetization (note the expanded vertical scale) up to about 250°C (Fig. 5.13d). This increase could be similar to the increasing magnetic moments observed by de Boer and Dekkers (1998) when measuring samples in non-saturating fields. These authors stirred their samples between successive thermomagnetic runs to avoid such magnetic changes. We do not stir the samples between thermomagnetic runs, but we do not think that these changes indicate thermal alteration because further increases in magnetization are not observed above 250°C, and the 300 and 350°C cycles are reversible, which indicates that this sample is particularly stable with no discernible thermal alteration up to 350°C. Thermal

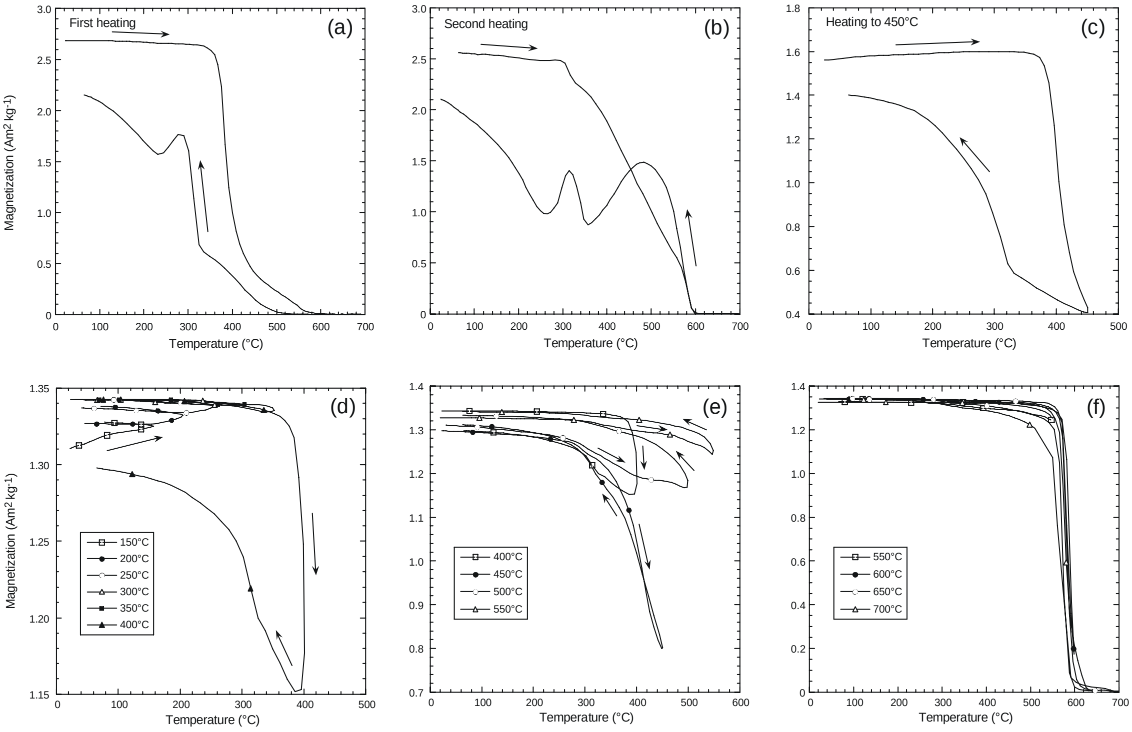

Figure 5.13. Thermomagnetic cycles for different sub-samples of greigite from an iron sulphide nodule from the Valle Ricca section (cf. Bracci et al., 1985; Florindo and Sagnotti, 1995). (a) Thermomagnetic cycle up to 700°C and back to room temperature. (b) Second heating of the sample shown in (a). (c) Thermomagnetic cycle for a fresh sample up to 450°C. Thermal alteration is still evident in the cooling run for this sample. (d) Thermomagnetic cycles for another fresh sample up to progressively increasing maximum temperatures and back to room temperature, including maximum temperatures of 150°C, 200°C, 250°C, 300°C, 350°C, and 400°C. Note the expanded vertical scale in this sub-figure. While slight increases in magnetization are evident up to 300°C, the 350°C curve is reversible, which suggests that the T_C for greigite must lie above 350°C. Thermal alteration is evident in the 400°C cycle. (e) Thermomagnetic cycles up to progressively increasing maximum temperatures and back to room temperature, including maximum temperatures of 400°C, 450°C, 500°C, and 550°C. Progressive thermal alteration is evident in each thermomagnetic cycle. (f) Thermomagnetic cycles up to progressively increasing maximum temperatures and back to room temperature, including maximum temperatures of 550°C, 600°C, 650°C, and 700°C. Each curve indicates that magnetite is present as the main magnetic alteration phase.

alteration is clearly visible, however, in the 400°C cycle, where the heating and cooling curves are not reversible. An inflection in the cooling curve at 320°C suggests the formation of monoclinic pyrrhotite (Fig. 5.13d). Pyrrhotite is clearly indicated in heating and cooling cycles up to 450°C, which is almost reversible (Fig. 5.13e; note the larger vertical scale in this sub-figure). Further thermal alteration, as indicated by irreversibility and increased magnetizations, is evident in the 500 and 550°C cycles. This newly formed phase is magnetite, as indicated by the reversible thermomagnetic curves with T_C of 580°C for cycles up to 600, 650 and 700°C (Fig. 5.13f). While thermal alteration is clearly a major determinant of the high-temperature magnetic properties of greigite, this sample is particularly stable, without thermal alteration (reversible thermomagnetic curves) up to 350°C, which indicates that the T_C of greigite exceeds 350°C.

5.3.4. Evaluation of the exchange constant for greigite

In ferrimagnets, information about the exchange energy is directly related to the spin wave stiffness. In the case of a ferrimagnetic spinel with two magnetic A and B sublattices, the spin wave stiffness has been shown to be (Srivastava and Aiyar, 1987):

$$D = (2J_{AA}S_A^2 + 4J_{BB}S_B^2 - 11J_{AB}S_AS_B)a^2/|16(S_A - 2S_B)|, \tag{5.2}$$

where D is the spin wave stiffness, a is the lattice parameter, and J_{AA}, J_{BB} and J_{AB} are the exchange integrals between the S_A and S_B spins on the A and B sublattices, respectively. As a first approximation, J_{AA} and J_{BB} can be considered to be negligible compared to J_{AB} (Néel, 1948).

In a ferromagnetic system, a parabolic dispersion relation can be deduced from:

$$\hbar\omega = Dk^2, \tag{5.3}$$

where $\hbar$ is Planck's constant; ω and k are the frequency and wave vector of the magnon excitation. Several methods can be used to experimentally observe spin waves, e.g., inelastic neutron scattering, Brillouin scattering and spin wave resonance. Deriving information about the exchange energy is difficult without large single crystals to directly observe spin waves using inelastic neutron scattering. The lack of large single crystals of greigite means that these techniques cannot currently be applied to investigate the dynamic properties of spin waves in greigite. No useful information about the exchange energy of greigite exists in the literature.

D can be deduced from the Bloch spin wave expansion of the spontaneous magnetization, which gives the $T^{3/2}$ term directly in terms of D, where T is temperature.

This model is based on approximating the magnetic spin system as a system of harmonic oscillators. It has been shown that the spontaneous magnetization at low temperature is by approximation linear to the $T^{3/2}$ term using Bose-Einstein statistics. Keffer (1966) gives for a ferrimagnet:

$$M(T) = M_0\,[1 - \zeta(3/2)\,\Theta^{3/2} + L], \tag{5.4}$$

where $\zeta(3/2) = 2.612$ is the Riemann zeta function, $\Theta = (g_{eff}\,\mu_B/M_0)^{2/3}k_BT/(4\pi D)$, $g_{eff} = (g_A\,S_A - g_B\,S_B)/|S_A - S_B|$ is the effective spectroscopic splitting factor g in ferrimagnets, and g_A and g_B are the g factors for sublattices A and B, respectively. L represents the higher order terms. M is the spontaneous magnetization, M_0 is the spontaneous magnetization at the ground state at 0 K, k_B is Boltzmann's constant, and μ_B is the magnetic moment in Bohr magnetons. A value of 2.0 can be taken for g_{eff}. By carefully measuring M_s for a large aligned sample, the spin wave stiffness can be obtained from the $T^{3/2}$ term of M_s using the spin wave model.

We measured the low-temperature M_s for two synthetic greigite samples. The magnetization in a 5 T field at low temperature vs $T^{3/2}$ is plotted in Fig. 5.14. M_s decreases with increasing temperature as thermal excitation of magnons increases. By expanding the magnetization to the next term, we get:

$$M(T) = M_0\,[1 - A_{3/2}\,\Theta^{3/2} + A_{5/2}\,\Theta^{5/2} + L]. \tag{5.5}$$

Note that the coefficient of the $T^{5/2}$ term $A_{5/2}$ is positive, which could explain why M_s is concave upward with increasing temperature (Fig. 5.14). We apply the Bloch spin wave expansion and fit the low-temperature M_s data to a second degree polynomial of $T^{3/2}$ using Equation 5.5. The corresponding D values for the two samples obtained from the M_s measurements are 182 meV·Å^2 and 205 meV·Å^2 with R^2 values of 0.9988 and 0.9943, respectively. The high R^2 values indicate strong polynomial regression of the low-temperature magnetization with respect to $T^{3/2}$. By using Equation 5.2 and assuming values of $S_A = 2.5$, $S_B = 2.25$ and substituting $a = 9.854$ Å, and as a first approximation ignoring J_{AA} and J_{BB}, we obtain the corresponding J_{AB} values of 0.97 meV and 1.09 meV for the two samples. The resulting effective exchange constant is $A = D{\cdot}M_s/(2g_{eff}\,\mu_B) = \sim 0.2\times 10^{-11}$ J/m, which appears to be the first estimate of A for greigite.

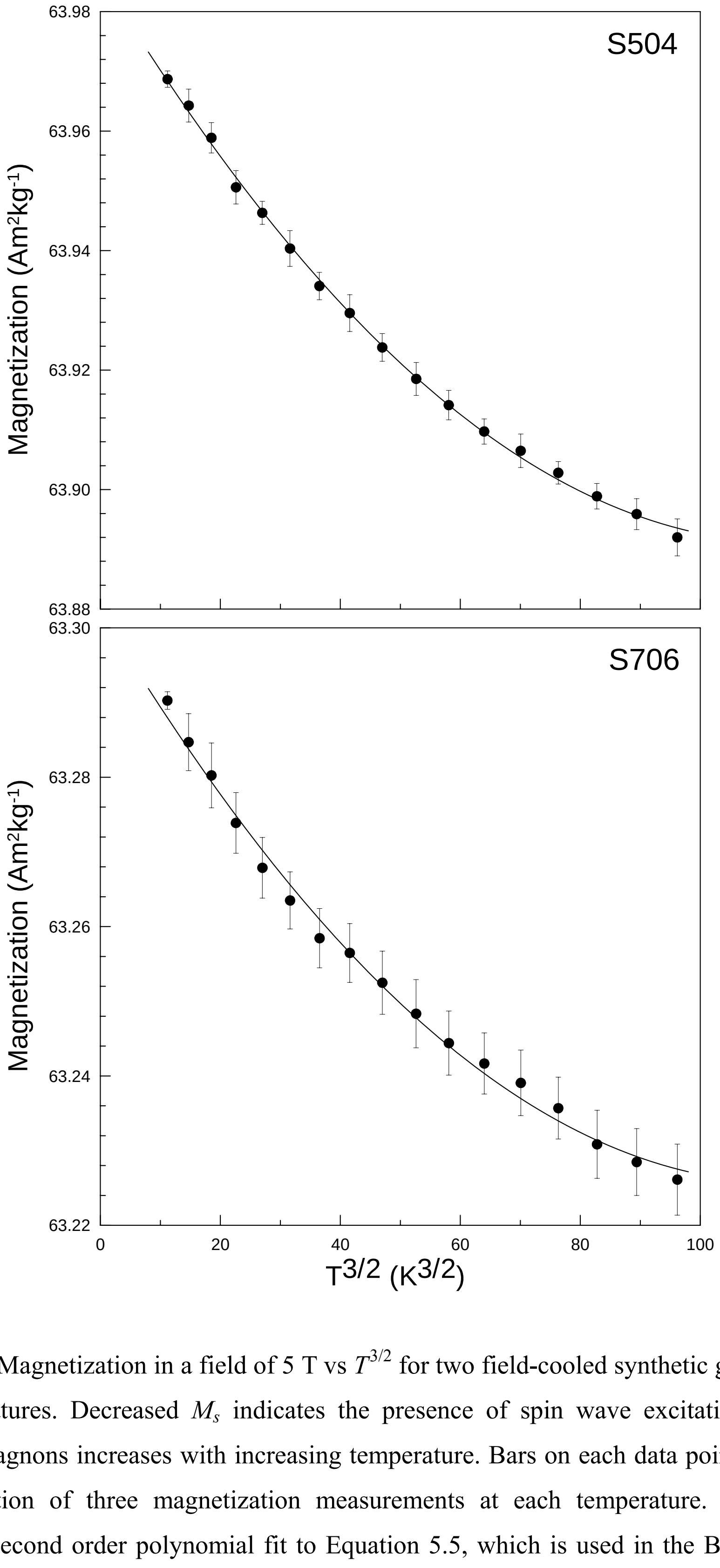

Figure 5.14. Magnetization in a field of 5 T vs $T^{3/2}$ for two field-cooled synthetic greigite samples at low temperatures. Decreased M_s indicates the presence of spin wave excitations as thermal excitation of magnons increases with increasing temperature. Bars on each data point represent the standard deviation of three magnetization measurements at each temperature. The solid line represents the second order polynomial fit to Equation 5.5, which is used in the Bloch spin wave expansion to obtain the spin wave stiffness for greigite.

5.4. Discussion

5.4.1. Fundamental magnetic parameters for greigite

5.4.1.1. Saturation magnetization

We have demonstrated that the M_s of greigite is much higher than has been estimated in many previous studies (Table 5.1). The apparently low value of M_s for greigite in previous reports is not a genuine property of greigite, but is rather a result of sample impurity in these previous studies. Any magnetic and electronic models that are based on lower values of M_s for greigite should therefore be regarded with caution. The M_s value of 59 $\mathrm{Am^2kg^{-1}}$ (3.13 μ_B/f.u.) reported here is more likely to be the precise value for greigite because of the high purity of the studied sample. Neutron diffraction results for this sample enable unambiguous determination of the magnetic structure of greigite and reveal the tetrahedral and octahedral iron moments in greigite (Chapter 6). These analyses also indicate a consistent M_s value to that obtained from the magnetic measurements reported here, which is slightly higher than the value of ~3.02 μ_B/f.u. obtained by spin-polarized multiple-scattering calculations (Braga et al., 1988).

Assuming that the magnetic structure of greigite is identical to that of magnetite and considering the different atomic weight of O and S, the M_s for greigite at room temperature would be ~70 $\mathrm{Am^2kg^{-1}}$ (~4 μ_B/f.u.), which is slightly higher than the value obtained in this study. Neutron diffraction also indicates that the net magnetic moment of the two sublattices in greigite is slightly lower than for magnetite (Chapter 6), which explains why M_s is slightly lower than for magnetite. Nevertheless, the value determined here is much closer to that of magnetite than any previously published estimates, which has important implications for the electronic and magnetic structure of greigite. Accurate determination of M_s is therefore important for understanding the magnetic properties of greigite, its magnetic structure, cation distribution and coordination. A precise value of this parameter is also crucial for micromagnetic and other modelling of greigite.

5.4.1.2. Mössbauer parameters

Previous Mössbauer spectra for greigite have been measured on poorly crystalline, non-stoichiometric fine-grained synthetic samples or impure natural samples. The hyperfine parameters obtained in this study are comparable to those reported in the literature (Table 5.2); however, they are probably more reliable because the sample studied here is purer than any other previously analyzed sample. Compared to magnetite, the B_{eff} is much lower for greigite, which is probably caused by a strong increased covalency effect in greigite. δ for the tetrahedral site is low (Table 5.2), which indicates that the tetrahedral iron is dominantly ferric (Coey et al., 1970; Vandenberghe et al., 1991). δ for the octahedral sites of 0.53 mm/s at room temperature (this study) suggests that the valence of these irons might be either high-spin ferrous or intermediate between ferrous and ferric (Spender et al., 1972). B_{eff} at both the tetrahedral and octahedral sites increases at low temperatures, with respective values of 31.9 and 32.7 T at 4 K, which is consistent with the study of Vandenberghe et al. (1991). However, they also observed a cross-over of $\mathrm{B_{eff}}$ values for tetrahedral and octahedral sites at ~290 K and obtained nearly equal B_{eff} values at room temperature. Our B_{eff} value for the octahedral sites is higher than for the tetrahedral sites below room temperature, which indicates that the effective spin for the octahedral sites is higher than for the tetrahedral sites. Unlike Coey et al. (1970) and Spender et al. (1972), who found almost the same values of B_{eff} for the two sites when extrapolating the two patterns to zero field, our study indicates a cross-over of values at ~0.5 T and a higher value for the octahedral sites at zero field.

5.4.1.3. Exchange constant

First estimates of the exchange constant J_{AB} (mean value of ~1.03 meV) and of the mean value of the spin wave stiffness (D = ~193 meV·Å^2) provided in this study give useful information for greigite. The exchange energy of magnetite has been extensively studied to verify the spin wave theory. However, variable measured values have been obtained for the exchange constant for magnetite with different approaches, e.g., inelastic neutron scattering (D = ~443 meV·Å^2; Brockhouse and Watanabe, 1963), low-temperature specific heat capacity measurements (D = ~60 meV·Å^2;Kouvel, 1956), (D = ~318 meV·Å^2; Kenan et al., 1963) and low-temperature M_s measurements (D = ~270 meV·Å^2; Aragón, 1992). The inconsistency is probably due to the complex nature of spin waves in ferrimagnetic spin arrangements (Srivastava and Aiyar, 1987). Direct observations of spin waves, e.g., determination of the dispersion relations for the acoustic and optic magnon modes by inelastic neutron scattering on single crystals, are needed for greigite to check the estimated value of the exchange constant obtained here and to check the reliability of this approach.

5.4.1.4. Curie temperature?

Greigite is chemically unstable at high temperatures, therefore high temperature magnetic measurements often reveal chemical decomposition rather than the T_C (Krs et al., 1992; Reynolds et al., 1994; Roberts, 1995; Dekkers et al., 2000). This makes it difficult to determine T_C for greigite, which remains unknown despite variable estimations reported in the literature. Spender et al. (1972) obtained an estimate for T_C of 333°C by extrapolating thermomagnetic curves to high temperatures, although it is likely that this estimate was affected by thermal alteration. Vandenberghe et al. (1991) made Mössbauer spectroscopic measurements up to 207°C and extrapolated B_{eff} of iron in tetrahedral sites to obtain a T_C value of at least 800 K (527°C) for greigite. No other corroborating data are available to indicate whether this is a reasonable inference. Roberts (1995) found a break in slope of the trend for all hysteresis parameters at 595 K (322°C). This break must mark the lower limit of the unblocking temperature range at which thermal energy begins to overcome the magnetocrystalline anisotropy for greigite. Evidence presented here (Fig. 5.13) indicates that T_C is likely to exceed 350°C in greigite. This is in disagreement with a T_C of ~320-330°C that is often incorrectly cited for greigite (e.g., Opdyke and Channell, 1996; Dunlop and Özdemir, 1997). The major break in slope at 250°C for the plotted hysteresis parameters (Fig. 5.12) for the studied greigite sample is lower than T_C estimates from the literature, which indicates that the synthetic samples studied here decomposed after heating at and above 250°C.

5.4.2. Magnetic properties

5.4.2.1. Dominant pseudo-single-domain and multi-domain behaviour

The grain size of the studied synthetic greigite sample is in the micron to tens of microns range (Fig. 5.3), which is large enough for PSD and MD behaviour to dominate the sample (Hoffmann, 1992; Chang et al., 2007). The coercivity of this synthetic sample is much lower than in most natural sedimentary greigite samples, which are often found in the SD state and therefore have much higher coercivities (Roberts, 1995; Roberts et al., 2006), although SP greigite is also common in many reducing environments (Rowan and Roberts, 2006). The low coercivity in the studied synthetic greigite samples might therefore be caused by either MD or SP behaviour; however, low-temperature hysteresis measurements do not indicate substantial magnetic blocking as expected for SP grains (Fig. 5.11). Detailed analysis of the magnetic behaviour of the studied synthetic greigite sample confirms that it is dominated by PSD/MD behaviour (Chang et al., 2007).

5.4.2.2. Presence of superparamagnetic behaviour

Although the studied greigite samples are dominated by large grains (Fig. 5.2, 5.3) with PSD/MD properties, restricted SP behaviour is also observed in magnetic and Mössbauer measurements. ZFC/FC susceptibility measurements for one studied greigite sample indicate a clear maximum in magnetization at ~160 K in the ZFC curve (Fig. 5.9). This is probably the mean blocking temperature of fine particles in the measured greigite sample. This interpretation is supported by Mössbauer data (Fig. 5.4). In the ordered magnetic hyperfine spectra, the six-line hyperfine spectrum would collapse with decreasing relaxation time caused by spin-wave time-averaging (Greenwood and Gibb, 1971). If the fluctuation rate is slow compared to the precession frequency of the nucleus in the field, the full six-line pattern is observed. If the fluctuation rate is extremely rapid, the nucleus will only respond to the time-averaged field which is zero and a symmetric quadrupole pattern will be seen. At room temperature, the central doublet (Fig. 5.4) is probably due to thermally relaxed fine particles, which is confirmed by low-temperature Mössbauer measurements. The central quadrupole doublet present at room temperature disappears at 4 K and 50 K (Fig. 5.4); fine particles are blocked and contribute to the observed sextets. Fine greigite particles therefore appear to be responsible for the SP properties that produced the quadrupole doublet in room temperature Mössbauer spectra. The origin of these fine particles is not clear. They may have been produced during synthesis, although they could also be small fragments that were produced by damaging the large, soft crystals during sample preparation.

5.4.2.3. Low-temperature coercivity minimum

A low-temperature coercivity minimum occurs in all of the studied greigite samples (Fig. 5.11). No such coercivity minimum has been reported before (e.g., Spender et al., 1972; Moskowitz et al., 1993; Roberts, 1995). However, previous studies were predominantly based on SD or SP greigite samples, while the observed local coercivity minimum occurs in PSD/MD greigite, and is probably related to the presence of magnetic domains (i.e., domain re-ordering). Nevertheless, we are currently unable to provide a detailed explanation for this local coercivity minimum.

5.4.3. Comparison of greigite with magnetite

It is useful to compare greigite and its oxide equivalent, magnetite (Fe_3O_4). These two minerals have a similar chemical composition and share the same inverse spinel crystal structure (Skinner et al., 1964). Magnetite should therefore be a reasonable analog for understanding the magnetism of greigite. The magnetic properties of magnetite have been well established for decades (Dunlop and Özdemir, 1997, and references therein), but the fundamental magnetic parameters for greigite are still poorly known. Despite expected similarities between the two phases, their magnetic properties are different in many aspects.

(1). Saturation magnetization. In the literature, the M_s of greigite is often suggested to be less than one-third that of magnetite (Table 5.1). We have demonstrated that the M_s for greigite at room temperature is about 59 Am^2kg^{-1}, which is lower than the value of ~90-92 Am^2kg^{-1} for magnetite even when considering the difference in atomic weight of O and S atoms (which converts to ~70 Am^2kg^{-1}). Neutron diffraction results verify that the M_s for greigite is slightly smaller than that of magnetite (Chapter 6).

(2). Low-temperature magnetic transition. Despite similarities in the chemical composition and crystal structure of these two spinels, no low-temperature magnetic discontinuities are observed for greigite, as indicated in this and in other studies (Coey et al., 1970; Spender et al., 1972; Vandenberghe et al., 1991; Moskowitz et al., 1993; Roberts, 1995; Dekkers et al., 2000).

(3). Easy axis of magnetization. In magnetite, the [111] crystallographic axis is the easy axis of magnetization at room temperature. However, the easy axis of magnetization for greigite has been shown to be the [100] crystallographic axis, as determined by Yamaguchi and Wada (1970) using electron diffraction. This observation has been confirmed by electron microscopic observations of bacterial greigite magnetosomes (e.g., Heywood et al., 1991; Bazylinski et al., 1993).

(4). Exchange energy. Our estimated exchange constant for greigite is lower than that of magnetite. This could be a result of the replacement of oxygen by sulphur in the spinel crystal lattice in greigite. This is likely to affect the superexchange coupling between iron in the octahedral and tetrahedral sites.

These properties and others demonstrate some intrinsic differences between the fundamental magnetic parameters of two spinels, magnetite and greigite. Some of these must reflect fundamental differences, e.g., in electronic structure, which demonstrate that considerable caution must be taken when making comparisons between these two inverse spinel minerals.

5.5. Conclusions

Pure synthetic greigite samples were produced with a new hydrothermal method. XRD, magnetic, Mössbauer spectroscopy and neutron diffraction measurements confirm sample purity. SEM observations demonstrate the crystallinity and morphology of individual greigite crystals, most of which are cubo-octahedral, with grain sizes up to 44 μm. These samples have the largest mean particle size of any synthetic or natural greigite sample described in the literature. Some crystals are elongated, with plate-like or prism-like crystals being the dominant morphologies.

The following magnetic properties have been determined for greigite from magnetic and Mössbauer spectroscopic measurements. The M_s at room temperature is ~59 Am^2kg^{-1} (3.13 μ_B/f.u.), which is much higher than previously published values because previous studies did not use high purity samples. The magnetic properties of the pure synthetic samples studied here are dominated by PSD/MD behaviour, although traces of SP behaviour are evident in ZFC/FC magnetization curves and in Mössbauer spectroscopic measurements. No low-temperature magnetic transition was detected, which confirms previous reports. However, a local coercivity minimum is clearly observed at around 130 K, which is probably related to the MD properties of the studied greigite samples. High-temperature magnetic analysis indicates that the synthetic samples start to undergo chemical decomposition at ~250°C. High-temperature magnetic measurements on an extremely stable natural greigite sample indicate that the T_C of greigite must exceed 350°C, although the exact value of T_C remains unknown. The exchange constant of greigite was estimated using low-temperature M_s measurements. The mean spin wave stiffness value for greigite is estimated to be ~193 meV·Å^2, with a corresponding exchange constant of ~1.03 meV, which was obtained from the $T^{3/2}$ term of M_s based on the Bloch spin wave expansion. Further work is needed to check our estimated value of the exchange constant for greigite. Mössbauer spectroscopy indicates two magnetic sextets for octahedral and tetrahedral sites in greigite, which confirms previously reported hyperfine parameters for greigite (Table 5.2). These parameters increase with decreasing temperature and B_{eff} is higher for the octahedral sites than for the tetrahedral sites below room temperature.

Production of pure greigite samples and new data presented here provide important new fundamental magnetic parameters for greigite. These determinations will benefit efforts to model magnetizations in a wide range of palaeomagnetic and environmental magnetic studies of greigite-bearing sediments and also in studies of greigite magnetosomes in microorganisms.

Chapter 6

Magnetic structure of greigite probed by neutron powder diffraction and polarized neutron diffraction

This chapter has been accepted for publication in the *Journal of Geophysical Research – Solid Earth* for publication, Chang, L., B. D. Rainford, J. R. Stewart, C. Ritter, A. P. Roberts, Y. Tang, and Q. Chen, Magnetic structure of greigite (Fe_3S_4) probed by neutron powder diffraction and polarized neutron diffraction.

Abstract We have investigated greigite using a combination of neutron powder diffraction and polarized neutron diffraction to give the first unambiguous assignment of its magnetic structure. Our results confirm that greigite has a collinear ferrimagnetic structure with antiferromagnetic coupling between the tetrahedral (*A*) and octahedral (*B*) sites. Our analysis also indicates that greigite does not have a significant vacancy concentration or spin canting. High-resolution neutron powder diffraction results enable determination of sublattice magnetizations of the *A* and *B* sites. At room temperature, the average magnetic moments on the two sites are almost the same (~3.0 μ_B), with a net magnetic moment of ~3.0 μ_B per formula unit (f.u.). The magnetic moment of the *B* sites decreases slightly between 10 K and room temperature, while the *A*-site moment is relatively stable as a function of temperature; this indicates that greigite is probably an R-type ferrimagnet. At 10 K, the average magnetic moments of the *A* and *B* sites are 3.0 μ_B and 3.25 μ_B, respectively. Neutron diffraction measurements, coupled with magnetic measurements, on our pure synthetic greigite samples indicate that the saturation magnetization of greigite is lower than that of magnetite. It is proposed that the lower magnetic moment in greigite (saturation magnetization = ~59 Am^2kg^{-1}) compared to magnetite is probably caused by an increased degree of covalency between iron and sulphur compared to oxygen ligands, or by greater delocalization of the 3*d* electrons in greigite.

.

6.1. Introduction

Greigite is an iron thiospinel, which has the same crystal structure as magnetite (Skinner et al., 1964). Greigite crystallizes in the inverse spinel structure (space group $Fd\bar{3}m$, Z = 8). As a basic phase in the thiospinel family, its unique magnetic and electronic properties have attracted considerable interest in solid state physics and chemistry (e.g., Coey et al., 1970; Yamaguchi and Wada, 1970; Spender et al., 1972; Goodenough and Fatseas, 1982; Braga et al., 1988; Letard et al., 2005). More importantly, greigite has been increasingly recognized to be geologically and geophysically important since its formal identification in lacustrine sediments (Skinner et al., 1964) and in anaerobic magnetotactic bacteria (e.g., Farina et al., 1990; Mann et al., 1990). It is now recognized that greigite is widely distributed in marine and lake sediments, in which anoxic, sulphate-reducing diagenetic conditions have occurred (e.g., Roberts and Weaver, 2005, and references therein). Its presence within sediments can therefore significantly affect palaeomagnetic and environmental magnetic records.

Despite its importance and widespread occurrence in natural environments, many magnetic properties of greigite remain unknown because of its metastability (e.g., Berner, 1984; Rickard and Luther, 2007). This sulphide phase is prone to oxidize in air, decompose at elevated temperatures, and react to form other iron sulphides. The greigite produced in many syntheses is affected by impurities, lattice defects and small grain size, which leads to superparamagnetic (SP) effects. Difficulty in obtaining pure greigite samples has also hindered determination of many important magnetic properties of greigite. An ongoing problem has been that the magnetic structure of greigite is still not clear, although its crystal structure has been well established (e.g., Skinner et al., 1964). It has been presumed that greigite has the same magnetic structure as magnetite because of their similar crystallographic structure. However, previous studies indicate that the saturation magnetization (M_s) of greigite appears to be much smaller than that of magnetite (e.g., Uda, 1965; Coey et al., 1970; Spender et al., 1972; Hoffmann, 1992; Reynolds et al., 1994; Dekkers and Schoonen, 1996; Chen et al., 2005; He et al., 2006). Various models have been proposed to account for the electronic and magnetic structures of greigite (e.g., Coey et al., 1970; Spender et al., 1972; Goodenough and Fatseas, 1982; Braga et al., 1988; Sherman, 1990; Letard et al., 2005). Based on Mössbauer spectroscopy measurements, Coey et al. (1970) proposed that greigite had the same ferrimagnetic structure as magnetite, but the expected net magnetic moment of $\geq 4\ \mu_B$ (considering the spin-only values for ionic moments in the Néel model) was inconsistent with their low measured magnetic moment ($2.2 \pm 0.2\ \mu_B$/f.u., extrapolated to 0 K). Magnetic measurements on the purest known synthetic greigite samples give the most accurate available M_s estimate of ~59 Am^2kg^{-1} (3.1 μ_B/f.u.) (Chapter 5). While the low M_s values reported in most published studies of greigite are largely caused by sample impurity, this recently reported M_s value is still inconsistent with the assumed high-spin ionic model for greigite (Chang et al., 2008). It has also been speculated that the (Fe^{2+}, Fe^{3+}) distribution in greigite is different from magnetite, that the magnetic state of these ions is different, or that the magnetic structure is not the collinear ferrimagnetic structure found in magnetite.

Production of pure, single-phase synthetic greigite samples makes it possible to establish some of its fundamental magnetic properties. In order to resolve the ambiguities associated with its magnetic structure, we have carried out a magnetic structure determination study using a combination of neutron powder diffraction (NPD) and polarized neutron diffraction on a highly pure synthetic greigite sample. Our analysis reveals the magnetic structure of greigite, along with the sublattice magnetizations and their temperature dependence, for the first time.

6.2. Samples and experiments

The synthetic greigite samples analyzed in this study were prepared by reacting ferric chloride ($FeCl_3 \cdot 6H_2O$) with thiourea (CH_4N_2S) and formic acid (HCOOH) at 170°C according to a new hydrothermal method (Tang et al., 2007; Chang et al., 2008). The samples have been confirmed to be pure, single-phase greigite that occurs as large polycrystalline grains (Chapter 5). Each synthesis yielded only less than 50 mg of pure greigite. Several tens of greigite syntheses were therefore carried out to provide enough material for this study. X-ray diffraction (XRD) analysis was carried out immediately after each synthesis to monitor sample purity. XRD spectra were recorded using a Phillips X'pert X-ray diffractometer with high-intensity Cu-Kα radiation (λ = 1.54056 Å) at a scanning speed of 0.05 °/s over a 2θ range from 10 to 80°. Samples with mixed phases were rejected and were not used for further analysis. The main impurities are cubic pyrite (FeS_2), orthorhombic marcasite (FeS_2) and elemental sulphur (S). The resulting pure synthetic greigite samples (~20 batches with a total weight of ~1 g) were kept in a desiccator to prevent wet oxidation before the neutron scattering experiments, which were conducted about half a year after synthesis. To enable cross-comparison of data for our pure synthetic greigite, NPD analyses were also made for the three purest natural greigite samples in our sample collection. These include iron sulphide nodules from the Valle Ricca section, near Rome, Italy (van Dongen et al., 2007) and from southwestern Taiwan (Jiang et al., 2001), and a coarse-grained greigite sample from the Czech Republic (Chang et al., 2007).

Neutron powder diffraction experiments were carried out at the Institut Laue-Langevin, Grenoble, France. The diffraction patterns were collected using both the high-intensity neutron powder diffractometer D1B and the high-resolution neutron powder diffractometer D1A at ILL using neutron wavelengths of 2.51 Å and 1.91 Å, respectively. The sample was held in a vanadium can for the NPD experiments. Full diffraction patterns were measured on D1A at 10 K, 100 K, 200 K and 290 K, with typical acquisition times of about 4 hours per temperature. On D1B, with its banana multidetector, it took only ~10 minutes to acquire a single diffraction pattern.

Successive measurements were made as the temperature was slowly ramped between room temperature and 10 K. Polarized neutron diffraction experiments were performed using the neutron polarization analysis spectrometer D7 at ILL. The incident neutron beam, with wavelength of 3.1 Å, was polarized by a supermirror polarizer before being scattered by the sample. A vertical field of 5 T was applied to saturate the magnetization of the sample normal to the scattering plane. The magnetic anisotropy of greigite is low (the coercivity of the studied multi-domain greigite sample is normally less than 10 mT at room temperature (Chang et al., 2007, 2008)); therefore, the magnetic moment can be readily oriented along the applied field. While D7 is designed for full polarization analysis, this technique is not applicable to a ferro- or ferrimagnet. Instead we only measured the non-spin-flip scattering intensities $I\,(+\,,+)$ and $I\,(-\,,-)$, which correspond to the scattering intensities with the neutron spin parallel (flipper off) and antiparallel (flipper on) to the sample magnetization (Moon et al., 1969). A neutron spin flipper was used to change the polarity of the neutron beam. The spin-flip scattering intensities ($I\,(+\,,-)$ and $I\,(+\,,-)$) were not measured. To avoid analysis of the polarization of the scattered beam, a thin (0.1 mm) shim of unmagnetized iron was placed between the sample and the detector banks. This had the effect of depolarizing the scattered beam before it reached the polarizing analysers in front of the D7 detectors. The sample was held in an aluminium sample can inside an ILL orange cryostat, allowing measurements between 2 K and room temperature. The incident neutron wavelength of 3.1 Å permitted the first 10 Bragg peaks to be measured.

6.3. Results

6.3.1. Neutron powder diffraction

NPD is the primary technique for probing the magnetic structures of magnetic materials (e.g., Rodríguez-Carvajal, 1993). The X-ray and neutron diffraction patterns for the synthetic greigite sample confirm the sample purity (Fig. 6.1): all the peaks may be indexed in the $Fd\bar{3}m$ space group and there is no sign of significant impurity peaks. The purity of the analysed synthetic sample is especially clear when plotted alongside data for the purest available natural samples (Fig. 6.1), which commonly contain pyrite and silicate grains in addition to greigite. The difference in relative intensities of the peaks between the X-ray and neutron data is partly due to the difference in atomic scattering amplitudes for X-rays and neutrons, but there is also a large magnetic contribution in the neutron patterns. This is particularly evident in the (111), (222), (331) and (531) peaks. The data from D1B (Fig. 6.1) are characteristic of a medium-resolution diffractometer, with the multidetector coverage extending over the first ten Bragg peaks. D1A is a high-resolution instrument, as can be seen from the narrow peak widths in Fig. 6.2. Its shorter wavelength also allows a larger range of *d*-spacings to be studied (27 peaks up to the maximum 2*θ*).

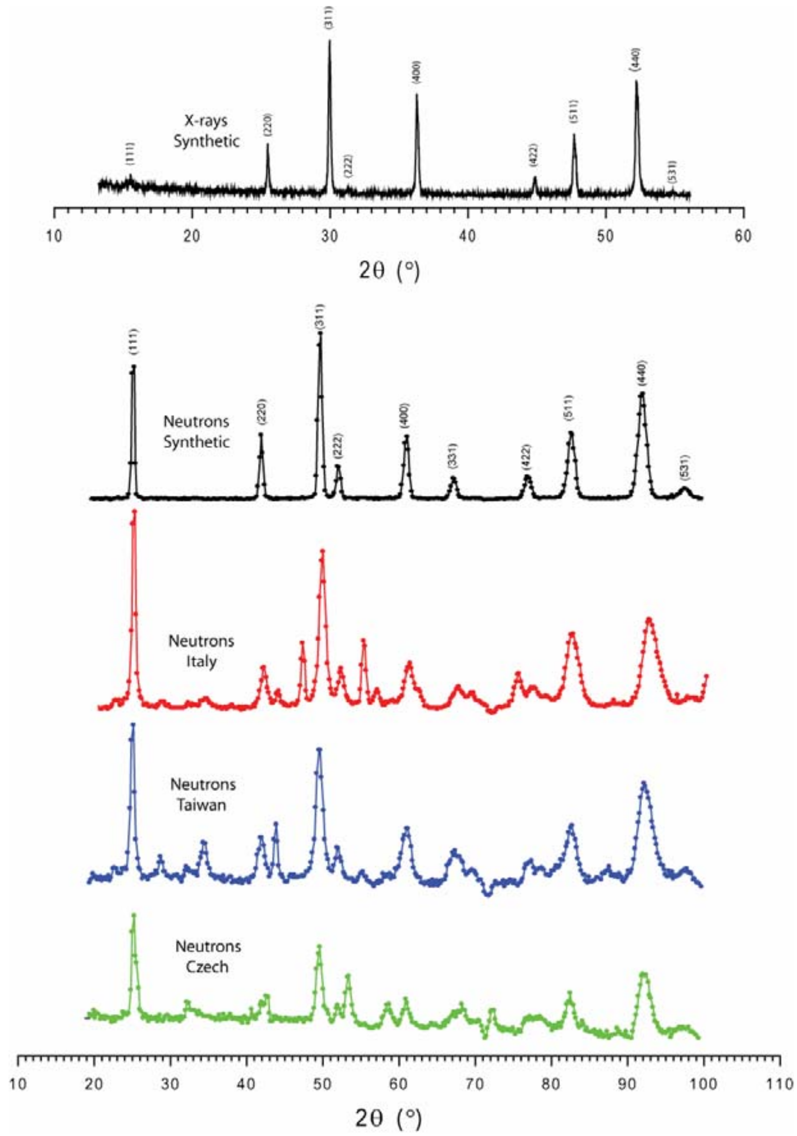

Figure 6.1. A room temperature X-ray diffraction pattern (λ = 1.54 Å) for the synthetic greigite sample is shown (above) for comparison with a room-temperature neutron diffraction spectrum (below) recorded on the high-intensity neutron powder diffractometer D1B (λ = 2.51 Å). A pronounced magnetic scattering contribution is observed in the neutron diffraction pattern, e.g., the (111), (222), and (331) reflections. NPD patterns are also shown for three natural greigite samples. The differences between these NPD patterns are attributed to impurities in the natural samples.

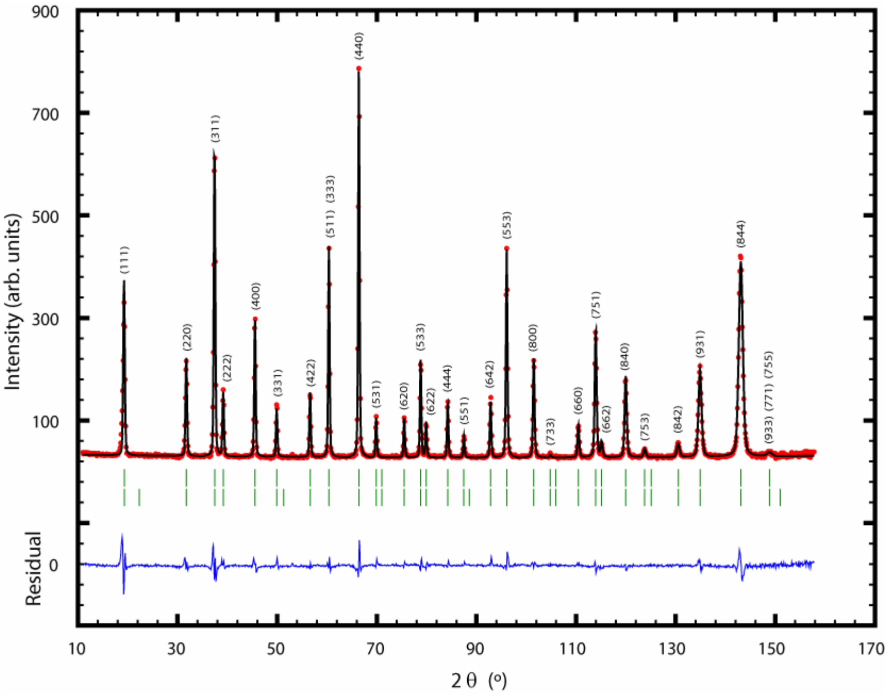

Figure 6.2. Rietveld refinement of the high-resolution NPD pattern for the synthetic greigite sample recorded on the D1A neutron powder diffractometer (λ = 1.91 Å) at 200 K. The observed and calculated intensities are shown by red dots and by a black solid line, respectively. The blue line at the bottom of the figure is the calculated residual between experimentally measured values and the refinement. Green tick marks indicate the positions of the nuclear (top lines) and magnetic (bottom lines) Bragg reflections. The model enables refinement of both the positional parameter and the magnetic moments of the two sublattices.

For unpolarized neutrons diffracted from a ferromagnetic or ferrimagnetic sample, there is no coherence between the nuclear and magnetic diffraction. The total scattering intensity is therefore the sum of the nuclear and magnetic diffraction intensities. To analyse the diffraction patterns, we used a two-phase profile refinement method: one phase involves the nuclear scattering contribution, while the second involves the magnetic scattering contribution. Rietveld analysis was carried out using the FULLPROF suite (Rodríguez-Carvajal, 1993) (Fig. 6.2) to refine a minimal set of variables, i.e., the lattice parameter, the internal sulphur coordinate *u* and the magnetic moments of the tetrahedral and octahedral sites, as well as absorption, background, and profile coefficients (Table 6.1). The inverse spinel structure (space group $Fd\bar{3}m$) refined from our NPD data agrees well with that determined by XRD (e.g., Skinner et al., 1964; Spender et al., 1972). In this crystal structure, it is supposed that Fe^{3+} occupies the tetrahedral sites at (⅛,⅛,⅛) and both $Fe^{2+}$and Fe^{3+} occupy the octahedral sites at (½,½,½) with sulphur atoms at (*u*, *u*, *u*) positions (Fig. 6.3). The values of *u* from the refinements are found to be independent of temperature: the D1B data yield the value $u = 0.2550(2)$, while the D1A data give $u = 0.2542(2)$. The lattice parameter a_0 smoothly increases with temperature, following the expected thermal expansion. This is a feature of the enharmonic terms in the inter-atomic potentials; a_0 values for particular temperatures are listed in Table 6.1. The small systematic difference between the a_0 values refined from the D1A and D1B data is probably due to small uncertainties in the wavelength calibrations.

Table 6.1. Structural parameters for greigite from FULLPROF Rietveld refinements.

Instrument	Temperature (K)	10	100	200	290
D1B	M_A (μ_B)	3.16±0.07	3.20±0.07	3.19±0.07	3.20±0.07
D1B	M_B (μ_B)	-3.24±0.05	-3.19±0.05	-3.16±0.05	-3.08±0.05
D1B	M / *f.u.* (μ_B)	3.32±0.09	3.18±0.09	3.13±0.09	2.96±0.09
D1B	a_0 (Å)	9.8559(3)	9.8585(3)	9.8650(3)	9.8734(3)
D1B	u	0.2552(7)	0.2549(8)	0.2552(8)	0.2552(8)
D1A	M_A (μ_B)	3.00±0.08	2.99±0.08	3.01±0.08	2.97±0.08
D1A	M_B (μ_B)	-3.26±0.06	-3.17±0.06	-3.07±0.06	-3.00±0.06
D1A	M / *f.u.* (μ_B)	3.52±0.10	3.35±0.10	3.13±0.10	3.03±0.10
D1A	a_0 (Å)	9.8538(2)	9.8552(2)	9.8645(2)	9.8718(2)
D1A	u	0.2542(7)	0.2541(6)	0.2546(4)	0.2540(6)

M_A and M_B are the magnetic moments of the *A* and *B* sites, respectively, M / *f.u.* is the total magnetic moment per unit formula, a_0 is the lattice parameter, and *u* is the internal sulphur coordinate.

The magnetic refinement confirms a collinear ferrimagnetic structure (magnetic space group F-1) (Fig. 6.3), in which the iron moments on the tetrahedral and octahedral sites are antiparallel. The values of the magnetic moments M_A and M_B of the two Fe sites are tabulated in Table 6.1 for specific temperatures, along with the net magnetic moment per formula unit $|2\,M_B + M_A|$. The temperature dependence of the magnitude of the moments is shown in Fig. 6.4 (where the scale for the net magnetic moment has been shifted for clarity (right-hand axis)). Agreement between the D1A and D1B refinements is generally excellent, although there is a systematic difference of about 0.2 μ_B between the values for the tetrahedral site moments, i.e., at room temperature the D1B data give $M_A = 3.20(7)$ μ_B, while for the D1A data $M_A = 2.97(8)$ μ_B.

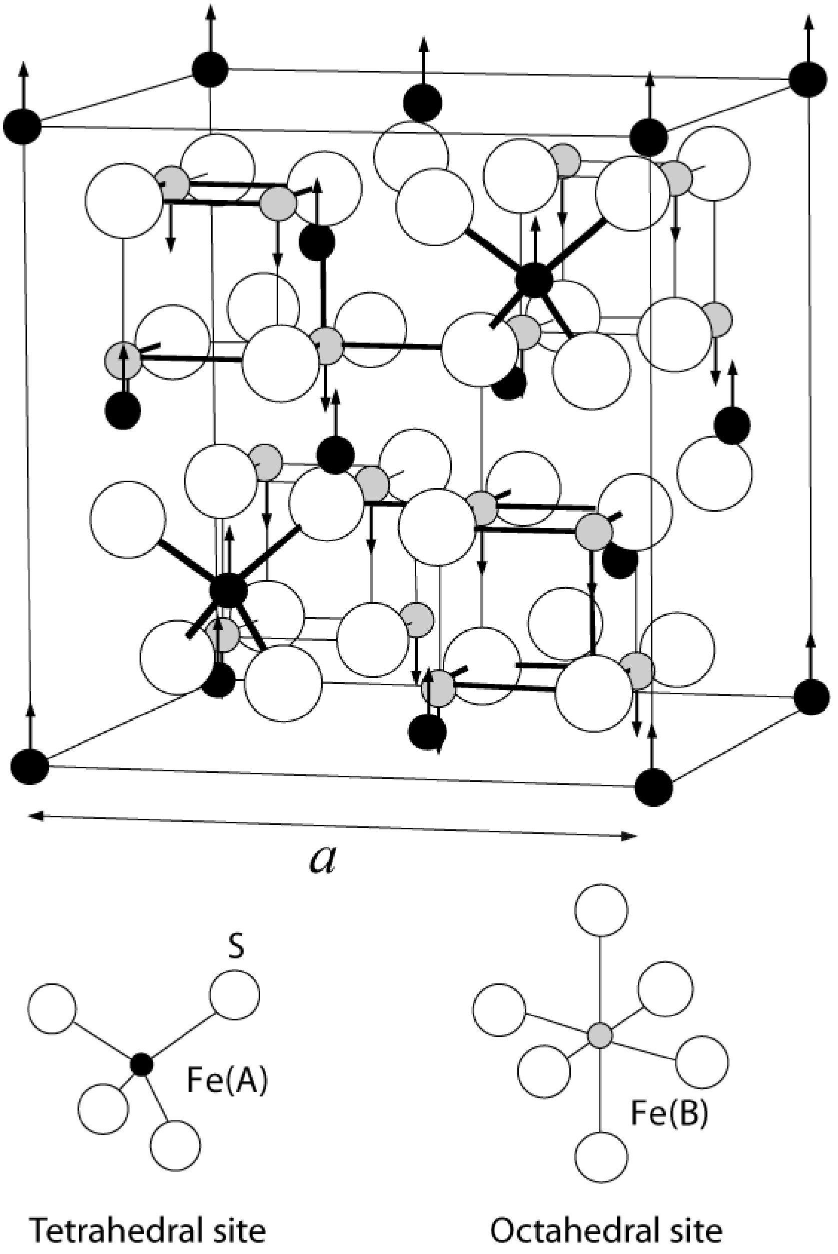

Figure 6.3. The crystallographic and magnetic structure of Fe_3S_4 determined from NPD and polarized neutron diffraction (adapted from García and Subías (2004)). Greigite crystallizes in the inverse spinel structure with a cubic close-packed sulphur array (space group $Fd\bar{3}m$, Z=8). Fe^{3+} occupies the *A* (tetrahedral) sites, while both $Fe^{2+}$and Fe^{3+} occupy the *B* (octahedral) sites. A collinear ferrimagnetic spin arrangement was found in greigite with antiferromagnetic coupling between the octahedral and tetrahedral Fe ions. *a* is the lattice parameter. The arrows represent the magnetic moment directions of each Fe ion. Magnetic moments are shown to be aligned along the crystallographic *c* axis because the easy axis of magnetization is the [100] crystallographic axis (Yamaguchi and Wada, 1970). The absolute moment directions within the unit cell cannot be obtained because, for the cubic phase, only relative orientations of moments affect the NPD intensities.

The origin of this discrepancy is not clear, but it may be related to correlations with thermal parameters in the fits. That is, thermal vibrations change the scattering amplitude by the Debye-Waller factor, which drops off with increasing 2θ, as does the magnetic scattering amplitude magnetic form factor, so it is possible that there would be correlations between the magnetic moments M and the thermal parameters. Nevertheless, the agreement between the two data sets for the octahedral site moments is excellent. There are several qualitative features common to both data sets. First, the magnitude of the moments at both Fe sites is similar (~3.0 μ_B at room temperature); these values are much smaller than those found in magnetite (e.g., Klotz et al., 2006). Second, the magnetic moment per formula unit is 3.0 μ_B at room temperature, rising to ~3.4 μ_B at 10 K; these values are in good agreement with bulk magnetic measurements which give M_s ~59 Am^2kg^{-1} (3.12 μ_B/f.u.) at room temperature and M_s ~64 Am^2kg^{-1} (3.39 μ_B/f.u.) at 10 K (Chapter 5). Third, while the B site moment increases as temperature decreases, reaching 3.25 μ_B at 10 K, the A site moment is practically independent of temperature. The temperature dependence of the sublattice magnetizations for greigite resembles those of R-type ferrimagnets, as found in many ferrites, e.g., $NiFe_2O_4$. By contrast, magnetite is a Q-type ferrimagnet, in which both sublattice magnetizations behave like true ferromagnets. Greigite has a much weaker A-B exchange interaction than magnetite (Chapter 5), which might explain the different sublattice magnetization curves for greigite and magnetite.

There were no significant differences in the qualities of the refinements of the D1A patterns at 10, 100, 200 and 290 K or in the D1B temperature scan from 290 K to 10 K. This is consistent with previous studies of greigite in which no evidence has been found for an equivalent of the Verwey transition in magnetite or for any other magnetic transition (Spender et al., 1972; Moskowitz et al., 1993; Roberts, 1995; Chang et al., 2007, 2008).

In the spinel structure, the sulphur coordinate u is related to the Fe-S bond lengths d_A and d_B at the A and B sites by $d_A = \sqrt{3}\, a(u - 1/8)$ and $d_B = a(1/2 - u)$. From the fit parameters, we find d_A = 2.21(1) Å and d_B = 2.42(1) Å. These values are somewhat larger than those for the Fe-O bond lengths in magnetite (d_A = 1.90 Å and d_B = 2.05 Å; (Klotz et al., 2006)), as would be expected for a larger ligand ionic radius. The ratio d_B/d_A is 1.078 for magnetite, but 1.093 for greigite: this may indicate a greater mixed-valent character for the octahedral sites of greigite compared to magnetite.

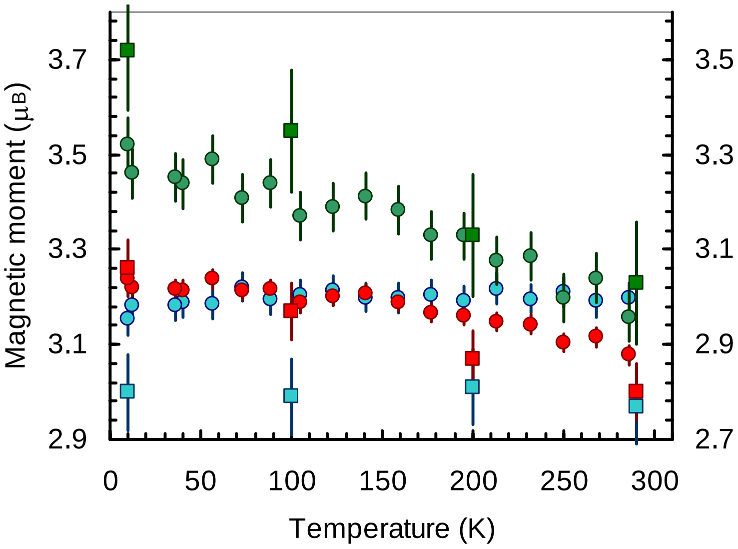

Figure 6.4. Temperature dependence of the sublattice (M_A and M_B) and total spontaneous (M_s) magnetizations for greigite. The blue and red circles are the sublattice moments of the tetrahedral sites M_A and octahedral sites M_B, respectively, derived from analysis of the D1B data. The blue and red squares are M_A and M_B values refined from the D1A data. The green circles and squares correspond to the moment per formula unit M/f.u. = (2 M_B - M_A) derived from the D1B and D1A data, respectively. For clarity, the scale of the M/f.u. data has been shifted as shown on the right-hand axis. The D1B data are averaged over five temperature points to reduce scatter. The average magnetic moment of the Fe ions on the B-sites decreases with increasing temperature, while the A-site moments appear to be temperature-independent below room temperature, which indicates that greigite is probably an R-type ferrimagnet.

6.3.2. Polarized neutron diffractometry

Polarized neutron diffraction was carried out to confirm the magnetic structure of greigite. Greigite is unstable at high temperature and decomposes before reaching its Curie temperature T_C (e.g., Krs et al., 1992; Roberts, 1995; Dekkers et al., 2000; Chang et al., 2008). It is therefore not possible to measure neutron diffraction patterns above and below T_C in order to separate the magnetic component of the Bragg peaks. Instead, we used polarized neutrons with a vertical applied field to saturate the magnetization of the sample normal to the scattering plane. This enabled isothermal separation of the nuclear and magnetic scattering. For a collinear ferro- or ferrimagnet, the flipping ratios for the saturated state give a measure of the ratio of the magnetic to nuclear structure factors. The non-spin-flip scattering intensities can be described by the interference of the nuclear and magnetic scattering (Brown and Forsyth, 1964):

$$I(\pm, \pm) = C\,|F_N \pm F_{mag}|^2, \tag{6.1}$$

where F_N and F_{mag} are the nuclear and magnetic structure factors and C is a constant. The ideal flipping ratio R is defined as the ratio between the diffraction intensities of neutrons with spin-up and spin-down (Brown and Forsyth, 1964):

$$R = \frac{I(+,+)}{I(-,-)} = \frac{(F_N + F_M)^2}{(F_N - F_M)^2} = \frac{(1+\gamma)^2}{(1-\gamma)^2}, \tag{6.2}$$

where $\gamma = F_N/F_M$ is the ratio of nuclear to magnetic structure factors. The flipping ratio R is determined by measuring the diffracted intensities with the neutron spin flipper turned alternately on and off. In practice, the measured flipping ratio differs from the ideal value because: (i) the incident beam is not 100% polarized, (ii) the neutron spin flipper is not 100% efficient, and (iii) the sample may introduce a degree of beam depolarization. When these factors are taken into account, the corrected flipping ratio becomes (Brown and Forsyth, 1964):

$$R = \frac{1+\gamma^2 + 2PD\gamma}{1+\gamma^2 - 2\eta PD\gamma}, \tag{6.3}$$

where P is the initial beam polarization, η is the flipping efficiency and D is the depolarization correction factor.

Diffraction profiles of the non-spin-flip intensities (I (+ , +) and I (– , –)) at room temperature in a 5 T magnetic field are shown in Figure 6.5a. In addition to greigite reflections, two strong Bragg peaks (at ~83° and 100° 2θ) can be attributed to the (111) and (200) Bragg peaks from the aluminium sample can (Fig. 6.5a). Aluminium is not magnetic, so the spin-up and spin-down neutron scattering have the same intensities. For greigite, the Bragg peak intensities for spin-up are mostly greater than those for spin-down (i.e., the flipping ratio R is greater than one) (Fig. 6.5a). There are two exceptions: for both the (220) and (422) reflections, the spin-down intensity is greater than the spin-up intensity (flipping ratio less than one). This may be seen more clearly in Fig. 6.5b, where the difference between the spin-up and spin-down patterns is plotted: here, the (220) and (422) reflections appear as negative peaks. The difference pattern is proportional to $4F_NF_M$, the product of the nuclear and magnetic structure factors. For the (220) reflection, the nuclear structure factor is $F_N = -8b_{Fe}$ (with a negligibly small sulphur contribution) while the magnetic structure factor is $F_M = -8p_A$. Here, b_{Fe} is the nuclear scattering amplitude of iron, while p_A is the magnetic scattering amplitude for the tetrahedral Fe site:

$$p_A = 2.69 \times 10^{-15}\, \mu_A\, f(Q), \tag{6.4}$$

where μ_A is the Fe moment on the tetrahedral sites and $f(Q)$ is the iron 3d form factor. The negative value of the product $F_N F_M$ for the (220) reflection means, therefore, that μ_A is antiparallel to the net magnetization. For the (422) reflection, the structure factors are $F_N = 8b_{Fe}$ and $F_M = 8p_A$, so the same argument applies as for the (220) reflection. This gives direct support to the collinear ferrimagnetic model of greigite in which the tetrahedral and octahedral Fe ions are antiferromagnetically coupled. For this model, it is readily shown that the nuclear and magnetic structure factors have the same sign as for all the other peaks, so that we expect flipping ratios greater than unity, as observed.

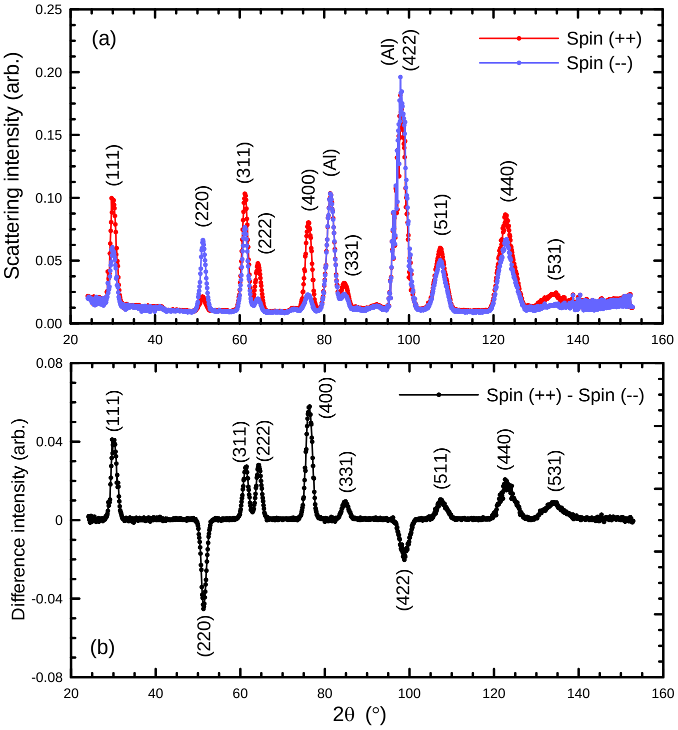

Figure 6.5. Spin-polarized neutron diffraction patterns for the synthetic greigite sample at room temperature in a magnetic field of 5 T. (a) Neutron spin-up (red line) and spin-down (blue line) diffraction patterns. Note the overlap of the greigite (422) reflection with the strong aluminium (200) peak. (b) Difference between the patterns shown in (a) (spin-up minus spin-down patterns).

To enable quantitative comparison of the D7 data with the magnetic structure of greigite, we compare in Table 6.2 the flipping ratios (R_{exp}; column 2) for the ten Bragg peaks measured at 20 K with the flipping ratios (R_{calc}; column 4) calculated from the magnetic and nuclear structure factors using the 10 K D1A data (i.e., sublattice moments and structural parameters). The R_{calc} data correspond to the ideal flipping ratio values, as defined in equation (2). Large discrepancies between R_{exp} and R_{calc} are evident for the reflections with γ values ($\gamma = F_N / F_M$) close to unity. Corrections for neutron polarization P, depolarization D, and flipping efficiency η are especially important. Values for P and η expected from the supermirror polarizers and spin flipper on D7 are normally about 0.9. For a bulk single crystal, the depolarization factor D is usually close to unity, but the values depend on the sample geometry and degree of magnetic saturation (Brown and Forsyth, 1964). However, the present sample is a fine powder and the degree of beam depolarization will be expected to be relatively high, because of the large contrast in B field within and between individual grains. The best fit between R_{exp} and R_{calc} is obtained with $P \cdot D = 0.7$ and $\eta = 0.9$. With these values, the corrected flipping ratio (column 5 in Table 6.2) agrees well with measured values (R_{exp}; column 2) within the error bars in all cases, except for the (422) reflection, which is contaminated by the strong aluminium (200) Bragg peak. We conclude that the D7 polarized neutron data confirm the magnetic structure of greigite derived from Rietveld analysis of unpolarized neutron diffraction data. One would normally expect polarized neutron diffractometry to give higher quality information than unpolarized data. This is the case for bulk single crystals; however, for powder samples the depolarization corrections can be large and it is difficult to determine these independently.

Table 6.2. Flipping ratios for polarized neutron diffraction for greigite at 20 K.

(*hkl*)	$R_{exp} = \Gamma^{++}/\Gamma^{-}$	ΔR_{exp}	R_{calc}	Corrected R_{calc}
(111)	1.90	0.11	2.643	1.87
(220)	0.20	0.03	0.027	0.21
(311)	1.45	0.05	1.766	1.45
(222)	3.36	0.34	13.20	3.50
(400)	4.52	0.23	190.0	4.50
(331)	1.61	0.11	2.366	1.66
(422)*	0.85	0.02	0.097	0.28
(511) & (333)	1.22	0.04	1.471	1.29
(440)	1.37	0.05	1.583	1.35
(531)	2.81	0.44	7.276	3.00

The experimental flipping ratio R_{exp} compared to R_{calc} calculated from the structure factors from the fit to the 10 K D1A data. The right-hand column has R_{calc} values corrected by the factor $PD = 0.7$ and a flipping efficiency $\eta = 0.9$. These values agree well with R_{exp} except in the case of the (422) reflection (*) which overlaps with the strong (200) peak for aluminium.

6.4. Discussion

6.4.1. Magnetic structure of greigite

NPD and polarized neutron diffraction experiments have enabled unambiguous assignment of the magnetic structure of greigite for the first time, confirming a collinear ferrimagnetic structure in which the iron moments on the tetrahedral sites are antiparallel to those on the octahedral sites. There is no evidence for significant spin canting in greigite from analysis of our neutron diffraction pattern because there are no extra peaks in the neutron diffraction pattern. This is also supported by the fact that there is no difference between the zero field neutron diffraction pattern and that measured in a 5 T field. In-field Mössbauer measurements also support the absence of significant spin canting in greigite (Chapter 5). Letard et al. (2005) proposed greigite to be a lacunary iron sulphide based on the differences between the observed XMCD spectra of greigite and magnetite. Rickard and Luther (2007) also argued that the composition of greigite is still not well-constrained and that greigite probably displays some degree of nonstoichiometry. Mössbauer measurements give possible evidence for nonstoichiometry of greigite (Coey et al., 1970; Spender et al., 1972). However, Qian et al. (1999) determined by spectrophotometric analysis that the composition of greigite in synthetic samples was $Fe_{2.994}S_4$, which is nearly stoichiometric. Our Rietveld profile analysis of the neutron diffraction data included parameters for partial occupancy of the Fe sites. However, no departure from stoichiometry was found in the parameters for the fitted profiles. The quality of the fits indicates that our synthetic sample does not have a significant vacancy concentration. In the standard inverse spinel structure, Fe^{3+} occupies the tetrahedral sites, while both Fe^{2+} and Fe^{3+} occupy the octahedral sites. Considering the ionic model, the formula of greigite can then be written as $[\uparrow Fe^{3+}]^{A}$ $[\downarrow Fe^{2+}\ \downarrow Fe^{3+}]^{B}$ S_4^{2-}. In the Néel (1948) model for magnetite, the ions have their localized spin-only moment, leading to sublattice Fe moments of 5 μ_B for the tetrahedral *A* sites and 4.5 μ_B for the octahedral *B* sites and a moment per formula unit of 4 μ_B. For magnetite, while the net magnetization is correctly predicted by this model, the sublattice moments are not: neutron diffraction measurements give $M_A = 4.2\ \mu_B$, $M_B = 3.97\ \mu_B$ at 130 K (Wright et al., 2002) and $M_A = 4.05\ \mu_B$, $M_B = 3.60\ \mu_B$ at 300 K (Klotz et al., 2006). This suggests that there is a degree of delocalization of the *d* electrons in magnetite. Band calculations (e.g., Zhang and Satpathy, 1991) indicate that magnetite is a semi-metal where the Fermi level intersects the minority spin 3*d* t_{2g}

bands of the Fe atoms on the octahedral sites. More recent calculations (Szotek et al., 2006) are based on the self-interaction corrected local spin density approximation, which gives a better account of electron correlations than other methods. They find that the lowest energy solution is ferrimagnetic with Fe^{3+} on both tetrahedral and octahedral sites, due to a delocalization of the sixth *d* electron of the original Fe^{2+} ions. The calculated sublattice moments are $M_A = 4.02\ \mu_B$ and $M_B = 3.90\ \mu_B$, which is close to the measured values.

The sublattice moments in greigite have similar magnitudes to each other, as in magnetite, and are even further removed from the localized model of Néel (1948), which suggests a higher degree of delocalization of the *d* electrons. The electronic structure of greigite, i.e., the valence state of iron, is still not clear. No band structure calculations are available for greigite so far, although spin-polarized multiple scattering calculations have been reported for Fe-S clusters (Braga et al., 1988). Their value for the moment per formula unit is 3.02 μ_B, which is close to the experimental value, but this agreement appears to be fortuitous because the *A* and *B* site moments were estimated to be 2.0 μ_B and 2.5 μ_B, respectively.

The magnetic structure model for greigite is consistent with Mössbauer spectroscopic measurements. The hyperfine fields for the *A* and *B* sites are -31.9 and -32.7 T, respectively, at 4 K, while at room temperature they are almost identical (-31.2 T, -31.5 T) (Chapter 5). This is in qualitative accord with the sublattice moments and their temperature dependence. The values of isomer shifts for greigite indicate that iron at the *A* sites is predominantly ferric, while the *B* sites are occupied by both ferrous and ferric ions if fast electronic hopping between them occurs (e.g., Coey et al., 1970; Spender et al., 1972; Vandenberghe et al., 1991; Chang et al., 2008). Application of a large magnetic field splits the Mössbauer spectra for greigite, with the hyperfine field at *A* sites increasing and that at *B* sites decreasing. The $\Delta M = 0$ transitions (lines 2 and 5) disappear at high fields, which is as expected if the magnetic moments are parallel or antiparallel to the applied field. These observations are consistent with a collinear ferrimagnetic structure.

X-ray magnetic circular dichroism (XMCD) spectra for greigite contain only two distinct absorption peaks, which so far have been attributed to the *B*-site Fe^{2+} and *B*-site Fe^{3+}, while the *A*-site absorption peak is not clear (Letard et al., 2005; Appendix B). Further analysis of such data appears to be necessary.

6.4.2. Origin of lower magnetic moments in greigite compared to magnetite

As obtained from high-resolution NPD patterns, the spontaneous magnetization M_s for greigite at room temperature is ~3.0 μ_B/f.u., which is slightly lower than the value of ~59 Am^2kg^{-1} (3.13 μ_B/f.u.) obtained from a superconducting quantum interference device (SQUID) magnetometer on bulk samples (Chapter 5). A similar contrast in results from different techniques has been observed for magnetite (e.g., Wright et al., 2002). This slight deviation for magnetite has been attributed to the residual orbital moments (e.g., Néel, 1948; Walz, 2002). It must be kept in mind that the sublattice moments measured by neutron diffraction correspond to the 3*d* component of the magnetization density: any spin transfer to the ligands (due to covalency or delocalization) would not be readily detected by neutrons because the magnetic form factor of the ligands drop rapidly with wave vector.

The apparently low M_s values for greigite in the literature (normally less than one-third that of magnetite) are not an intrinsic property of greigite because previously reported greigite samples were not pure and also had small particle size, leading to large SP fractions, as argued by Dekkers et al. (2000) and Chang et al. (2008). The synthetic greigite samples analysed in this study have been confirmed by a range of analyses to be virtually pure. Therefore, the measured M_s from these samples represents the most accurate published value for greigite (Chang et al., 2008). Surface magnetic effects may contribute to low M_s in fine particle systems. It is well known that spins in the surface layer can be inclined at various angles to the direction of net moment, as observed in many systems containing ultrafine magnetic particles, e.g., γ-Fe_2O_3 (e.g., Coey et al., 1971) and $NiFe_2O_4$ (Kodama et al., 1996). Unlike most of the synthetic greigite samples with significant SP behavior reported in the literature (e.g., Uda, 1965; Spender et al., 1972; Dekkers et al., 2000), our samples have much larger grain sizes (tens of μm) with only small concentrations of extremely fine particles (Chapter 5). There may be surface magnetic effects in our finest greigite grains, but their contributions can be ignored. Therefore, they should not cause a significant decrease of M_s in our synthetic greigite samples. The presence of vacancies can also lower M_s. For example, maghemite (γ-Fe_2O_3) has a similar inverse spinel structure as magnetite except that one-sixth of the *B* sites are occupied by vacancies ($[\uparrow Fe^{3+}]^{A}\ [\downarrow Fe_{5/3}^{3+}\ \square_{1/3}]^{B}\ O_4^{2-}$), which results in a lower M_s compared to magnetite. However, neutron scattering results indicate that there is no significant vacancy concentration in our greigite sample. Our overall conclusion is that the average magnetic moment for greigite is lower than for magnetite, but it is not as low as was previously thought. It is therefore necessary to explain why greigite has a lower spontaneous magnetization than magnetite.

The difference in M_s between magnetite and greigite probably relates to different degrees of covalency between Fe ions with oxygen and sulphur ligands, respectively, although greigite is considered to be the most ionic thiospinel. Increased covalency reduces the ionicity of the ions, which makes the ligands (O or S) less negative and the Fe cations less positive. Normally, covalency would be stronger with sulphur ligands than with oxygen because there should be more overlap of wave function between Fe and S ions (a larger covalency radius) compared to Fe and O ions. This increased covalency effect is also suggested by the lower hyperfine fields for greigite than for magnetite (e.g., Morice et al., 1969; Coey et al., 1970; Spender et al., 1972; Vandenberghe et al., 1991; Chang et al., 2008) and decreased separation between the absorption peaks for the Fe^{2+} and Fe^{3+} in octahedral sites in the XMCD spectra of greigite (Letard et al., 2005; Appendix B). From a band point of view, we can equate increased covalency with a higher degree of overlap and hybridization between the sulphur 3*p* and iron 3*d* bands. Neutron diffraction results for Fe_3Se_4, which has a defect NiAs structure, also indicate lower magnetic moments of the iron ions (Andersen, 1968). This is probably explained by a further increased covalency with selenium ligands. Coey et al. (1970) carried out conductivity measurements on synthetic greigite samples and showed that the resistivity was in the range of $10^{-1} – 10^{-3}$ Ω cm. They concluded that there is some electron delocalization in greigite, which is probably a result of cation-anion covalence because the *B*-*B* cation distance (3.49 Å) is probably too large for direct cation-cation overlap (Coey et al., 1970). The increased delocalization of electrons in greigite would effectively lower the ordered moment. We therefore conclude that the lower spontaneous magnetization of greigite compared to magnetite results from increased covalency between Fe and S ligands compared to O ligands, or from greater delocalization of the 3*d* electrons in greigite.

6.4.3. Absence of low-temperature structural changes in greigite

We cannot claim from our NPD and polarized neutron diffraction results to have demonstrated that greigite has no low-temperature equivalent to the Verwey transition because the crystallographic changes found at the Verwey transition in magnetite are subtle, and difficult to resolve (Wright et al., 2001, 2002). However, the smooth variation of our fitted parameters from room temperature to low temperature are consistent with other measurements that indicate that greigite has no low-temperature phase transition (Coey et al., 1970; Spender et al., 1972; Vandenberghe et al., 1991; Moskowitz et al., 1993; Roberts, 1995; Chang et al., 2007, 2008). It is not possible to explain the absence of a low-temperature phase transition in greigite at the moment, given that the mechanism for the Verwey transition is not yet fully understood. Regardless, we assume that the replacement of oxygen by sulphur in greigite has suppressed any analogue to the Verwey transition in greigite.

6.5. Conclusions

Neutron scattering experiments on pure synthetic greigite enable us to provide the first determination of its magnetic structure. These data provide a direct measure of the intrinsic magnetism of greigite. Our results confirm that greigite has a collinear ferrimagnetic structure, similar to the magnetic structure of magnetite above the Verwey transition. Our analysis of our neutron diffraction patterns indicates that greigite does not have a significant vacancy concentration and there is also no evidence of significant spin canting in greigite. The average magnetic moments of Fe ions for both the *A* and *B* sublattices at room temperature, refined from high-resolution NPD measurements, are ~3.0 μ_B with M_s of 3.0 μ_B/f.u. At 10 K, the *A*-site moment is 3.08 μ_B, while the *B*-site moment is 3.25 μ_B with M_s of 3.4 μ_B/f.u. The average magnetic moment of the Fe ions at the *B* sites decreases with increasing temperature, while the *A*-site moments vary little up to room temperature. This indicates that greigite is an R-type ferrimagnet, which is consistent with the measured lower *A*-*B* exchange interaction for greigite than magnetite. Neutron diffraction and magnetic measurements consistently indicate lower magnetic moments in greigite compared to magnetite. It is likely that the low magnetic moments in greigite arise from a higher degree of covalency between Fe ions and the sulphur ligands, or from greater delocalization of the 3*d* electrons. A band structure calculation for greigite is long overdue. No low-temperature crystal or magnetic structure change is evident for greigite in either the high-resolution NPD or the polarized neutron diffraction; this is consistent with other published data that demonstrate the lack of a low-temperature phase transition in greigite.

Chapter 7

Low-temperature magnetic properties of greigite

This chapter was published in *Geochemistry, Geophysics, Geosystems*, Volume 10, Chang, L., A. P. Roberts, C. J. Rowan, Y. Tang, P. Pruner, Q. Chen, and C-S. Horng, Low-temperature magnetic properties of greigite (Fe_3S_4), Q01Y04, doi:10.1029/2008GC002276, 2009. Copyright (2009), with permission of the American Geophysical Union and the Geochemical Society.

Abstract We provide comprehensive low-temperature magnetic results for greigite across the spectrum from superparamagnetic (SP) to multi-domain (MD) behaviour. It is well known that greigite has no low-temperature magnetic transitions, but we also document that it has strong domain-state dependence of magnetic properties at low temperatures. Blocking of SP grains and increasing thermal stability with decreasing temperature is apparent in many magnetic measurements. Thermally stable single domain greigite undergoes little change in magnetic properties below room temperature. For pseudo-single-domain (PSD)/MD greigite, hysteresis properties and first-order reversal curve diagrams exhibit minor changes at low temperatures, while remanence continuously demagnetizes because of progressive domain wall unpinning. The low-temperature demagnetization is grain size dependent for PSD/MD greigite, with coarser grains undergoing larger remanence loss. AC susceptibility measurements indicate consistent blocking temperatures (T_B) for all synthetic and natural greigite samples, which are probably associated with surficial oxidation. Low-temperature magnetic analysis provides much more information about magnetic mineralogy and domain state than room-temperature measurements and enables discrimination of individual components within mixed magnetic mineral assemblages. Low-temperature rock magnetometry is therefore a useful tool for studying magnetic mineralogy and granulometry of greigite-bearing sediments.

7.1. Introduction

Low-temperature ($T < 300$ K) rock magnetometry is widely used in rock magnetism and environmental magnetism (e.g., Dunlop and Özdemir, 1997; Moskowitz et al., 1998) for magnetic mineral identification, magnetic granulometry, quantification of superparamagnetism in ultra-fine-grained nanophases, and detection of magnetic ordering and phase transitions. Low-temperature magnetic measurements involve thermal dynamic processes, which provide much more information about magnetic systems than room-temperature analysis alone. Compared with high-temperature ($T > 300$ K) measurements, low-temperature methods also avoid chemical alteration.

The low temperature magnetic properties of magnetite have been extensively studied because of its importance as a terrestrial magnetic mineral, and because it undergoes the Verwey transition (a crystallographic change from a cubic to a monoclinic superstructure) at ~120 K and the magnetic isotropic point (where the magnetocrystalline anisotropy constant K_1 is zero and changes sign) at 130 K. In contrast, the magnetic behaviour of the thiospinel counterpart of magnetite, greigite, which forms in sulphate-reducing sedimentary systems (e.g., Berner, 1984), is less well known because it was generally considered to be metastable over geological timescales and therefore rare in natural systems. However, greigite has now been widely identified in marine and lake sedimentary sequences (e.g., Snowball and Thompson, 1988, 1990; Krs et al., 1990, 1992; Tric et al., 1991; Horng et al., 1992; Roberts and Turner, 1993; Reynolds et al., 1994; Florindo and Sagnotti, 1995; Housen and Musgrave, 1996; Roberts et al., 1996; Horng et al., 1998; Sagnotti and Winkler, 1999; Liu et al., 2004; Rowan and Roberts, 2006; Babinszki et al., 2007; Florindo et al., 2007; Frank et al., 2007; Ron et al., 2007; Vasiliev et al., 2007, 2008; Fu et al., 2008; Rowan et al., 2009) and it is also produced by magnetotactic bacteria in anoxic marine environments (e.g., Mann et al., 1990). Its increased recognition has made it more important to understand the magnetic properties of greigite. Published magnetic data for greigite have mostly been measured at room- or high-temperatures, while low-temperature data for greigite consist mainly of SIRM warming curves (Moskowitz et al., 1993; Roberts, 1995; Roberts et al., 1996; Torii et al., 1996; Chang et al., 2007), and a few other types of low-temperature measurements, e.g., hysteresis (Spender et al., 1972; Roberts, 1995; Dekkers et al., 2000; Chang et al., 2008) and FORC diagrams (Chang et al., 2007). Compared with high-temperature analysis, low-temperature analysis of greigite offers distinct advantages because of complications caused by chemical alteration at elevated temperatures (e.g., Spender et al., 1972; Krs et al., 1992; Roberts, 1995; Dekkers et al., 2000; Chang et al., 2008). We present comprehensive data for a range of low-temperature measurement techniques, using greigite samples that span the grain size spectrum from SP to MD behaviour.

7.2. Samples and methods

We analysed a range of natural and synthetic greigite samples. The natural greigite samples are from Neogene marine sediments from eastern New Zealand (Rowan and Roberts, 2006), Plio-Pleistocene marine sediments from the Lower Gutingkeng Formation, southwestern Taiwan (Horng et al., 1998; Jiang et al., 2001), upper Pliocene marine sediments from the Valle Ricca section near Rome, Italy (Florindo and Sagnotti, 1995; van Dongen et al., 2007), and Miocene lacustrine sediments from the Czech Republic (Krs et al., 1990). The New Zealand greigite samples are from two locations on the Mahia Peninsula, North Island, New Zealand: the 'NR' samples are from 'Nukutaurua Road', while the 'TC' samples are from 'Te Waipera Cemetery' (see Figure 1 of Rowan and Roberts (2006)). The New Zealand samples contain mixtures of SP and SD greigite (Rowan and Roberts, 2006). The samples from Taiwan and Italy contain typical SD greigite. The sample from the Czech Republic is a mixture of SD and MD greigite (Roberts et al., 2006). Pure synthetic greigite samples with dominantly coarse grains (labelled 'S') were prepared according to the hydrothermal method of Tang et al. (2007) by reacting $FeCl_3$ with CH_4N_2S and HCOOH at 170°C (Chang et al., 2008). The 'S' samples with mean grain sizes as large as 13 μm have PSD/MD behaviour (Chang et al., 2007). An additional fine-grained synthetic greigite sample (SYN06) was produced by solid state transformation of mackinawite (FeS) to pyrite via the intermediate greigite (Hunger and Benning, 2007). This synthetic sample is dominated by (non-magnetic) mackinawite but contains nanophase greigite particles (a few tens of nanometres across) (Hunger and Benning, 2007), which exhibit SP behaviour at room temperature (Roberts et al., 2006).

Low-temperature magnetic measurements were made at the Institute for Rock Magnetism, University of Minnesota, USA. Low-temperature hysteresis loops, back-field demagnetization curves and FORCs were measured using a Princeton Measurements Corporation vibrating sample magnetometer with a cryostat. FORC diagrams (Pike et al., 1999; Roberts et al., 2000) were determined from 80 FORCs (averaging time = 200 ms, field spacing = 1.85 mT, smoothing factor = 3), using the FORCinel software (Harrison and Feinberg, 2008). A Quantum Design MPMS was used for susceptibility and remanence measurements. For zero-field magnetization (ZFM) measurement, samples were cooled to 10 K in zero field. ZFM curves were recorded in a low field (2 mT) at stepwise increasing temperatures to 300 K. Samples were then cooled to 10 K in a low field (2 mT). Field-cooled magnetization (FCM) curves were measured in a low field (2 mT) during warming to room temperature. For ZFC and FC SIRM warming, samples were cooled to 10 K in either zero field or a large field (2.5 T). At 10 K, a 5 T field was applied and then switched off to impart a low-temperature SIRM. SIRM warming curves were measured during warming in zero-field. For LTC of a room-temperature SIRM, remanence was measured from room temperature to 10 K and back to room temperature in zero field. Alternating current (AC) susceptibility was measured with both the MPMS system and a Lakeshore

Susceptometer. Samples were cooled in zero field to either 4 K or 20 K and then measured in a low AC field at several frequencies up to 400 K.

7.3. Results

7.3.1. Low-temperature hysteresis properties

Hysteresis and backfield demagnetization parameters (B_c, B_{cr}, M_{rs}/M_s, and B_{cr}/B_c, where B_c is coercivity, B_{cr} is coercivity of remanence, M_{rs} is saturation remanent magnetization and M_s is saturation magnetization) for the studied greigite samples are variable below room temperature (Fig. 7.1). For typical SD greigite from Taiwan and Italy, B_c and B_{cr} decrease monotonically with warming. B_{cr} values are noisy because this parameter can be difficult to measure. M_{rs}/M_s also decreases monotonically with increasing temperature, but less rapidly than B_c and B_{cr}, and it always has values above 0.5 (Fig. 7.1c). B_{cr}/B_c is stable at low temperatures for SD greigite (Fig. 7.1d); values for the Italian greigite sample increase by only ~2% from 20 K to room temperature. Room temperature hysteresis parameters for a series of natural greigite samples (Snowball, 1997a, b) have similar values to those of our SD greigite samples measured at 50 K. This probably indicates that the greigite samples measured by Snowball (1997a, b) are even more thermally stable than our stable SD greigite samples.

Hysteresis parameters for coarse-grained synthetic greigite samples are nearly temperature independent below room temperature (Fig. 7.1). Chang et al. (2008) observed a local coercivity minimum at ~130 K for these samples, which is not visible at the scale of Fig. 7.1a. The minimum is probably associated with domain wall re-accommodations in the PSD/MD greigite samples.

Low-temperature hysteresis properties for the fine-grained synthetic greigite sample (SYN06) indicate progressive magnetic unblocking during warming (Fig. 7.1). B_c and B_{cr} decrease rapidly with increasing temperature (Fig. 7.1a, b), which is consistent with previous reports for fine-grained synthetic greigite (e.g., Coey et al., 1970; Spender et al., 1972; Dekkers et al., 2000). M_{rs}/M_s and B_{cr}/B_c are noisy, but generally M_{rs}/M_s decreases, and B_{cr}/B_c increases with warming (Fig. 7.1c, d). Hysteresis loops for a dominantly SP greigite sample NR08 (at room temperature, B_c = 4 mT, B_{cr} = 32 mT, M_r/M_s = 0.09) from New Zealand become broader at low temperatures (Fig. 7.1f), which is consistent with the behaviour of sample SYN06 (Fig. 7.1e), and

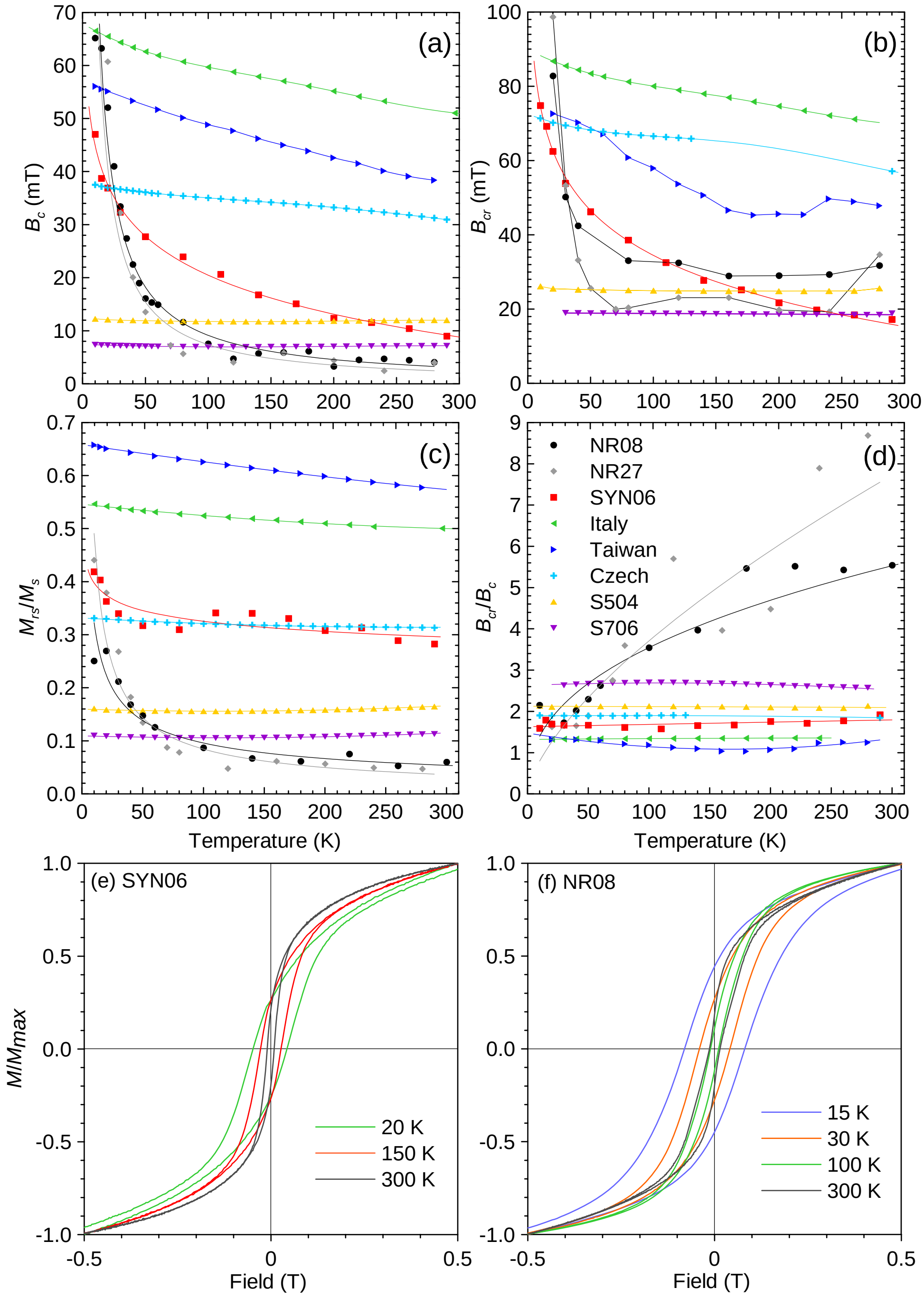

Figure 7.1. (a-d) Temperature variations of hysteresis and back-field demagnetization properties for greigite samples below room temperature: (a) B_c, (b) B_{cr}, (c) M_{rs}/M_s, and (d) B_{cr}/B_c. Solid lines connect data points or are best fits to the data. (e, f) Low-temperature hysteresis loops for greigite-bearing samples with significant SP behaviour. (e) Fine-grained synthetic greigite sample SYN06. (f) A magnetic separate of sample NR08. Note the broadening of the hysteresis loops as temperature decreases. The mean grain sizes for the synthetic coarse-grained samples S504 and S706 are ~4 μm and ~8 μm, respectively (cf. Chang et al., 2007). The "open" nature of the hysteresis loops at low-temperatures up to 0.5 T is probably associated with surficial oxidation.

indicates progressive blocking of fine magnetic particles with decreasing temperature. B_c and B_{cr} of sample NR08 decrease rapidly with warming, particularly below ~100 K (Fig. 7.1a, b). M_{rs}/M_s and B_{cr}/B_c approach SD values at ~10 K (Fig. 7.1c, d).

Low-temperature hysteresis data for natural greigite from the Czech Republic are intermediate between those of SD and PSD/MD samples (Fig. 7.1). B_c and B_{cr} decrease upon warming, with ~20% and ~23% decreases from 20 K to room temperature, respectively (Fig. 7.1a, b). Hysteresis ratios are more stable, with only ~5% and ~3% increases for M_{rs}/M_s and B_{cr}/B_c, respectively (Fig. 7.1c, d). These observations are consistent with the conclusion of Roberts et al. (2006) that this sample contains a mixture of SD and MD greigite.

7.3.2. Low-temperature FORC diagrams

Low-temperature FORC diagrams illustrate the domain-state characteristics for greigite (Fig. 7.2). FORC distributions indicate high coercivity and strong magnetostatic interactions for natural SD greigite (cf. Roberts et al., 2000, 2006; Rowan and Roberts, 2006; Florindo et al., 2007; Vasiliev et al., 2007), without substantial low temperature variations (Fig. 7.2a-d). The concentric SD contours migrate toward slightly higher coercivities as temperature decreases (Fig. 7.2a-d), as expected for progressive blocking of a small fraction of fine particles (Pike et al., 2001a). Interaction field distributions (B_i) for SD greigite undergo negligible changes at low temperatures, unlike SD magnetite (e.g., Carvallo and Muxworthy, 2006).

Although FORC distributions for fine-grained synthetic greigite are noisy, they migrate to higher coercivities at low temperatures (Fig. 7.2e-h), which confirms the dominantly SP behaviour at room-temperature for sample SYN06 (Roberts et al., 2006). This behaviour is consistent with models (Pike et al., 2001a) and with low-temperature observations for samples with dominantly SP behaviour (e.g., Carvallo and Muxworthy, 2006).

FORC distributions for PSD/MD greigite samples are unchanged at low temperatures (Fig. 7.2i-l) (Chang et al., 2007), as expected for MD assemblages. This contrasts with PSD magnetite, where FORC distributions split into two sets of concentric contours at low temperatures (e.g., Carvallo and Muxworthy, 2006; Smirnov, 2006). The splitting is probably associated with induced anisotropy effects (Smirnov, 2006), which do not appear to be present for greigite.

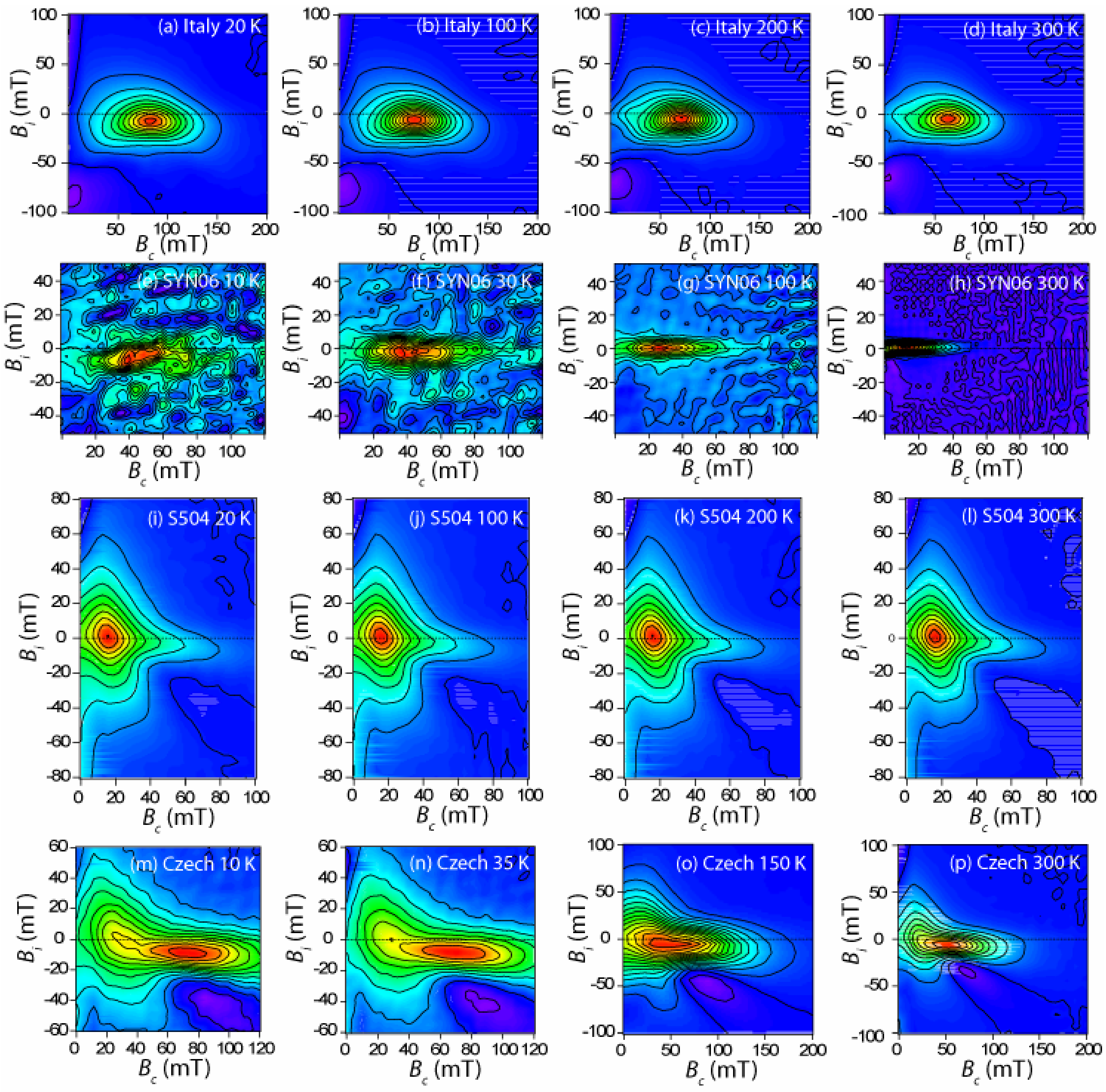

Figure 7.2. FORC diagrams for greigite samples at various temperatures. (a-d) A natural SD greigite sample from Italy. (e-h) Fine-grained synthetic greigite sample (SYN06) with dominantly SP behaviour at room temperature. (i-l) A coarse-grained synthetic greigite sample (S504) with dominantly PSD behaviour. (m-p) A natural greigite sample from the Czech Republic with a mixture of SD and PSD/MD grains. A smoothing factor (SF; see Roberts et al. (2000)) of 3 was used for all FORC diagrams; except for (e, f) for which SF = 5.

Low-temperature FORC diagrams for the Czech sample indicate mixed SD and PSD/MD behaviour, as suggested by Roberts et al. (2006). Migration of the concentric peak to higher coercivities at low temperature indicates SD behaviour with minor thermal relaxation, while the divergent outer contours indicate the presence of PSD/MD grains (Fig. 7.2m-p).

7.3.3. Low-temperature ZFM/FCM

When cooled in zero magnetic field, the magnetic moments of fine particles are randomly oriented. When subsequently warmed in a weak field from low temperature, magnetic moments of the randomly oriented particles become progressively aligned with the field due to increasing thermal energy. Maximum susceptibility (where magnetic moments are maximally aligned with the field) is observed at the blocking temperature (T_B). Above T_B, susceptibility decreases as thermal energy gradually randomizes the aligned magnetic moments (Dormann et al., 1997).

A ZFM curve for sample SYN06 rapidly increases upon warming (Fig. 7.3a), which indicates progressive alignment of magnetic moments with the weak field. The rapid increase over the whole temperature range probably indicates a broad grain size distribution. Although the mean T_B is above room temperature, there is significant SP behaviour at room temperature. ZFM/FCM curves for some New Zealand greigite samples indicate large paramagnetic contributions, as indicated in a plot of inverse susceptibility (Fig. 7.3b), which completely swamp ferrimagnetic greigite signals. After magnetic separation, sample NR08 has a dominant ferrimagnetic signal: the magnetization increases sharply from low temperature up to 120 K and decreases sharply from 270 K to room temperature with a broad plateau between 120 K and 270 K (Fig. 7.3c). By removing the paramagnetic susceptibility (from hysteresis loops; insert in Fig. 7.3d), ZFM/FCM curves can be produced that represent the ferrimagnetic signal. For sample NR27, which is dominated by SP behaviour at room temperature, a peak at ~120 K in the ZFM curve (Fig. 7.3d) indicates the mean T_B.

7.3.4. Low-temperature alternating current susceptibility

χ (T, f) curves (where T and f are temperature and frequency, respectively) for SD greigite increase slightly during warming (Fig. 7.4a), which suggests that the mean T_B is above room temperature. However, both the real χ' (T, f) and imaginary χ'' (T, f) components have frequency-dependent properties, which indicates the presence of some SP behaviour (Fig. 7.4a, d). A T_B between 6 K and 20 K is detected in the χ'' (T, f) curve (Fig. 7.4d). Coarse-grained synthetic greigite samples undergo small susceptibility variations at low temperatures (Fig. 7.4b), although a local susceptibility maximum was observed between 100 K and 110 K (Fig. 7.4b). This maximum does not

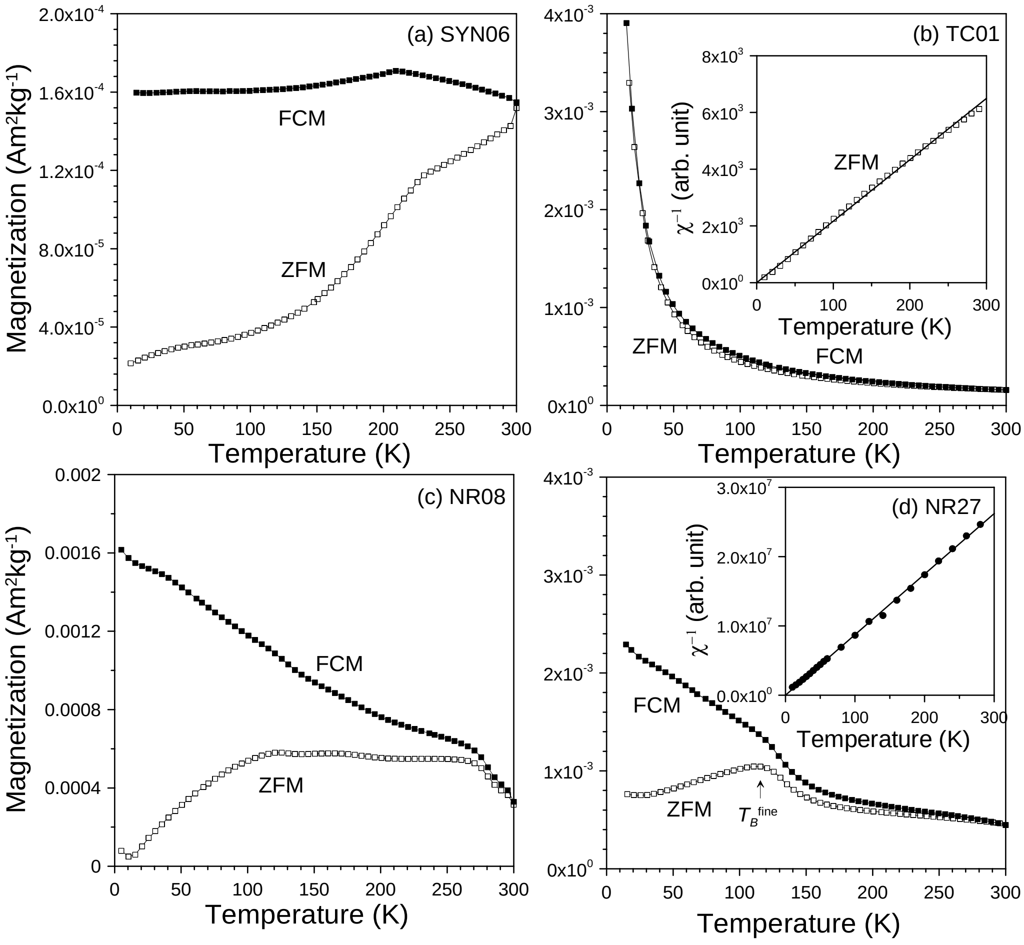

Figure 7.3. (a-d) ZFM/FCM curves for greigite samples in a small field (2 mT). The inserts in (b) and (d) are inverse ZFM curves that indicate dominant paramagnetism across the whole temperature range. (d) ZFM/FCM curves for a greigite-bearing sediment sample from New Zealand (sample NR27) after removing the paramagnetic magnetization, which was calculated from high-field magnetization measurements (insert). See text for detailed description.

likely represent a T_B because it does not display frequency-dependence and because it is not detected in the χ'' (T, f) curve at this temperature (Fig. 7.4b, e). This local susceptibility maximum is therefore probably an intrinsic property of PSD/MD greigite. Chang et al. (2008) observed a local coercivity minimum for the same samples at ~130 K, but it is not clear if these properties are related. SP behaviour (with a T_B between 8 K and 20 K) is indicated in the χ' (T, f) and χ'' (T, f) curves with strong frequency-dependence. The observed T_B below 20 K for both synthetic and natural greigite samples (Fig. 7.4d, e, f) probably has a similar origin. Chang et al. (2008) observed a magnetically ordered phase in synthetic greigite samples at 4 K from Mössbauer spectroscopy, which they attributed to slight surficial oxidation of greigite particles, which may be associated with the observed T_B below 20 K. This interpretation is supported by TEM observations of surfical oxidation on fine greigite grains (Letard et al., 2005; Kasama et al., 2006). χ' (T, f) curves for natural greigite-bearing sediments from New Zealand rapidly decrease upon warming (Fig. 7.4g-i), which indicates substantial paramagnetism. Weak ferrimagnetic greigite signals are often therefore swamped by paramagnetism. However, measurement of a magnetic separate (sample NR08) indicates characteristic frequency-dependent susceptibility that is associated with SP behaviour (Fig. 7.4c, f).

To remove the dominating effect of paramagnetic signals from matrix minerals, we linearly fitted the temperature-dependent paramagnetic AC susceptibility for $T < 50$ K to $1/T$ (Fig. 7.4j-l). We subtracted this paramagnetic susceptibility from the measured susceptibility to obtain the ferrimagnetic signal (Fig. 7.4m-o). Sample NR15 has a clear peak at ~180 K (Fig. 7.4m). The imaginary component χ'' (T, f) for this sample also has peaks at this temperature, which confirms a T_B of ~180 K. For samples TC15 and TC29, the ferrimagnetic susceptibility increases rapidly up to 190 and 120 K, respectively, and is followed by nearly stable susceptibility up to room temperature (Fig. 7.4n, o). These temperatures probably indicate the T_B for the SP component of the samples with a broader superposed grain size distribution that includes a stable SD component.

7.3.5. Low-temperature remanence

Cooling conditions (ZFC or FC) have no effect on SIRM warming of greigite because there is no low-temperature transition for greigite (Moskowitz et al., 1993; Chang et al., 2007). We therefore only show FC SIRM warming curves in Fig. 7.5. SIRM warming curves for samples dominated by SD greigite undergo minor decreases with warming (Fig. 7.5a, b), which agrees with the results of Roberts (1995). SIRM decreases by 23% and 30% from 20 to 300 K for the SD greigite samples from Italy and Taiwan, respectively, which indicates different SP contributions. The Czech sample has similar behaviour to a previously reported sample from this locality (Fig. 7.5c) (Moskowitz et al., 1993; Roberts, 1995). The SIRM for synthetic sample S706 (mean grain size of ~8 μm) decreases by 34% from 20 to 300 K (Fig. 7.5d), which is larger than the SIRM decrease (28%) for synthetic PSD sample S504 with smaller mean grain size (<4 μm; grain sizes are reported by Chang et al. (2007)). Low-temperature SIRM

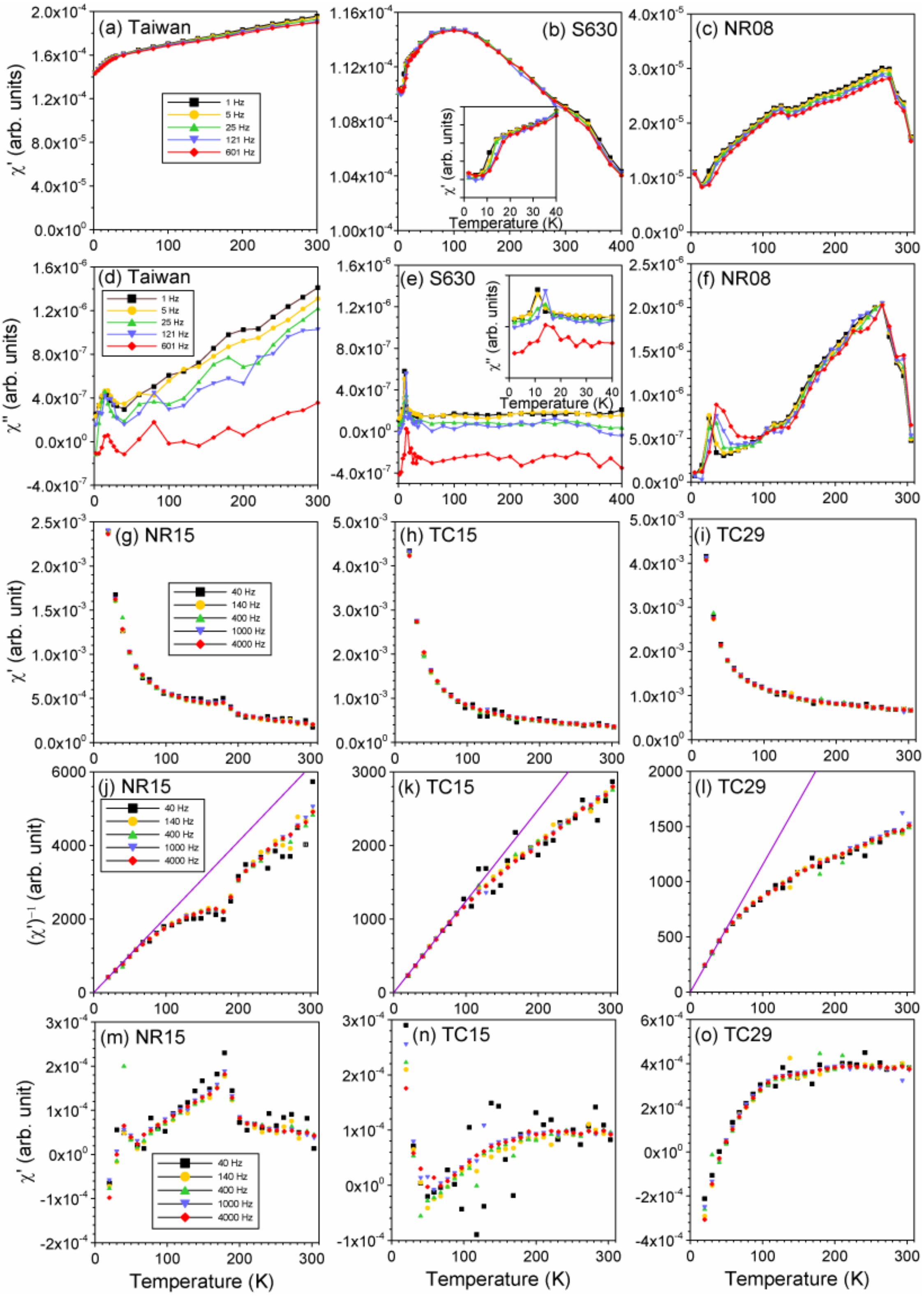
(a) Taiwan
χ' (arb. units)
2.0x10^-4
1.6x10^-4
1.2x10^-4
8.0x10^-5
4.0x10^-5
0.0x10^0
1 Hz
5 Hz
25 Hz
121 Hz
601 Hz
0
100
200
300
(b) S630
1.16x10^-4
1.12x10^-4
1.08x10^-4
1.04x10^-4
1.00x10^-4
χ' (arb. units)
0 10 20 30 40
Temperature (K)
0
100
200
300
400
(c) NR08
4.0x10^-5
3.0x10^-5
2.0x10^-5
1.0x10^-5
0.0x10^0
0
100
200
300
(d) Taiwan
χ'' (arb. units)
1.6x10^-6
1.2x10^-6
8.0x10^-7
4.0x10^-7
0.0x10^0
-4.0x10^-7
1 Hz
5 Hz
25 Hz
121 Hz
601 Hz
(e) S630
1.6x10^-6
1.2x10^-6
8.0x10^-7
4.0x10^-7
0.0x10^0
-4.0x10^-7
χ'' (arb. units)
0 10 20 30 40
Temperature (K)
(f) NR08
2.5x10^-6
2.0x10^-6
1.5x10^-6
1.0x10^-6
5.0x10^-7
0.0x10^0
(g) NR15
χ' (arb. unit)
2.5x10^-3
2.0x10^-3
1.5x10^-3
1.0x10^-3
5.0x10^-4
0.0x10^0
40 Hz
140 Hz
400 Hz
1000 Hz
4000 Hz
(h) TC15
5.0x10^-3
4.0x10^-3
3.0x10^-3
2.0x10^-3
1.0x10^-3
0.0x10^0
(i) TC29
5.0x10^-3
4.0x10^-3
3.0x10^-3
2.0x10^-3
1.0x10^-3
0.0x10^0
(j) NR15
(χ')^-1 (arb. unit)
6000
4000
2000
0
40 Hz
140 Hz
400 Hz
1000 Hz
4000 Hz
(k) TC15
3000
2000
1000
0
(l) TC29
2000
1500
1000
500
0
(m) NR15
χ' (arb. unit)
3x10^-4
2x10^-4
1x10^-4
0x10^0
-1x10^-4
-2x10^-4
40 Hz
140 Hz
400 Hz
1000 Hz
4000 Hz
Temperature (K)
(n) TC15
3x10^-4
2x10^-4
1x10^-4
0x10^0
-1x10^-4
Temperature (K)
(o) TC29
6x10^-4
4x10^-4
2x10^-4
0x10^0
-2x10^-4
-4x10^-4
Temperature (K)

Figure 7.4

warming curves for a range of coarse-grained synthetic greigite samples confirm that the remanence drop correlates with coercivity (insert in Fig. 7.5d), which is a sensitive indicator of grain size for PSD/MD greigite (e.g., Chang et al., 2007). Our results therefore indicate that low-temperature SIRM warming curves are grain-size dependent for PSD/MD greigite. Coarser-grained greigite undergoes larger remanence loss during warming, although unblocking due to minor SP particles will also contribute to remanence loss.

Our fine-grained synthetic greigite sample has complex SIRM warming behaviour (Fig. 7.5e). The abrupt remanence decrease from 10 to 20 K is probably due to impurities, such as an oxidized surface layer, e.g., iron oxide or hydroxide (Letard et al., 2005; Kasama et al., 2006). TEM observations indicate that this sample contains extremely fine greigite grains (Hunger and Benning, 2007). Therefore, surface oxidation could have a significant effect on the magnetic properties. The large remanence drop between 20 K and 230 K is likely due to unblocking of fine greigite particles. The relatively small decrease from 230 K to room temperature is probably due to an additional grain size distribution (i.e., there are bimodal and overlapping grain size distributions). The remaining remanence at room temperature is carried by SD grains, which is consistent with ZFM/FCM measurements that indicate a mixture of SP/SD grains. SIRM warming curves for the New Zealand greigite samples abruptly decrease between 20 and 300 K (Fig. 7.5f-i). First derivatives of SIRM warming curves indicate the presence of minor magnetite in the greigite-dominated TC samples (Fig.

Figure 7.4. (a-f) The AC susceptibility for three greigite samples with SP and SD and PSD/MD properties during warming. The inserts in (b) and (e) are expanded views of the main susceptibility curves. (g-i) The measured AC susceptibility (real component χ' (T, f)) for natural greigite samples from eastern New Zealand. (j-l) The inverse AC susceptibility for the same samples in (g-i). Lines are linear fits to $\chi^{-1} = A \cdot T$ (where χ and T are susceptibility and temperature, respectively; A is a coefficient) for $T < 50$ K, which represent paramagnetic signals. The measured susceptibility data deviate from linearity at elevated temperatures, which indicates the increasing dominance of ferrimagnetic signals and a rapidly decreasing influence of paramagnetic susceptibility with increasing temperature. (m-o) Susceptibility curves after subtraction of the fitted paramagnetic susceptibility from the measured susceptibility for greigite samples in (g-i). These curves represent ferrimagnetic greigite signals with variable grain size distributions. See text for detailed description. Samples in (a-f) and (g-o) were measured with MPMS and Lakeshore Susceptometer systems, respectively.

7.5g-i), which is likely to be from detrital tuffaceous material that was not dissolved during reductive diagenesis (Rowan and Roberts, 2006). Magnetite, even when present in small concentrations, can be detected by low-temperature magnetic measurements because of the effect of the Verwey transition. Regardless, trace amounts of magnetite do not significantly affect our conclusions.

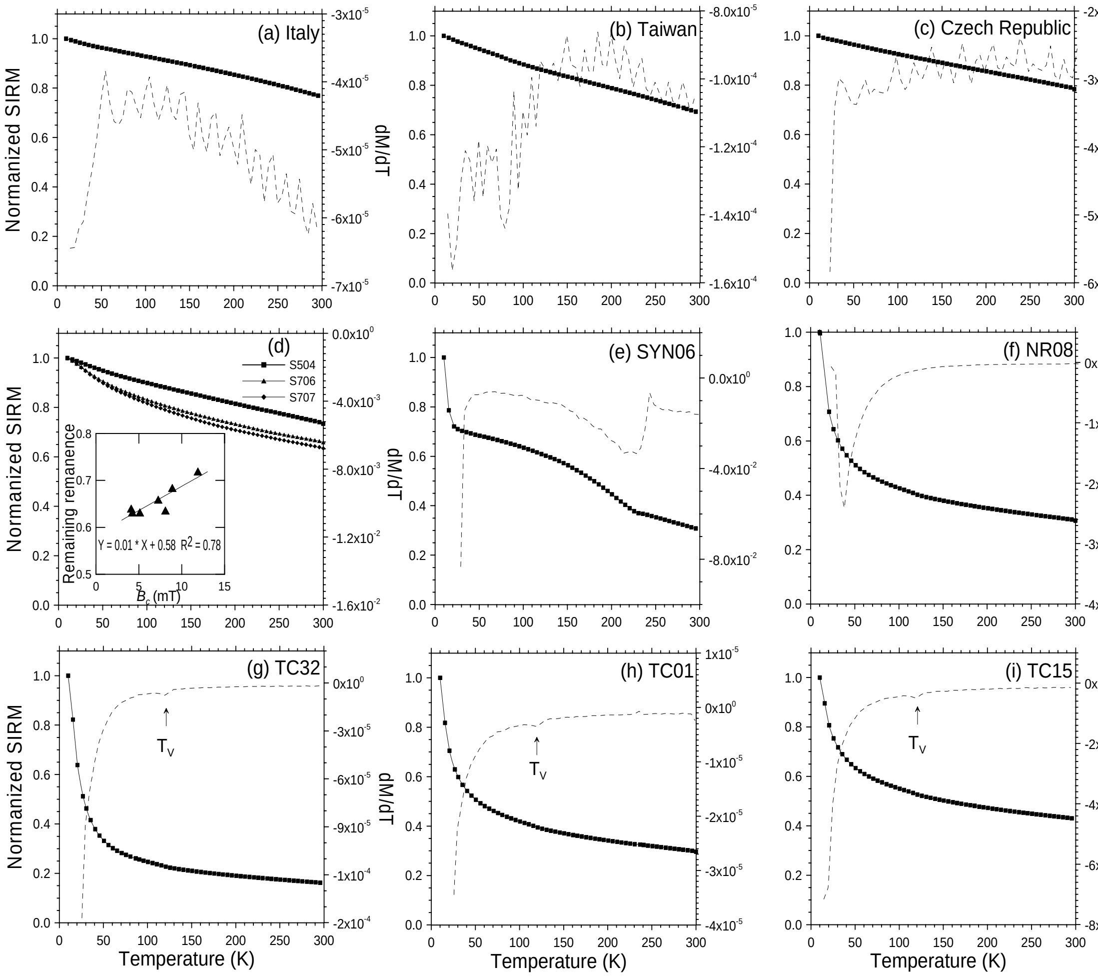

Figure 7.5. SIRM warming curves for greigite samples. Solid points represent measured data. Dashed lines are the first derivative of the SIRM with respect to temperature (d*M*/d*T*). The SIRM was imparted in a 5 T field at 10 K. T_V represents the Verwey transition for magnetite. The insert in (d) is the correlation between coercivity and remaining remanence after zero-field SIRM warming from 10 K to 300 K for a range of synthetic PSD/MD greigite samples.

Finally, LTC measurements of a RT-SIRM for a natural SD greigite sample and for a range of coarse-grained synthetic samples resemble the results of Chang et al. (2007), which indicate contrasting behaviour for SD and PSD/MD samples (Fig. 7.6a).

SP particles make no contribution to remanence, so they are not relevant to LTC of RT-SIRM measurements. For SD greigite (from Taiwan), the remanence increases slightly due to decreased thermal energy upon cooling (Dekkers et al., 2000; Chang et al., 2007). The remanence memory is nearly complete when warmed back to room temperature. In contrast, PSD/MD greigite demagnetizes during cooling and the warming curve is irreversible with respect to the cooling curve (Chang et al., 2007). Measurements on coarse-grained synthetic greigite samples indicate that the remanence memory after LTC is strongly correlated to B_c, which, in turn, is dependent on grain size (Fig. 7.6b). LTC of a RT-SIRM therefore provides a useful tool for magnetic granulometry by enabling discrimination between SD and PSD/MD grains.

7.4. Discussion

Comprehensive low-temperature magnetic measurements of SP to MD greigite consistently provide no evidence of a low-temperature transition. This confirms previous observations (e.g., Coey et al., 1970; Spender et al., 1972; Moskowitz et al., 1993; Roberts, 1995; Torii et al., 1996; Dekkers, et al., 2000; Chang et al., 2007, 2008). There is also no evidence for a low-temperature phase transition from structural investigations from either Mössbauer spectroscopy (Vandenberghe et al., 1991; Chang et al., 2008) or neutron scattering (Chapter 6). Greigite probably also has no low-temperature magnetic isotropic point. Low-temperature SIRM warming curves have been used to discriminate greigite from other magnetic minerals with low-temperature magnetic transitions, e.g., magnetite and pyrrhotite (Fe_7S_8) (e.g., Moskowitz et al., 1993; Roberts, 1995; Housen and Musgrave, 1996; Roberts et al., 1996; Torii et al., 1996; Horng et al., 1998; Jiang et al., 2001; Babinszki et al., 2007). However, it should be noted that the absence of a magnetic transition does not enable positive identification of greigite. Additional analyses, e.g., X-ray diffraction (XRD) and scanning electron microscope SEM observations, are needed to enable unambiguous detection.

At room temperature, hysteresis parameters for greigite-bearing sediments from eastern New Zealand (Rowan and Roberts, 2006) fall on a similar trend to SP/SD mixing lines calculated for magnetite (Dunlop, 2002). Representative hysteresis loops are slightly wasp-waisted (Fig. 1f; Rowan and Roberts, (2006)), which is consistent with the presence of SP/SD mixtures (Roberts et al., 1995). The dominantly SP greigite

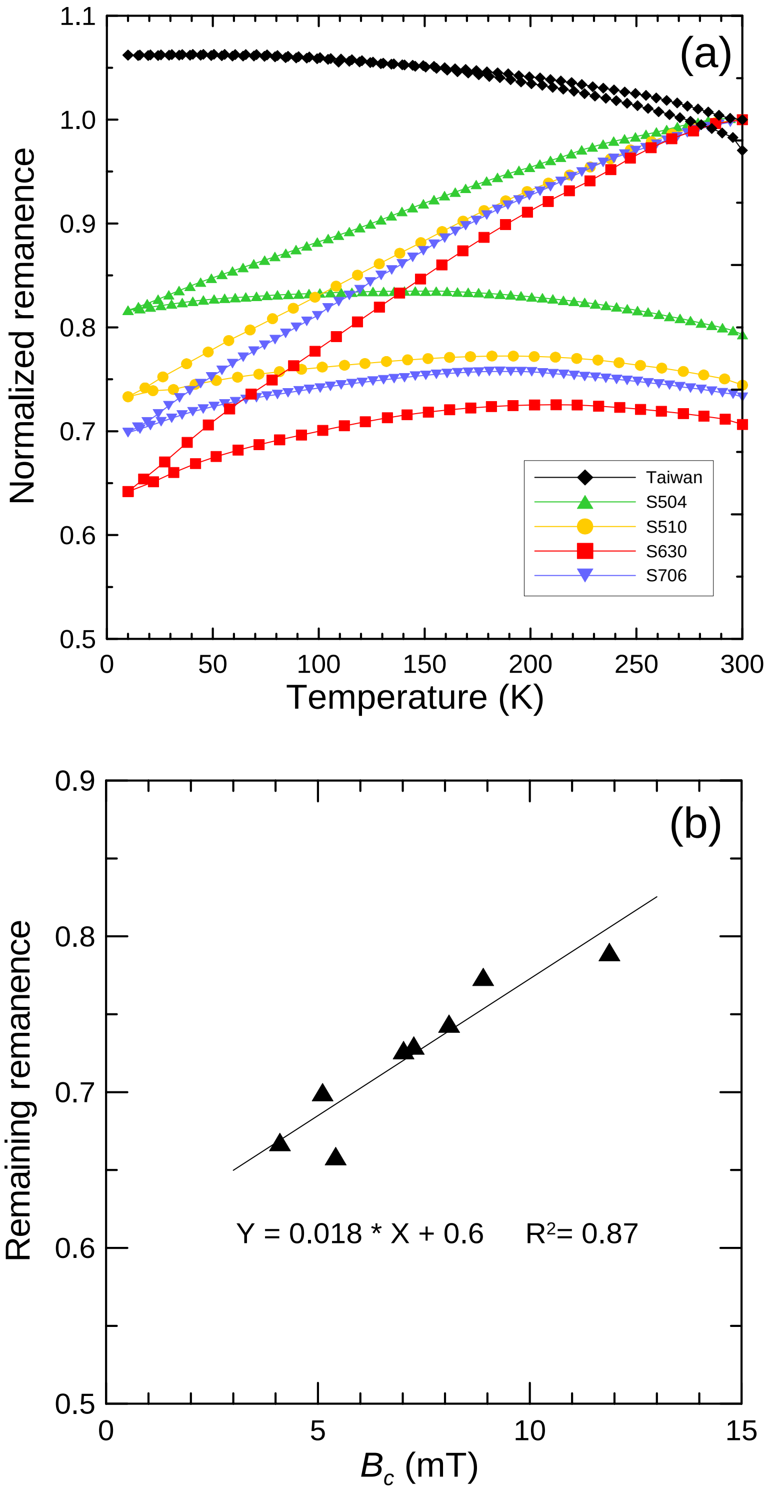

Figure 7.6. (a) Normalized zero-field cooling and warming of a RT-SIRM for a representative range of greigite samples that span the grain size range from SD to PSD/MD. (b) The correlation between coercivity and remaining remanence after zero-field LTC of RT-SIRM for a range of synthetic PSD/MD greigite samples. Mean grain sizes for the synthetic coarse-grained greigite samples S504, S510, S630, and S706 are ~4 μm, ~9 μm, ~11 μm, and ~ 8 μm, respectively (cf. Chang et al., 2007).

samples undergo the most rapid low temperature change in magnetic properties. Low-temperature hysteresis measurements, along with ZFM/FCM and low-temperature AC susceptibility curves, also confirm the dominance of SP behaviour in these sediments. Variations in the observed T_B reveal fine but variable grain size distributions. SP behaviour is also present in samples dominated by SD greigite (e.g., B_c decreases by ~28% and ~44%, while SIRM decreases by 23% and 30% from 20 to 300 K for the natural greigite samples from Italy and Taiwan, respectively). These low-temperature observations are consistent with room-temperature hysteresis measurements, where the Italian sample has a larger B_c value than the sample from Taiwan (50 versus 44 mT). The different decreases probably reflect different SP contributions. SP behaviour in greigite-bearing sediments is unsurprising considering that greigite progressively grows from solution to a finite grain size, which favours formation of ultra-fine particles (Rowan and Roberts, 2006). Progressive blocking during cooling to low temperatures means that B_c, B_{cr} and M_{rs}/M_s increase rapidly where SP behaviour dominates, while B_{cr}/B_c decreases rapidly with decreasing temperature (cf. Coey et al., 1970; Spender et al., 1972; Dekkers et al., 2000). Concentric FORC contours move rapidly to higher coercivities. ZFM/FCM and AC susceptibility curves for dominantly SP samples have characteristic maxima that correspond to the mean T_B of the fine greigite particles. Low-temperature SIRM also decreases rapidly during warming (cf. Roberts, 1995; Chang et al., 2007).

SD greigite has relatively stable magnetic properties at low temperatures. Hysteresis parameters undergo only small changes, with slightly increasing B_c, B_{cr} and M_{rs}/M_s, and decreasing B_{cr}/B_c during cooling. FORC diagrams indicate a minor migration of the SD distribution toward higher coercivities with decreasing temperature, but these changes are much smaller than for dominantly SP samples. ZFM and AC susceptibility increases slightly during warming. SIRM decreases slightly from low to room temperature (cf. Roberts, 1995; Chang et al., 2007). Zero-field cycling of RT-SIRM indicates a small increase during cooling, with nearly reversible warming curves (e.g., Chang et al., 2007).

Temperature dependence of magnetic properties for PSD/MD greigite is mainly controlled by domain-wall movements. Magnetization (hysteresis, FORC, ZFM/FCM, AC susceptibility) is usually stable, while remanence (warming, zero-field cycling) is unstable. He et al. (2006) observed low-temperature magnetization jumps in ZFM curves for a synthetic greigite microrod, which they attributed to domain wall pinning effects. We did not observe such behaviour, probably because of a comparatively low magnetic anisotropy for our more equant PSD/MD greigite samples (Chang et al., 2008). By contrast, the remanence is demagnetized in our samples at low temperatures as domain walls become progressively unpinned. Low-temperature demagnetization of SIRM for PSD/MD grains is associated with domain wall unpinning (e.g., Moskowitz et al., 1998). Low-temperature SIRM warming curves vary with grain size for PSD/MD greigite: coarser-grained greigite undergoes larger demagnetization. More MD-like greigite can lose significant remanence, which could be misinterpreted as SP behaviour. Complementary measurements are therefore needed to resolve such ambiguities. Zero-field cycling of RT-SIRM causes significant demagnetization during cooling, and warming curves are not reversible with respect to cooling curves (Chang et al., 2007). This irreversible demagnetization is probably associated with domain re-ordering, i.e., domain wall re-equilibration or domain nucleation due to temperature-dependent changes in magnetocrystalline anisotropy and trans-domain processes (Chang et al., 2007), similar to cooling processes that cause remanence decreases in PSD/MD magnetite above the Verwey transition (Muxworthy et al., 2003).

7.5. Conclusions

Greigite undergoes no low-temperature transition and it probably has no magnetic isotropic point. Low-temperature measurements indicate strong domain-state dependence of magnetic properties for greigite. SP behaviour produces major changes in low-temperature measurements. SP greigite is widespread in greigite-bearing sediments, even in typical natural SD greigite samples, and can be detected despite large SD or PSD/MD background signals using SIRM warming, ZFM/FCM curves and AC susceptibility. A T_B below 20 K was consistently observed in our greigite samples by AC susceptibility measurements, which we attribute to minor surface oxidation of greigite grains. SD greigite has relatively stable magnetic properties; coercivity increases slightly as thermally relaxed grains magnetically block at low temperature. For PSD/MD greigite, hysteresis properties, FORC diagrams, ZFM/FCM curves and AC susceptibility are stable, while remanence demagnetizes significantly due to domain wall unpinning. MD greigite can undergo significant remanence loss during warming, which can be misinterpreted as SP behaviour. Complementary measurements are therefore needed to resolve this potential ambiguity. Low-temperature magnetic measurements have the potential to unravel contributions from either mineral mixtures or mixed domain states, which provides much more information than room-temperature measurements. Low-temperature rock magnetometry can therefore be widely useful for studying magnetic mineralogy and granulometry of greigite-bearing materials.

Chapter 8

Conclusions and recommendations for future work

8.1. Conclusions

In this study, new results have been presented concerning the magnetic properties of greigite. These results provide many important new insights about greigite, including its micromagnetic structure and macroscopic magnetic properties, ranging from SP to MD behaviour, and from 4 K to high temperatures. In addition to the conclusions discussed in Chapters 4 to 7, the main conclusions and implications of this study are summarized below.

8.1.1. Production of highly pure greigite samples

Most previous chemical synthesis methods have failed to produce pure greigite samples, which demonstrates the difficulties in synthesizing high quality greigite samples (Chapter 5; Appendix A). A new recipe for synthesizing greigite has been explored in this study (Chapter 5) and is based on the approach of Tang et al. (2007) in which ferric chloride is reacted with thiourea and formic acid at 170°C. XRD, neutron diffraction, Mössbauer spectroscopy and SEM observation with elemental analyses all confirm the high purity of the studied suite of synthetic greigite samples (Chapters 5, 6). These analyses also indicate that, compared to other reported greigite samples, the studied synthetic greigite samples have much larger grain size and good crystallinity (Chapters 4, 5). Production of pure greigite samples has made it possible to investigate the fundamental magnetic properties of greigite for the first time in this study.

8.1.2. Unambiguous determination of the magnetic structure of greigite

The magnetic structure of greigite has been considered to be the same as that of magnetite because of their similar crystallographic structure. However, no direct determination of the magnetic structure of greigite has been reported. Previous studies indicated that the M_s of greigite is much lower than for magnetite (Table 5.1), which is difficult to reconcile with the assumed magnetic structure of greigite (Chapter 6). In this study, a range of analyses, including neutron scattering (Chapter 6), Mössbauer spectroscopy (Chapter 5) and XMCD (Appendix B) have been used to probe the magnetic structure of greigite. Neutron powder diffraction also enabled determination of the average magnetic moments of Fe ions for the two sublattices. This study confirms that greigite has a collinear ferrimagnetic structure with antiferromagnetic coupling between the tetrahedral and octahedral sites. But the average magnetic moments for the two sublattices of greigite are slightly lower than those of magnetite. Several studies have proposed the possible presence of vacancies in greigite (e.g., Letard et al., 2005; Rickard and Luther, 2007). However, Rietveld analysis of the neutron powder diffraction patterns obtained in this study provides strong evidence that the studied synthetic greigite sample does not have a significant concentration of vacancies (Chapter 6). For the first time, the results of this study provide a direct measure of the intrinsic magnetism of greigite.

8.1.3. Newly determined fundamental magnetic parameters for greigite

In addition to determining the magnetic structure, production of pure greigite samples enables determination of fundamental magnetic parameters that were previously either unknown or poorly constrained (Chapters 5, 6).

8.1.3.1. Saturation magnetization

Using pure synthetic greigite samples, the M_s of greigite at room temperature was determined to be 59 $\mathrm{Am^2kg^{-1}}$ (equivalent to 3.13 μ_B/f.u.) from magnetic measurements (Chapter 5) and 3.03 μ_B/f.u. from neutron scattering (Chapter 6). These values are much higher than previous estimates from impure greigite samples (Table 5.1). However, neutron diffraction and magnetic measurements consistently indicate a slightly lower magnetic moment in greigite compared to magnetite. The low magnetic moment in greigite compared to magnetite is probably caused by an increased degree of covalency between iron and sulphur compared to oxygen ligands (which has been confirmed by XMCD measurements, Appendix B), or by greater delocalization of the 3*d* electrons in greigite (Chapter 6).

8.1.3.2. Sublattice magnetizations

Unlike magnetic methods, which can only measure the total magnetization of a magnetic material, neutron scattering provides a unique tool to measure sublattice magnetizations. Rietveld profile analysis of the neutron powder diffraction patterns gives M_A = ~3.0 μ_B, M_B = ~3.0 μ_B, with M_s = 3.0 μ_B/f.u. at room temperature and M_A = ~3.25 μ_B, M_B = ~3.0 μ_B, with M_s = 3.5 μ_B/f.u at 10 K (Table 6.1). The Fe moment of the *A* sites decreases with increasing temperature, while the *B*-site moment is relatively stable at low temperatures. This type of sublattice magnetization curve indicates that greigite is probably an R-type ferrimagnet, unlike magnetite, which is a Q-type ferrimagnet. This is probably because the *A*-*B* exchange interaction for greigite is much lower than for magnetite (Chapter 5).

8.1.3.3. Exchange constant

By measuring the low-temperature M_s of pure greigite and based on the Bloch spin wave expansion, the spin wave stiffness *D* of greigite was determined for the first time as ~193 meV·Å^2, with a corresponding exchange constant J_{AB} of ~1.03 meV. The determined exchange constant for greigite is lower than that of magnetite. The replacement of oxygen by sulphur in the spinel crystal lattice in greigite is likely to have decreased the *A*-*B* superexchange coupling.

8.1.3.4. Curie temperature?

It is difficult to determine the Curie temperature for greigite because greigite decomposes at elevated temperatures. High-temperature magnetic analyses therefore reveal chemical decomposition effects rather than the T_C (Krs et al., 1992; Reynolds et al., 1994; Roberts, 1995; Dekkers et al., 2000). The T_C for greigite remains unknown despite variable estimations reported in the literature (Spender et al., 1972; Vanderberghe et al., 1991; Roberts, 1995). High-temperature analysis on an extremely stable greigite nodule from Italy, as analyzed in this study, indicates that T_C must exceed 350°C in greigite (Chapter 5).

8.1.4. Domain state dependence of the magnetic properties of greigite

The magnetic properties of PSD/MD greigite are poorly known because of difficulties in producing large enough greigite samples to develop non-uniform magnetization within individual grains. There has only been one previous study of the PSD/MD behaviour of greigite (Hoffmann, 1992). The new hydrothermal synthesis method enables production of greigite crystals that are sufficiently large (with mean grain size up to 14 μm and maximum individual grain size up to 44 μm) to exhibit PSD/MD behaviour (Chapters 4, 5). In this study, knowledge of the magnetic behaviour of greigite has been extended to cover the range of magnetic properties across the SP, SD and PSD/MD states (Chapters 4, 7). Production of greigite samples with knowing grain size has enabled a first study of the grain-size dependent magnetic properties of greigite (Chapter 4). SD properties are widely used to identify greigite in sediments (cf. Roberts, 1995). However, Rowan and Roberts (2006) found that SP greigite is common in rapidly-deposited marine sediments, which means that use of SD properties to identify greigite will lead to widespread underestimation of its presence in sediments. Results presented in Chapter 4 indicate that the coercivity of PSD/MD greigite (Table 4.1) overlaps with that of PSD/MD magnetite. The lack of a low-temperature magnetic transition in greigite means that it is also possible to confuse the low-temperature behaviour of greigite with that of maghemite or partially oxidized magnetite (Chapters 4, 7). This non-uniqueness means that the presence of PSD/MD greigite in sediments can go unrecognized unless additional high- and low-temperature magnetic measurements are made.

8.1.5. The magnetic behaviour of greigite at low temperatures

It is well known that greigite has no low-temperature magnetic transitions (cf. Roberts, 1995), but data presented in Chapters 4 and 7 document for the first time that the magnetic properties of greigite have strong domain-state dependence at low temperatures. Blocking of SP grains is apparent below room temperature. SD greigite undergoes little change in magnetic properties at low temperatures. For PSD/MD greigite, hysteresis properties and FORC diagrams exhibit minor changes at low temperatures, while remanence continuously demagnetizes because domain walls become progressively unpinned. Clear and gradual changes in magnetic properties are evident for greigite across the grain size spectrum from SP to MD behaviour. In addition, a consistent T_B was detected at low temperatures for all synthetic and natural greigite samples, which is probably associated with surficial oxidation. Low-temperature rock magnetic analyses therefore provide a useful tool for studying the magnetic granulometry and surface oxidation of greigite in sediments (Chapter 7).

8.2. Suggestions for future work

Results presented in this thesis have provided fundamental new data, but they also pave the way for important future research. Production of pure, size-controlled synthetic greigite samples makes it possible to determine the remaining unknown magnetic properties of greigite, such as the magnetocrystalline anisotropy constant, a complete grain-size dependent magnetic property framework, and the critical SP/SD and SD/two-domain threshold sizes. Band structure calculation (e.g., Szotek et al., 2006) is needed to investigate the electronic structure of greigite, to compare with the new neutron scattering, XMCD and Mössbauer spectroscopy data presented in this study. Determinations of the key fundamental magnetic parameters in this study, such as M_s and the exchange constant, along with the future determination of the anisotropy constant and domain threshold sizes, will enable micromagnetic modelling of fine greigite grains. Such modelling will enable testing of the palaeomagnetic recording fidelity for a range of microscopic grain configurations from a theoretical perspective. Further details of these suggestions for future work are described below.

8.2.1. Determination of the remaining fundamental magnetic parameters for greigite

8.2.1.1. Magnetocrystalline anisotropy constant

The magnetocrystalline anisotropy constant K_1 for greigite remains undetermined, although Spender et al. (1972) suggested a K_1 value of 10^5 J/m^3, while Diaz-Ricci and Kirschvink (1992) suggested a value of 10^3 J/m^3. These disparate values are rough estimates only and are not experimentally determined. The conventional technique to measure K_1 is by employing a torque magnetometer on large single crystals (> mm scale). This is not possible even for the largest currently available synthetic greigite single crystals. For currently available greigite samples, multiple approaches, such as cantilever magnetometer, ferromagnetic resonance (FMR) and high-field magnetization measurements, can be employed to directly estimate K_1. A cantilever magnetometer is a miniaturized version of a torque magnetometer that allows measurement of macroscopically small single crystals (Martín-Hernández et al., 2006). FMR is a form of electron spin resonance, which has been used to probe K_1 in magnetotactic bacteria (Kopp et al., 2006). The 'law of approach' to saturation describes the dependence of magnetization on applied magnetic field. K_1 can be determined by fitting high-field hysteresis curves according to Chikazumi (1997). Using these multiple methods will enable a test of the robustness of each estimate.

8.2.1.2. Magnetostriction constants

Determination of the magnetostriction constants λ is difficult without employing a recording rotating field magnetometer on large single crystals (e.g., Moskowitz, 1993). Experimental determination of λ can therefore only be achieved by advances in synthesizing much larger greigite single crystals than is currently possible.

8.2.1.3. Curie temperature

Direct determination of T_C of greigite has proven to be impossible because greigite decomposes below T_C. A more creative approach is therefore needed to enable estimation of T_C for greigite. Cation-substitution (e.g., Al, Ti) in magnetic materials will reduce T_C, as is the case, for example, in titanomagnetites. It is possible to introduce non-magnetic cations, e.g., Al, into greigite crystals (Dr. Yan Tang, Wuhan University of Science and Technology; personal communication, 2008), which should reduce T_C to below the alteration temperature. By measuring T_C for a range of nonstoichiometric substituted greigite samples, it should be possible to extrapolate T_C to the value for stoichiometric greigite to provide an estimate of T_C for greigite.

8.2.2. Magnetic domain observations for greigite

The production of coarse-grained greigite, which is large enough to develop domain walls (Chapter 4), makes it possible to carry out domain observations. Compared to the natural greigite samples investigated by Hoffmann (1992), the studied synthetic greigite samples should have simple domain patterns because it is expected that hydrothermally synthesized materials will have reduced magnetostriction effects. Domain observations on these synthetic greigite samples should provide a promising line of investigation because, for example, direct observation of domain wall width can be used to calculate domain size thresholds.

8.2.3. A complete grain size dependent magnetic framework for greigite

A full grain size dependent magnetic property framework needs to be determined for greigite, along with the lower and upper grain size thresholds for stable SD behaviour. This problem can be addressed using a combination of experimental and theoretical approaches. Magnetic properties, such as hysteresis, can be measured on size-controlled samples to provide empirical estimates. From a theoretical perspective, micromagnetic modelling enables prediction of the domain states of particles with various sizes and shapes.

8.2.4. Micromagnetic modelling of fine greigite particles

M_s and the exchange constant for greigite were determined in this study. Determination of the remaining fundamental magnetic parameter K_1 for greigite will enable micromagnetic modelling to understand the magnetization of greigite on small (sub-micron) length scales. For example, modelling will enable determination of the grain size dependence of domain state for greigite and assessment of the effects of magnetostatic interactions on palaeomagnetic recording. Such modelling will provide a basis for understanding whether strong magnetostatic interactions can explain the commonly observed anomalies (e.g., contradictory polarities; Jiang et al. (2001)) in magnetic recording associated with greigite.

8.3. Summary

The results reported in Chapters 4 to 7 represent the first precise estimates of several key magnetic parameters for greigite, the first determination of the magnetic structure of greigite, and the first report of a domain-state dependent framework for the magnetic properties of greigite. While the work presented here provides a major step forward, the research suggested above will provide a feasible means of determining the remaining parameters that are needed to obtain a complete understanding of the magnetic properties and palaeomagnetic recording fidelity of greigite.

Appendix A

Greigite synthesis

Before greigite was formally identified in natural environments (Skinner et al., 1964), Yamaguchi and Katsurai (1960) synthesized a magnetic iron sulphide with the composition Fe_3S_4 and spinel structure, which was later confirmed to be greigite (Uda, 1965). In this hydrothermal method, a sodium sulphide solution was reacted with Mohr's salt (ferrous ammonium sulphate). Most subsequent recipes for greigite synthesis were based on this method (e.g., Uda, 1965; Yamaguchi and Wada, 1969, 1971; Dekkers and Schoonen, 1996). Rapid quenching in cold water after autoclaving is considered to be essential to produce purer greigite samples (Uda, 1965; Yamaguchi and Wada, 1969; Dekkers and Schoonen, 1996). These synthetic samples normally contain fine greigite grains with SP properties at room temperature (e.g., Uda, 1965; Coey et al., 1970; Spender et al., 1972; Snowball, 1991; Roberts, 1995; Dekkers and Schoonen, 1996; Dekkers et al., 2000). Synthesizing highly pure greigite samples is difficult because greigite is a metastable intermediate product in these reactions. While the conventional hydrothermal method described above and other approaches (Richard and Luther, 2007, and references therein) enables production of greigite with reasonable purity, these synthetic greigite samples are disadvantaged by contamination, poor crystallinity and small grain size, which makes it difficult to characterize the intrinsic magnetic properties of greigite. Several new methods have recently been proposed to synthesize pure greigite (e.g., Qian et al., 1999; Chen et al., 2005; He et al., 2006; Tang et al., 2007; Han and Guo, 2008), which provide important clues for synthesizing high quality greigite samples. A brief summary of these methods is given below.

In the toluene thermal process (Qian et al., 1999), $FeSO_4{\cdot}7H_2O$ is reacted with Na_2S_3 at 80°C in an excess of toluene for 24 hours. After autoclaving, the solution is naturally cooled to room temperature. This toluene-thermal reaction process is probably a liquid-solid reaction (Qian et al., 1999):

$$3FeSO_4 + 3Na_2S_3 \rightarrow Fe_3S_4 + 3Na_2SO_4 + 5S.$$

Nitrite red spectrophotometry analysis determined the chemical composition for this synthetic greigite to be $Fe_{2.994}S_4$, which indicates nearly stoichiometry. TEM observation indicates a mean grain size of ~25 nm. No magnetic properties were measured for this greigite sample.

Chen et al. (2005) proposed a simple solution-based route to synthesize greigite, in which $FeSO_4{\cdot}7H_2O$ or $FeCl_3{\cdot}6H_2O$ is reacted with thioacetamide (C_2H_5NS) at 100°C for 12 hours. After autoclaving, the solution is naturally cooled to room temperature. TEM observation indicates that the precipitate consists of tens of nanometres wide acicular or irregular greigite grains with mean size of 100 nm depending on the starting materials. The M_s for these synthetic greigite samples is up to 38.5 Am^2kg^{-1}, which indicates reasonably high purity. Hysteresis measurements for the synthetic greigite samples produced using $FeSO_4 \cdot 7H_2O$ as the starting material indicate a nearly ideal SD assemblage with magnetocrystalline anisotropy: B_c = ~120 mT, and M_{rs}/M_s = ~0.8. Reduced B_c and M_{rs}/M_s values were observed for synthetic greigite samples produced using $FeCl_3 \cdot 6H_2O$ as the starting material, which is probably caused by SP effects.

He et al. (2006) proposed a modified hydrothermal approach to synthesize greigite either by an *in situ* magnetic-field-assisted hydrothermal route or in the absence of a magnetic field, where ammonium iron sulphate hexahydrate is reacted with a sulphur precursor cysteine ($C_3H_7NO_2S$) at 150°C-160°C for 24 hours. Application of the external magnetic field has an effect on the morphology of the synthetic greigite grains. Applying a 45 mT magnetic field at the inert bottom of the reaction vessel produces pearl-chain-like microrods with diameters of 5.5-6 μm and lengths of 75-200 μm. Each microrod is composed of branched plates of greigite crystals. In contrast, in the absence of a magnetic field, equi-dimensional greigite crystals are produced with diameters of a few μm. XRD analysis indicates that the precipitate is single-phase greigite. The room-temperature M_s value for this greigite sample is 44.7 Am^2kg^{-1}, which indicates reasonably high purity. B_c for the greigite microrods is up to 40 mT, which probably indicates dominant SD grains but probably with a small contribution from PSD/MD grains.

The main synthetic greigite samples used in this study were produced using the new hydrothermal method proposed by Tang et al. (2007). In a typical hydrothermal procedure, $FeCl_3$ is reacted with CH_4N_2S in the presence of HCOOH in an autoclave at 170°C for 8 hours. The details of the procedure are described in Chapter 5. The hydrothermal process is kept in the autoclave, therefore it is difficult to sample intermediate products and monitor the reaction process. The present discussion focuses on formation of greigite in this process. In the hydrothermal process, CH_4N_2S provides the sulphur source because it can decompose in water and can produce H_2S (H_2S can be smelt during the synthesis). H_2S and Fe^{3+} then undergo a redox reaction. This process produces Fe^{2+} and elemental S:

$$H_2S + 2Fe^{3+} \rightarrow 2Fe^{2+} + S + H_2.$$

Elemental S is found when opening the autoclave after reacting for 6 hours. The Fe^{2+}, Fe^{3+} and H_2S in the solution then react to form greigite:

$$Fe^{2+} + 2Fe^{3+} + 4H_2S \rightarrow Fe_3S_4 + 4H_2.$$

Richard and Luther (2007) argued that greigite had not been reported to form directly from solution. All greigite syntheses are argued to involve the precursor mackinawite, which is metastable with respect to greigite (Berner, 1967; Lennie et al., 1997). However, it is not clear whether this hydrothermal process involves any iron sulphide precursors to greigite. Greigite is metastable and it is therefore not the final product in this hydrothermal process. For longer reaction times, greigite will react with S or H_2S to produce marcasite (Tang et al., 2007):

$$Fe_3S_4 + 2S \rightarrow 3FeS_2, \text{ or}$$

$$Fe_3S_4 + 2H_2S \rightarrow 3FeS_2 + 2H_2.$$

In these processes, S and H_2S are oxidants and two-thirds of the Fe^{3+} in greigite is reduced to Fe^{2+}. It is therefore important to control the reaction time in order to obtain pure greigite samples. HCOOH is not involved in the chemical process of greigite formation. However, HCOOH is important for producing pure greigite samples because it controls the acidity of the hydrothermal solution. The final product will be FeS_2 rather than Fe_3S_4 without HCOOH. Sample purity has been confirmed by a range of analyses including XRD, neutron diffraction, Mössbauer spectroscopy, and magnetic measurements. The greigite samples produced with this hydrothermal method represent the purest greigite yet produced.

In addition to these highly pure synthetic greigite samples, other less pure fine-grained greigite samples were also produced for this study. These greigite samples represent the end-member of magnetic domain states. Greigite is the only detected magnetic phase within the samples. These synthetic greigite samples were produced by solid state transformation of mackinawite to pyrite via the intermediate greigite (e.g., Lennie et al., 1997; Benning et al., 2000; Hunger and Benning, 2007). These samples contain substantial fine greigite particles that are dominated by SP properties at room temperature (Roberts et al., 2006). Details about the procedure and sample characterizations are described by Hunger and Benning (2007). Only a brief description of the method is given here. All open solutions and solids were manipulated in an anaerobic chamber with a hydrogen/nitrogen gas mixture (5%/95%). All reagents were prepared from analytical purity chemicals and deionized water (≥18 MΩ), which had been boiled for 30 minutes and purged with oxygen-free nitrogen gas when cooling. For the greigite synthesis, a nanocrystalline iron monosulphide precipitate was first prepared at 25°C in a 500 ml sealed glass reaction vessel using the methods described by Benning et al. (2000). A 0.1 M deoxygenated solution of Mohr's salt with a pH of 3.6 was then saturated with H_2S gas. By raising the pH of the solution to 6.5 via addition of a degassed 1.0 N NaOH solution, the iron was quantitatively precipitated as iron monosulphide. The vessel was then transferred to the anaerobic chamber and concentrated by settling and decanting. Polysulphide solutions containing fine greigite particles were synthesized using a modified standard procedure (Petre and Larachi, 2006). Weighed amounts of elemental sulphur that was dissolved in a degassed 1.0 N NaOH solution that had been saturated with pure H_2S gas and ~1.25 mmol FeS suspension were mixed and transferred into 3.5 ml silica ampoules. FeS was transformed to pyrite via greigite at certain temperatures (70°C and 90°C) over various time intervals (from 4 to 112 hours). The transformations were quickly stopped by quenching the silica ampoules into liquid nitrogen and were stored in a refrigerator at -88°C prior to analysis.

Appendix B

X-ray magnetic circular dichroism spectra for greigite

The XMCD technique was used to investigate the magnetic and electronic structure of greigite. XAS and XMCD spectra for both synthetic and natural greigite samples were recorded at the iron $L_{2,3}$ edge using circularly polarized synchrotron radiation at the Daresbury Laboratory (Fig. A1). The spectra are consistently different compared to magnetite (Fig. A2). Unlike magnetite, which has three components that correspond to the octahedral Fe^{2+}, the octahedral Fe^{3+}, and the tetrahedral Fe^{3+} in the XMCD spectrum, the XMCD spectrum for greigite has only two components associated with the octahedral Fe^{2+} and the octahedral Fe^{3+}. The missing peak for the tetrahedral Fe site in the measured XMCD spectrum of greigite (Fig. A1) might be caused by the low resolution of the energy spectrum, i.e., the three peaks are too close

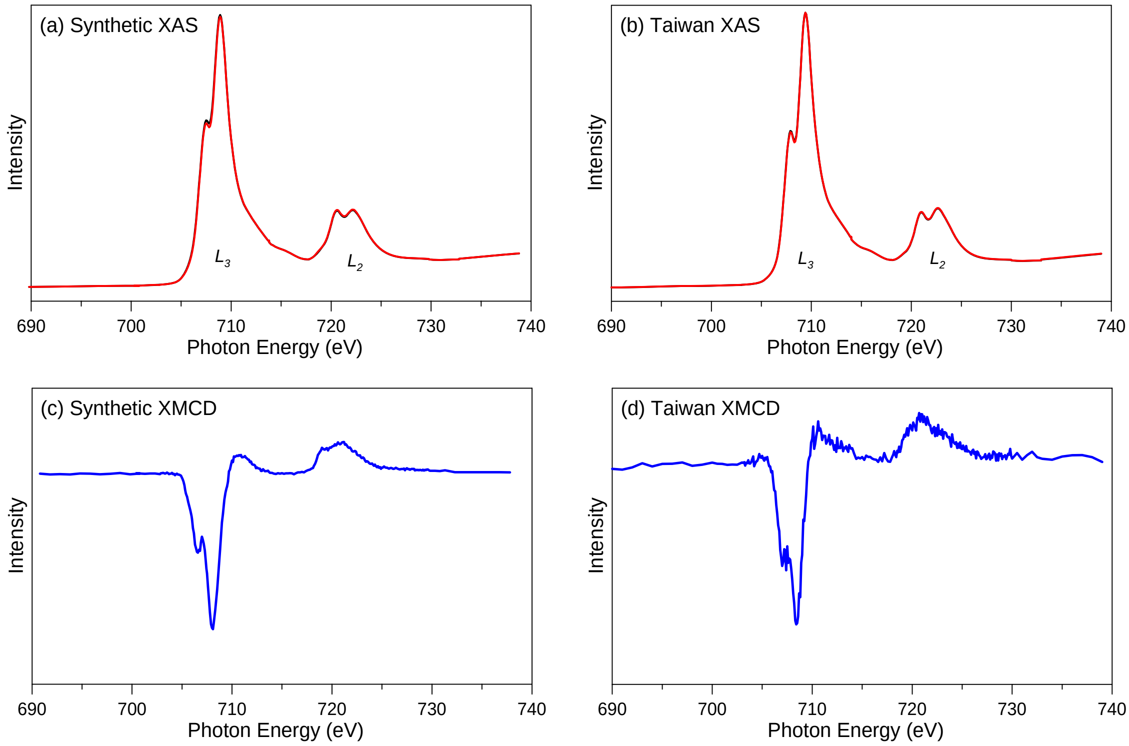

Figure A1. (a, b) XAS spectra at the iron $L_{2,3}$ edge using synchrotron radiation source for a pure synthetic greigite sample and a natural greigite sample from Taiwan. XAS spectra are the absorption curves measured with the magnetic field parallel (ρ_+) and antiparallel (ρ_-) to the X-ray beam. The positions of the L_2 and L_3 absorption peaks are labelled. (c, d) the corresponding XMCD spectra ($\rho_+ - \rho_-$). XMCD spectra were measured by reversing the sample magnetization at each point in the scans using an eight-pole vector magnet. A 0.6 T magnetic field was applied along the beam direction. All spectra were measured at room temperature.

to exhibit all features. To test this possibility, XMCD spectra were measured for the same greigite samples using the powerful synchrotron radiation source at the Advanced Light Source (ALS) at the Lawrence Berkeley National Laboratory in California, USA. Similar XMCD patterns were obtained as those shown in Figure A1, which rules out the possibility of energy resolution problems and confirms the fundamental difference in the electronic structure between greigite and magnetite. Letard et al. (2005) attributed the different XMCD spectra between greigite and magnetite to the possible presence of vacancies in greigite. However, Rietveld profile analysis of the neutron diffraction pattern for a pure synthetic greigite sample indicates that greigite does not have a

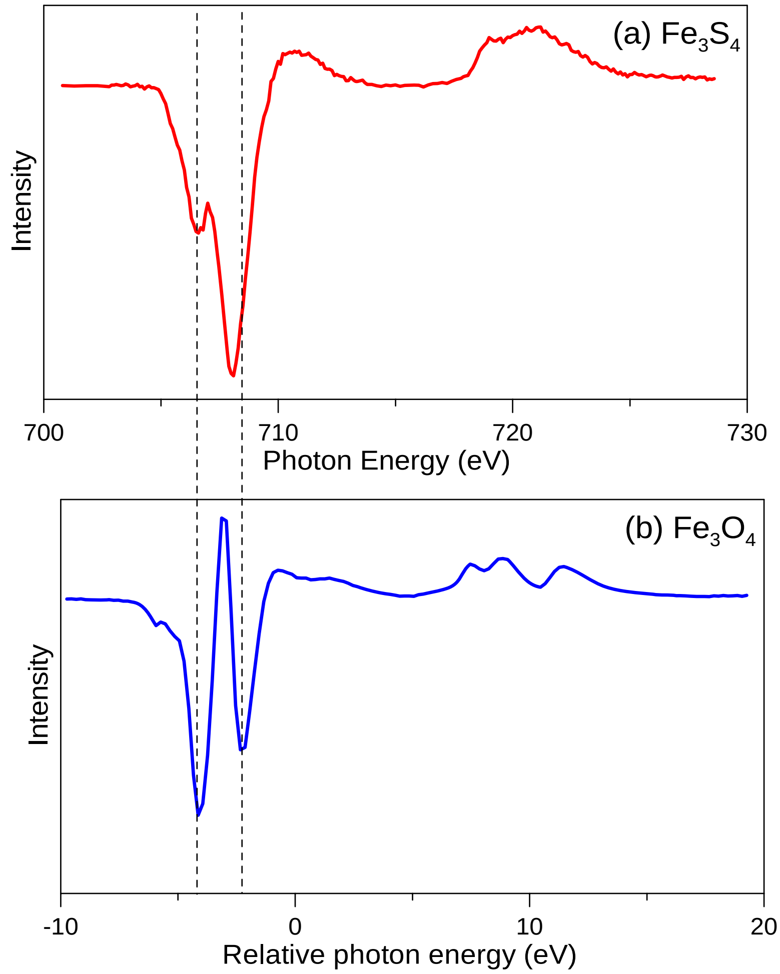

Figure A2. Comparison of XMCD spectra between (a) greigite and (b) magnetite. The reduced separation of energy between the peaks for octahedral Fe^{2+} and Fe^{3+} sites confirms an increased degree of covalency between iron and sulphur compared to oxygen ligands. The XMCD data for magnetite were kindly provided by Gerrit van der Laan.

significant vacancy concentration (Chapter 6). Qian et al. (1999) determined the composition of the greigite produced by the employed hydrothermal synthesis method to be nearly stoichiometric ($Fe_{2.994}S_4$). This indicates that the electronic structure of greigite is different to that of magnetite, e.g., cation distribution and valence states of iron. Comparison of XMCD spectra for greigite and magnetite indicates a reduced energy separation between the Fe^{2+} and Fe^{3+} peaks in greigite compared to magnetite (Fig. A2). This indicates an increased covalency of Fe_3S_4 compared to the more ionic Fe_3O_4. Increased covalency reduces the ionicity of the ions, which makes the ligands (O or S) less negative and the Fe cations less positive. For illustration, a charge distribution of $[Fe^{2+}, Fe^{3+}]_B(Fe^{3+})_A$ with a total magnetic moment of $5\ \mu_B - 5\ \mu_B + 4\ \mu_B = 4\ \mu_B$ is representative for Fe_3O_4, while $[Fe^{1+}, Fe^{2+}]_B(Fe^{2+})_A$ with a total magnetic moment of $3\ \mu_B - 4\ \mu_B + 4\ \mu_B = 3\ \mu_B$ could be representative of Fe_3S_4. In reality, the charges will not necessarily be integers and it is difficult to determine the precise *d*-count of each cation. Nevertheless, XMCD analysis confirms an increase in covalency in greigite compared to magnetite. This is consistent with the observed lower magnetic moment in greigite compared to magnetite (Chapter 6). One possible explanation for the XMCD spectrum of greigite is that the tetrahedral peak is shifted closer to the energy position of the Fe^{2+} octahedral peak (Fig. A3) (Prof. Gerrit van der Laan, personal communication, 2008). The relative positions of the two negative peaks (the Fe^{2+} and Fe^{3+} *B* sites) and the positive peak (the Fe^{3+} *A* site) can be different in energy for Fe_3S_4 and Fe_3O_4 because of differences in electronegativity, covalency, crystal field strength, etc. The energy position is largely driven by the charge of the ions (more precisely, it is the number of *d* electrons, i.e., the *d*-count). The *d*-counts on the different sites are not expected to be integer values. Chen et al. (2004) argued that the *d*-counts in magnetite are octahedral Fe^{2+} = 6.15, tetrahedral Fe^{3+} = 5.30, and octahedral Fe^{3+} = 5.47. There is only a difference of 0.68 electrons between Fe^{2+} and Fe^{3+}. This indicates the possibility that the *d*-count of the Fe^{3+} tetrahedral site in greigite can be shifted closer to that of the Fe^{2+} octahedral site. The tetrahedral peak will shift down in energy compared to both tetrahedral peaks, which could mean that the tetrahedral site becomes less positive relative to the octahedral sites. Consequently, this suggests that the covalency is stronger for the tetrahedral site than for the octahedral sites. This approximately explains the observed XMCD spectra for greigite. Nevertheless, future work, such as band structure calculations and experiments, is necessary to test this explanation and to definitely resolve the electronic structure of greigite.

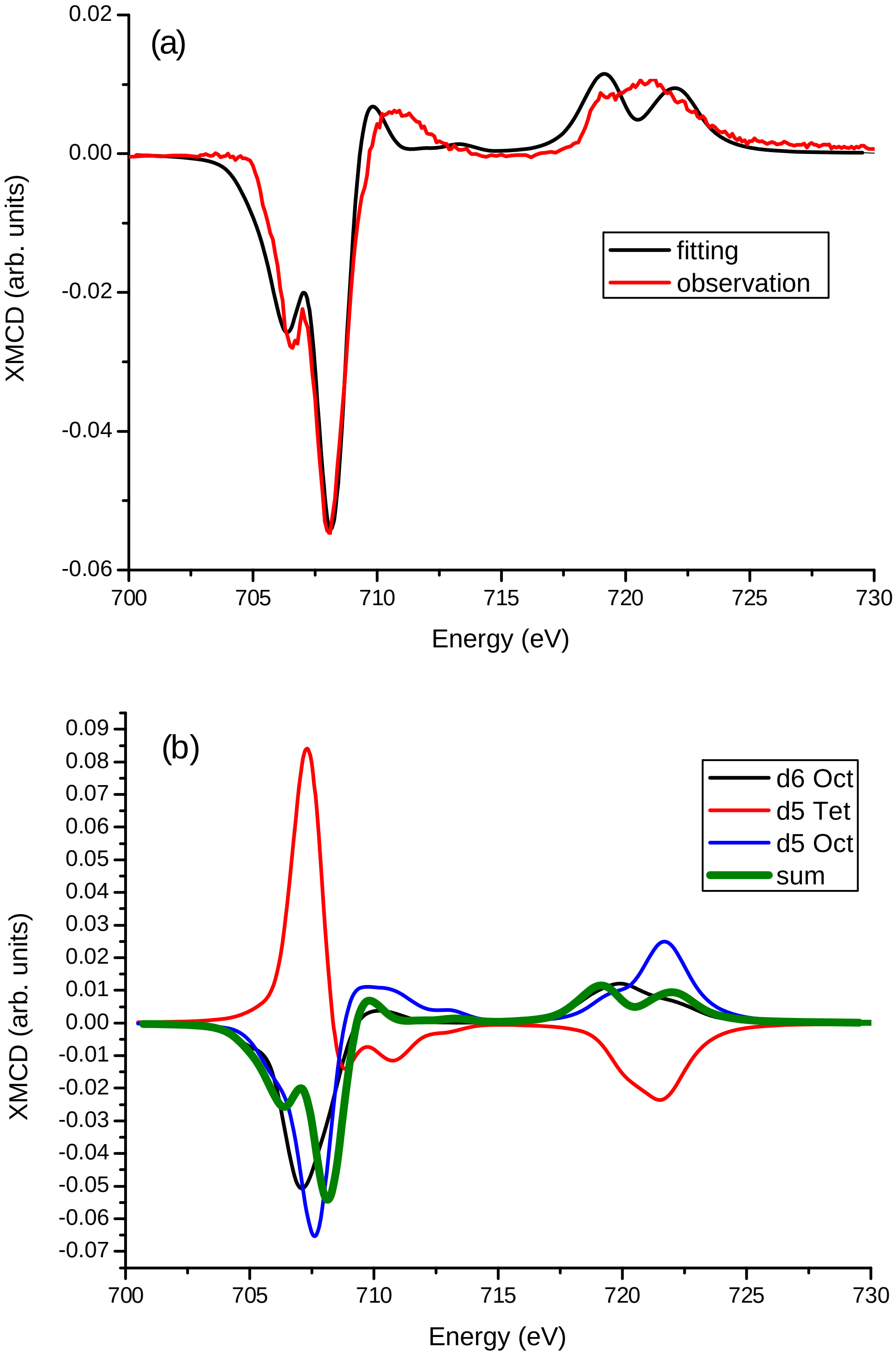

Figure A3. (a) Measured XMCD spectrum of the synthetic greigite sample (red curve) and the calculated best fit (black curve). (b) Calculated XMCD components for each Fe site. The measured XMCD spectra were fitted using a nonlinear least squares method. The calculated XMCD curves for each Fe site used in the fitting were first convoluted by a Gaussian to account for experimental broadening of peaks.

References

Andersen, A. F. (1968), A neutron diffraction investigation of Fe_3Se_4, *Acta. Chem. Scand.*, *22*, 827-835.

Aragón, R. (1992), Magnetization and exchange in nonstoichiometric magnetite, *Phys. Rev. B*, *46*, 5328-5333.

Babinszki, E., E. Marton, P. Marton, and L. F. Kiss (2007), Widespread occurrence of greigite in the sediments of Lake Pannon: Implications for environment and magnetostratigraphy, *Palaeogeogr. Palaeoclimatol. Palaeoecol.*, *252*, 626-636.

Bacon, G. E. (1975), *Neutron Diffraction*, 3rd ed., Clarendon Press, Oxford, 636 pp.

Bazylinski, D. A., B. R. Heywood, S. Mann, and R. B. Frankel (1993), Fe_3O_4 and Fe_3S_4 in a bacterium, *Nature*, *366*, 218.

Bazylinski, D. A., R. B. Frankel, B. R. Heywood, S. Mann, J. W. King, P. L. Donaghay, and A. K. Hanson (1995), Controlled biomineralization of magnetite (Fe_3O_4) and greigite (Fe_3S_4) in a magnetotactic bacterium, *Appl. Env. Microbiol.*, *61*, 3232-3239.

Benning, L. G., R. T. Wilkin, and H. L. Barnes (2000), Reaction pathways in the Fe-S system below 100°C, *Chem. Geol.*, *167*, 25-51.

Berner, R. A. (1984), Sedimentary pyrite formation: An update, *Geochim. Cosmochim. Acta*, *48*, 605-615.

Bracci, G., D. Dalena, and P. Orlandi (1985), La greigite di Mentana, Lazio, *Rend. Soc. Ital. Mineral. Petrol.*, *40*, 295-298.

Braga, M., S. K. Lie, C. A. Taft, and W. A. Lester, Jr. (1988), Electronic structure, hyperfine interactions, and magnetic properties for iron octahedral sulfides, *Phys. Rev.*, *38*, 10837-10851.

Brockhouse, B. N., and H. Watanabe (1963), Spin waves in magnetite from neutron scattering, in *Inelastic Scattering of Neutrons in Solids and Liquids*, vol. 2, 297-308, International Atomic Energy Agency Proceedings, Vienna.

Brown, P. J., and J. B. Forsyth (1964), The determination of beam polarization and flipping efficiency in polarized neutron diffractometry, *Brit. J. Appl. Phys.*, *15*, 1529-1533.

Butler, R. F. (1992), *Paleomagnetism: Magnetic domains to geologic terrances*, Blackwell Scientific Publications, 238 pp.

Canfield, D. E., and R. A. Berner (1987), Dissolution and pyritization of magnetite in anoxic marine sediments, *Geochim. Cosmochim. Acta*, *51*, 645-659.

Canfield, D. E., R. Raiswell, S. H. Bottrell (1992), The reactivity of sedimentary iron minerals toward sulfide, *Am. J. Sci.*, *292*, 659-683.

Carvallo, C., and A. R. Muxworthy (2006), Low-temperature first-order reversal curve (FORC) diagrams for synthetic and natural samples, *Geochem. Geophys. Geosyst.*, *7*, Q09003, doi:10.1029/2006GC001299.

Chadwick, J. (1932), Possible existence of a neutron, *Nature*, *129*, 312-312.

Chang, L., A. P. Roberts, A. R. Muxworthy, Y. Tang, Q. Chen, C. J. Rowan, Q. Liu and P. Pruner (2007), Magnetic characteristics of synthetic pseudo-single-domain and multi-domain greigite (Fe_3S_4), *Geophys. Res. Lett.*, *34*, L24304, doi:10.1029/2007GL032114.

Chang, L., A. P. Roberts, Y. Tang, B. D. Rainford, A. R. Muxworthy, and Q. Chen (2008), Fundamental magnetic parameters from pure synthetic greigite (Fe_3S_4), *J. Geophys. Res.*, *113*, B06104, doi:10.1029/2007JB005502.

Chang, L., A. P. Roberts, C. J. Rowan, Y. Tang, P. Pruner, Q. Chen, and C-S. Horng (2009), Low-temperature magnetic properties of greigite (Fe_3S_4), *Geochem., Geophys., Geosyst.*, *10*, Q01Y04, doi:10.1029/2008GC002276.

Chen, J., D. J. Huang, A. Tanaka, C. F. Chang, S. C. Chung, W. B. Wu, and C. T. Chen (2004), Magnetic circular dichroism in Fe 2*p* resonant photoemission of magnetite, *Phys. Rev. B*, *69*, 085107.

Chen, X. Y., X. F. Zhang, J. X. Wan, Z. H. Wang, and Y. T. Qian (2005), Selective fabrication of metastable greigite (Fe_3S_4) nanocrystallites and its magnetic properties through a simple solution-based route, *Chem. Phys. Lett.*, *403*, 396-399.

Chikazumi, S. (1997), *Physics of Ferromagnetism*, second edition, Clarendon Press, Oxford, 670 pp.

Coey, J. M. D. (1971), Non-collinear spin arrangement in ultrafine ferrimagnetic crystallites, *Phys. Rev. Lett.*, *27*, 1140-1142.

Coey, J. M. D., M. R. Spender, and A. H. Morrish (1970), The magnetic structure of the spinel, Fe_3S_4, *Solid State Comm.*, *8*, 1605-1608.

Cracknell, A. P. (1975), *Magnetism in crystalline materials; applications of the theory of groups of cambiant symmetry*, Pergamon Press, Oxford, 276 pp.

Day, R., M. Fuller, and V. A. Schmidt (1977), Hysteresis properties of titanomagnetites: Grain size and composition dependence, *Phys. Earth Planet. Inter.*, *13*, 260-267.

Dekkers, M. J. (1989), Magnetic properties of natural pyrrhotite. II. High- and low-temperature behaviour of J_{rs} and TRM as function of grain size, *Phys. Earth Planet. Inter.*, *57,* 266-283.

Dekkers, M. J., and M. A. A. Schoonen (1996), Magnetic properties of hydrothermally synthesized greigite-I. Rock magnetic parameters at room temperature, *Geophys. J. Int.*, *126*, 360-368.

Dekkers, M. J., H. F. Passier, and M. A. A. Schoonen (2000), Magnetic properties of hydrothermally synthesized greigite-II. High- and low-temperature characteristics, *Geophys. J. Int.*, *141*, 809-819.

Diaz-Ricci, J. C., and J. L. Kirschvink (1992), Magnetic domain state and coercivity predictions for biogenic greigite (Fe_3S_4): A comparison of theory with magnetosome observations, *J. Geophys. Res.*, *97*, 17309-17315.

Dormann, J. L., D. Fiorani, and E. Tronc (1997), Magnetic relaxation in fine-particle systems, *Adv. Chem. Phys.*, vol. XCVIII, edited by I. Prigogine and S. A. Rice, pp. 283-494, John Wiley, Hoboken, N. J.

Doss, B. N. (1912a), Über die nature und zusammensetzung des Miocänen tonen der gouvernements Samara auftretenden Schwefeleisens, *Neues Jahrb. Mineral.*, *A33*, 662-713.

Doss, B. N. (1912b), Melnikowit, ein neues eisenbisulfid, und seine bedeutung für genesis der Kieslagerstätten, *Zeit. Prakt. Geol.*, *20*, 453-483.

Dunlop, D. J. (2002), Theory and application of the Day plot (M_{rs}/M_s versus H_{cr}/H_c): 1. Theoretical curves and tests using titanomagnetite data, *J. Geophys. Res.*, *107*, 2056, doi:10.1029/2001JB000486.

Dunlop, D. J., and Ö. Özdemir (1997), *Rock Magnetism: Fundamentals and Frontiers*, Cambridge, 573 pp.

Enkin, R. J., J. Baker, D. Nourgaliev, P. Iassonov, and T. S. Hamilton (2007), Magnetic hysteresis parameters and Day plot analysis to characterize diagenetic alteration in gas hydrate-bearing sediments, *J. Geophys. Res.*, *112*, B06S90, doi:10.1029/2006JB004638.

Fabian, K., Some additional parameters to estimate domain state from isothermal magnetization measurements, *Earth Planet. Sci. Lett.*, *213*, 337-345, 2003.

Farina, M., D. M. S. Esquivel, and H. G. P. Lins de Barros (1990), Magnetic iron-sulphur crystals from a magnetotactic microorganism, *Nature*, *343*, 256-258.

Fassbinder, J. W. E., and H. Stanjek (1994), Magnetic properties of biogenic soil greigite (Fe_3S_4), *Geophys. Res. Lett.*, *21*, 2349-2352.

Florindo, F., and F. Marra (1995), A revision of the stratigraphy for the Middle Pleistocene continental deposits of Rome (Central Italy): Palaeomagnetic data, *Ann. Geofis.*, *38*, 177-188.

Florindo, F., and L. Sagnotti (1995), Palaeomagnetism and rock magnetism in the upper Pliocene Valle Ricca (Rome, Italy) section, *Geophys. J. Int.*, *123*, 340-354.

Florindo, F., D. B. Karner, F. Marra, P. R. Renne, A. P. Roberts, and R. Weaver (2007), Radioisotopic age constraints for Glacial Terminations IX and VII from aggradational sections of the Tiber River delta in Rome, Italy, *Earth Planet. Sci. Lett.*, *256*, 61-80.

Frank, U., N. R. Nowaczyk, and J. F. W. Negendank (2007), Palaeomagnetism of greigite bearing sediments from the Dead Sea, Israel, *Geophys. J. Int.*, *168*, 904-920.

Fu, Y., T. von Dobeneck, C. Franke, D. Heslop, and S. Kasten (2008), Rock magnetic identification and geochemical process models of greigite formation in Quaternary marine sediments from the Gulf of Mexico (IODP Hole U1319A), *Earth Planet. Sci. Lett.*, *275*, 233-245.

García, J, and G. Subías (2004), The Verwey transition – a new perspective, *J. Phys.: Condens. Matter*, *16*, R145-R178.

Gonser, U. (1975), *Mössbauer Spectroscopy*, Springer-Verlag, Berlin, 240 pp.

Goodenough, J. B. (1978), Structure chemistry of iron sulfides, *Mat. Res. Bull.*, *13*, 1305-1314.

Goodenough, J. B., and G. A. Fatseas (1982), Mössbauer ^{57}Fe isomer shift as a measure of valence in mixed-valence iron sulfides, *J. Solid State Chem.*, *41*, 1-22.

Greenwood, N. N., and T. C. Gibb (1971), *Mössbauer Spectroscopy*, Chapman and Hall Ltd, London, 659 pp.

Han, W., and M. Gao (2008), Investigations on iron sulfide nanosheets prepared via a single-source precursor approach, *Cryst. Growth Des.*, *8*, 1023-1030.

Harrison, R. J., and J. M. Feinberg (2008), FORCinel: An improved algorithm for calculating first-order reversal curve distributions using locally weighted regression smoothing, *Geochem. Geophys. Geosyst.*, *9*, Q05016, doi:10.1029/2008GC001987.

He, Z. B., S. H. Yu, X. Y. Zhou, X. G. Li, and J. F. Qu (2006), Magnetic-field-induced phase-selective synthesis of ferrosulfide microrods by a hydrothermal process: Microstructure control and magnetic properties, *Adv. Funct. Mater.*, *16*, 1105-1111.

Heywood, B. R., S. Mann, and R. B. Frankel (1991), Structure, morphology and growth of biogenic greigite, *Mater. Res. Soc. Symp. Proc.*, *218*, 93-108.

Hilton, J. (1990), Greigite and the magnetic properties of sediments, *Limnol. Oceanogr.*, *35*, 509-520.

Hippert, F., E. Geissler, J. L. Hodeau, E. Lelièvre-Berna, J. -R Regnard (2006), *Neutron and X-ray Spectroscopy*, Springer, 566 pp.

Hoffmann, V. (1992), Greigite (Fe_3S_4): Magnetic properties and first domain observations, *Phys. Earth Planet. Inter.*, *70*, 288-301.

Horiuchi, S., H. Wada, and T. Moori (1974), Morphology and imperfection of hydrothermally synthesized greigite (Fe_3S_4), *J. Cryst. Growth*, *24/25*, 624-626.

Horng, C. S., J. C. Chen, and T. Q. Lee (1992a), Variations in magnetic minerals from two Plio-Pleistocene marine-deposited sections, southwestern Taiwan, *J. Geol. Soc. China*, *35*, 323-335.

Horng, C. S., C. Laj, T. Q. Lee, and J. C. Chen (1992b), Magnetic characteristics of sedimentary rocks from the Tsengwen-chi and Erhjen-chi sections in southwestern Taiwan, *Bull. Inst. Earth Sci., Acad. Sin.*, *12*, 27-32.

Horng, C. S., M. Torii, K. S. Shea, and S. J. Kao (1998), Inconsistent magnetic polarities between greigite- and pyrrhotite/magnetite-bearing marine sediments from the Tsailiao-chi section, southwestern Taiwan, *Earth Planet. Sci. Lett.*, *164*, 467-481.

Housen, B. A., and R. J. Musgrave (1996), Rock-magnetic signature of gas hydrates in accretionary prism sediments, *Earth Planet. Sci. Lett.*, *139*, 509-519.

Hunger, S., and L. G. Benning (2007), Greigite: A true intermediate on the polysulfide pathway to pyrite, *Geochem. Trans.*, *8*, doi:10.1186/1467-4866-8-1.

Jelinowska, A., P. Tucholka, F. Gasse, and J. C. Fontes (1995), Mineral magnetic record of environment in Late Pleistocene and Holocene sediments, Lake Manas, Xinjiang, China, *Geophys. Res. Lett.*, *8*, 953-956.

Jelinowska, A., P. Tucholka, F. Guichard, I. Lefèvre, D. Badaut-Trauth, F. Chalié, F. Gasse, N. Tribovillard, and A. Desprairies (1998), Mineral magnetic study of Late Quaternary South Caspian Sea sediments: Palaeoenvironmental implications, *Geophys. J. Int.*, *133*, 499-509.

Jiang, W. T., C. S. Horng, A. P. Roberts, and D. R. Peacor (2001), Contradictory magnetic polarities in sediments and variable timing of neoformation of authigenic greigite, *Earth Planet. Sci. Lett.*, *193*, 1-12.

Kao, S. J., C. S. Horng, A. P. Roberts, and K. K. Liu (2004), Carbon-sulfur-iron relationships in sedimentary rocks from southwestern Taiwan: Influence of geochemical environments on greigite and pyrrhotite formation, *Chem. Geol.*, *203*, 153-168.

Kasama, T., M. Pósfai, R. K. K. Chong, A. P. Finlayson, P. R. Buseck, R. E. Dunin-Borkowski, and R. B. Frankel (2006a), Magnetic microstructure of iron sulfide crystals in magnetotactic bacteria from off-axis electron holography, *Physica B*, *384*, 249-252.

Kasama, T., M. Pósfai, R. K. K. Chong, A. P. Finlayson, P. R. Buseck, R. B. Frankel, and R. E. Dunin-Borkowski (2006b), Magnetic properties, microstructure, composition, and morphology of greigite nanocrystals in magnetotactic bacteria from electron holography and tomography, *Am. Mineral.*, *91*, 1216-1229.

Keffer, F. (1966), Ferromagnetism, in *Encyclopedia of Physics*, edited by H. P. J. Wijin (Springer-Verlag, Berlin), Vol. XVIII-2, 273 pp.

Kenan, R. P., M. L. Glasser, and F. J. Milford (1963), Spin-wave contribution to the heat capacity of magnetite, *Phys. Rev.*, *132*, 47-49.

Kittel, C. (1946), Theory of the structure of ferromagnetic domains in films and small particles, *Phys. Rev.*, *70*, 965-971.

Kittel, C. (1949), Physical theory of ferromagnetic domains, *Rev. Mod. Phys.*, *21*, 541-583.

Klotz, S., G. Rousse, Th. Strässle, C. L. Bull, and M. Guthrie (2006), Nuclear and magnetic structure of magnetite under pressure to 5.3 GPa and low temperatures to 130 K by neutron scattering, *Phys. Rev. B*, 74, 012410.

Kopp, R. E., C. Z. Nash, A. Kobayashi, B. P. Weiss, D. A. Bazylinski, and J. L. Kirschvink (2006), Ferromagnetic resonance spectroscopy for assessment of magnetic anisotropy and magnetostatic interactions: A case study of mutant magnetotactic bacteria, *J. Geophys. Res.*, *111*, B12S25, doi:10.1029/2006JB004529.

Kronmüller, H, and M. Fähnle (2003), *Micromagnetism and the Microstructure of Ferromagnetic Solids*, Cambridge, 448 pp.

Krs, M., M. Krsová, P. Pruner, A. Zeman, F. Novák, and J. Jansa (1990), A petromagnetic study of Miocene rocks bearing micro-organic material and the magnetic mineral greigite (Sokolov and Cheb basins, Czechoslovakia), *Phys. Earth Planet. Inter.*, *63*, 98-112.

Krs, M., F. Novák, M. Krsová, P. Pruner, L. Koulíková, and J. Jansa (1992), Magnetic properties and metastability of greigite-smythite mineralization in brown-coal basins of the Krusné Hory Piedmont, Bohemia, *Phys. Earth Planet. Inter.*, *70*, 273-287.

Kodama, R. H., A. E. Berkowitz, E. J. McNiff, Jr., and S. Foner (1996), Surface spin disorder in $NiFe_2O_4$ nanoparticles, *Phys. Rev. Lett.*, *77*, 00628.

Kouvel, J. S. (1956), Specific heat of a magnetite crystal at liquid helium temperatures, *Phys. Rev.*, *102*, 1489-1490.

Landau, L., and E. Lifshitz (1935), On the theory of the dispersion of magnetic permeability in ferromagnetic bodies, *Physik. Zeits. Sowjetunion*, *8*, 153-169.

Larrasoaña, J. C., A. P. Roberts, R. J. Musgrave, E. Gràcia, E. Piñero, M. Vega, and F. Martínez-Ruiz (2007), Diagenetic formation of greigite and pyrrhotite in marine sedimentary systems containing gas hydrates, *Earth Planet. Sci. Lett*, *261*, 350-366.

Lein, A. Y., G. A. Sidorenko, I. I. Volkov, and A. Y. Shevchenko (1978), Diagenetic mackinawite, melnikovite (greigite) and pyrite in sediments of the trans-Pacific profile and the Gulf of California, *Dok. Akad. Nauk SSSR*, *238*, 698-700.

Lennie, A. R, S. A. T. Redfern, P. E. Champness, C. P. Stoddart, P. F. Schofield, and D. J. Vaughan (1997), Transformation of mackinawite to greigite: An in situ X-ray powder diffraction and transmission electron microscope study, *Am. Mineral.*, 82, 302-309.

Lepp, H. (1957), The synthesis and probable geologic significance of melnikovite, *Econ. Geol.*, *52*, 528-535, 1957.

Letard, I., Ph. Sainctavit, N. Menguy, J.-P. Valet, A. Isambert, M. Dekkers, and A. Gloter (2005), Mineralogy of greigite Fe_3S_4, *Phys. Scrip.*, *T115*, 489-491.

Lins, U., C. N. Keim, F. F. Evans, M. Farina, P. R. Buseck (2007), Magnetite and greigite crystals in multicellular magnetotactic prokaryotes, *Geomicrobiol. J.*, *24*, 43-50, doi:10.1080/01490450601134317.

Liu, J., R. X. Zhu, A. P. Roberts, S. Q. Li, and J. H. Chang (2004), High-resolution analysis of early diagenetic effects on magnetic minerals in post-middle-Holocene continental shelf sediments from the Korea Strait, *J. Geophys. Res.*, *109*, B03130, doi:10.1029/2003JB002813.

Mann, S., N. H. C. Sparks, R. B. Frankel, D. A. Bazylinski, and H. W. Jannasch (1990), Biomineralization of ferrimagnetic greigite (Fe_3S_4) and iron pyrite (FeS_2) in a magnetotactic bacterium, *Nature*, *343*, 258-261.

Manning, P. G., J. D. H. Williams, M. N. Charlton, L. A. Ash, and T. Birchall (1979), Mössbauer spectral studies of the diagenesis of iron in a sulphide-rich sediment core, *Nature*, *280*, 134-136.

Markov, G. P., V. P. Shcherbakov, A. S. Bolshakov, and Y. K. Vinogradov (1983), On the temperature-dependence of partial thermoremanent magnetization in multidomain grains, *Izv. Akad Nauk SSSR Fiz. Zemli*, *19*, 625-630.

Martín-Hernández, F., I. M. Bominaar-Silkens, M. J. Dekkers, and J. K. Maan (2006). High-field cantilever magnetometry as a tool for the determination of the magnetocrystalline anisotropy of single crystals, *Tectonophysics*, 418, 21-30.

Mattei, M., C. Kissel, and R. Funiciello (1996), No tectonic rotation of the Tuscan Tyrrhenian margin (Italy) since late Messinian, *J. Geophys. Res., 101*, 2835-2845.

Mattis, D. C. (1981), *The Theory of Magnetism I: Statics and dynamics,* Springer-Verlag, New York, 300 pp.

Mayergoyz, I. D. (1986), Mathematical models of hysteresis, *Phys. Rev. Lett.*, *56*, 1518-1561.

Moon, R. M., T. Riste, and W. C. Koehler (1969), Polarization analysis of thermal-neutron scattering, *Phys. Rev.*, *181*, 920-931.

Morice, J. A., L. V. C. Rees, and D. T. Rickard (1969), Mössbauer studies of iron sulphides, *J. Inorg. Nucl. Chem.*, *31*, 3797-3802.

Moskowitz, B. M. (1991), *Hitchhiker's Guide to Magnetism*, Institute for Rock Magnetism, University of Minnesota (source: http://www.irm.umn.edu/hg2m/hg2m_index.html).

Moskowitz, B. M. (1993), High-temperature magnetostriction of magnetite and titanomagnetite, *J. Geophys. Res.*, *98*, 359-371.

Moskowitz, B. M., R. B. Frankel, and D. A. Bazylinski (1993), Rock magnetic criteria for the detection of biogenic magnetite, *Earth Planet. Sci. Lett.*, *120*, 283-300.

Moskowitz, B. M., M. Jackson and C. Kissel (1998), Low-temperature magnetic behavior of titanomagnetites, *Earth Planet. Sci. Lett.*, *157*, 141-149.

Muxworthy, A. R., and D. J. Dunlop (2002), First-order reversal curve (FORC) diagrams for pseudo-single-domain magnetites at high temperature, *Earth Planet. Sci. Lett.*, *203*, 369-382.

Muxworthy, A. R., D. J. Dunlop, and W. Williams (2003), High-temperature magnetic stability of small magnetite particles, *J. Geophys. Res.*, *108*, 2281, doi:2210.1029/2002JB002195.

Nagata, T. (1961), *Rock Magnetism*, 2en ed., Maruzen, Tokyo, 350 pp.

Nakazawa, H., and K. Sakaguchi (1972), Anhydrous synthesis of greigite, *Mineral. J.*, *6*, 458-463.

Nakazawa, H., T. Osaka, and K. Sakaguchi (1973), Preparation of thin films of greigite, Fe_3S_4, and its preferred orientation on a sodium chloride crystal, *Am. Mineral.*, *58*, 926-929.

Néel, L. (1948), Propriétés magnétiques des ferrites: Ferrimagnétisme et antiferromagnétisme, *Ann. Phys.*, *3*, 137-198.

Néel, L. (1949), Théorie du traînage magnétique des ferromagnétiques en grains fins avec applications aux terres cuites, *Ann. Géophys.*, *5*, 99-136.

Opdyke, N. D., and J. E. T. Channell (1996), *Magnetic Stratigraphy*, Academic Press, San Diego, 346 pp.

O'Reilly, W. (1984), *Rock and Mineral Magnetism*, Chapman and Hall, London, 220 pp.

Pearce, C. I., R. A. D. Pattrick, and D. J. Vaughan (2006), Electrical and magnetic properties of sulfides, *Rev. Mineral. Geochem.*, *61*, 127-180.

Petre C. F., and F. Larachi (2006), Capillary electrophoretic separation of inorganic sulfur-sulfide, Polysulfides, and sulfur-oxygen species, *J. Separation Sci.*, *29,* 144-152.

Petrova, G. N., and V. I. Trukhin (1961), Spontaneous changes in H_c of particular cycles of magnetization observed during cooling of ferromagnetic minerals, *Izv., Phys. Solid Earth*, *6*, 584-588.

Pike, C. R. (2003), First-order reversal-curve diagrams and reversible magnetization, *Phys. Rev. B*, 104424.

Pike, C. R., A. P. Roberts, and K. L. Verosub (1999), Characterizing interactions in fine magnetic particle systems using first order reversal curves, *J. Appl. Phys.*, *85*, 6660-6667.

Pike, C. R., A. P. Roberts, and K. L. Verosub (2001a), First-order reversal curve diagrams and thermal relaxation effects in magnetic particles, *Geophys. J. Int.*, *145*, 721-730.

Pike, C. R., A. P. Roberts, M. J. Dekkers, and K. L. Verosub (2001b), An investigation of multi-domain hysteresis mechanisms using FORC diagrams, *Phys. Earth Planet. Inter.*, *126*, 11-25.

Pósfai, M., P. R. Buseck, D. A. Bazylinski, and R. B. Frankel (1998a), Iron sulfides from magnetotactic bacteria: Structure, composition, and phase transitions, *Am. Mineral.*, *83*, 1469-1481.

Pósfai, M., P. R. Buseck, D. A. Bazylinski, and R. B. Frankel (1998b), Reaction sequence of iron sulfide minerals in bacteria and their use as biomarkers, *Science, 280*, 880-883.

Pye K. (1981), Marshrock formed by iron sulphide and siderite cementation in saltmarsh sediments, *Nature*, *294*, 650-652.

Qian, X. F., X. M. Zhang, C. Wang, Y. Xie, W. Z. Wang, and Y. T. Qian (1999), The preparation and phase transition of nanocrystalline iron sulfides via toluene-thermal process, *Mater. Sci. Eng.*, *64*, 170-173.

Radusinović, D. (1966), Greigite from the Lojane chromium deposit, Macedonia, *Am. Mineral.*, *51*, 209-215.

Raiswell, R. (1997), A geochemical framework for the application of stable sulphur isotopes to fossil pyritization, *J. Geol. Soc. (Lond.)*, *154*, 3169-3175.

Reynolds, R. L., M. L. Tuttle, C. A. Rice, N. S. Fishman, J. A. Karachewski, and D. M. Sherman (1994), Magnetization and geochemistry of greigite-bearing Cretaceous strata, North Slope Basin, Alaska, *Am. J. Sci.*, *294*, 485-528.

Reynolds, R. L., J. G. Rosenbaum, P. van Metre, M. Tuttle, E. Callender, and A. Goldin (1999), Greigite () as an indicator of drought – The 1912-1994 sediment magnetic record from White Rock Lake, Dallas, Texas, USA, *J. Paleolimnol.*, *21*, 193-206.

Rickard, D., and G. W. Luther, III (2007), Chemistry of iron sulfides, *Chem. Rev.*, *107,* 514-562.

Roberts, A. P. (1995), Magnetic properties of sedimentary greigite (Fe_3S_4), *Earth Planet. Sci. Lett.*, *134*, 227-236.

Roberts, A. P., and G. M. Turner (1993), Diagenetic formation of ferrimagnetic iron sulphide minerals in rapidly deposited marine sediments, South Island, New Zealand, *Earth Planet. Sci. Lett.*, *115,* 257-273.

Roberts, A. P., and R. Weaver (2005), Multiple mechanisms of remagnetization involving sedimentary greigite (Fe_3S_4), *Earth Planet. Sci. Lett.*, *231*, 263-277.

Roberts, A. P., Y. L. Cui, and K. L. Verosub (1995), Wasp-waisted hysteresis loops: Mineral magnetic characteristics and discrimination of components in mixed magnetic systems, *J. Geophys. Res.*, *100*, 17909-17924.

Roberts, A. P., C. R. Pike, and K. L. Verosub (2000), FORC diagrams: A new tool for characterizing the magnetic properties of natural samples, *J. Geophys. Res.*, *105*, 28461-28475.

Roberts, A. P., R. L. Reynolds, K. L. Verosub, and D. P. Adam (1996), Environmental magnetic implications of greigite formation in a 3 m.y. lake sediment record from Butte Valley, northern California, *Geophys. Res. Lett.*, *23*, 2859-2862.

Roberts, A. P., W. T. Jiang, F. Florindo, C. S. Horng, and C. Laj (2005), Assessing the timing of greigite formation and the reliability of the Upper Olduvai polarity transition record from the Crostolo River, Italy, *Geophys. Res. Lett.*, *32*, L05307, doi:10.1029/2004GL022137.

Roberts, A. P., Q. S. Liu, C. J. Rowan, L. Chang, C. Carvallo, J. Torrent, and C. S. Horng (2006), Characterization of hematite (α-Fe_2O_3), goethite (α-FeOOH), greigite (Fe_3S_4), and pyrrhotite (Fe_7S_8) using first-order reversal curve diagrams, *J. Geophys. Res.*, *111*, B12S35, doi:10.1029/2006JB004715.

Rodríguez-Carvajal, J. (1993), Recent advances in magnetic structure determination by neutron powder diffraction, *Physica B*, *192*, 55-69.

Ron, H., N. R. Nowaczyk, U. Frank, M. J. Schwab, R. Naumann, B. Striewski, and A. Agnon (2007), Greigite detected as dominating remanence carrier in late Pleistocene sediments, Lisan Formation, from Lake Kinneret (Sea of Galilee), Israel, *Geophys. J. Int.*, *170*, 117-131.

Rowan, C. J., and A. P. Roberts (2005), Tectonic and geochronological implications of variably timed remagnetizations carried by authigenic greigite in fine-grained sediments from New Zealand, *Geology*, *33*, 553-556.

Rowan, C. J., and A. P. Roberts (2006), Magnetite dissolution, diachronous greigite formation, and secondary magnetization from pyrite oxidation: Unravelling complex magnetizations in Neogene marine sediments from New Zealand, *Earth Planet. Sci. Lett.*, *241*, 119-137.

Rowan, C. J., A. P. Roberts, and T. Broadbent (2009), Reductive diagenesis, magnetite dissolution, greigite growth and paleomagnetic smoothing in marine sediments: A new view, *Earth Planet. Sci. Lett.*, *227*, 223-235.

Sagnotti, L., and A. Winkler (1999), Rock magnetism and palaeomagnetism of greigite-bearing mudstones in the Italian Peninsula, *Earth Planet. Sci. Lett.*, *165*, 67-90.

Sagnotti, L., A. Winkler, L. Alfonsi, F. Florindo, and F. Marra (2000), Paleomagnetic constraints on the Plio-Pleistocene geodynamic evolution of the external central-northern Apennines (Italy), *Earth Planet. Sci. Lett.*, *180*, 243-257.

Sagnotti, L., A. P. Roberts, R. Weaver, K. L. Verosub, F. Florindo, C. R. Pike, T. Clayton, and G. S. Wilson (2005), Apparent magnetic polarity reversals due to remagnetization resulting from late diagenetic growth of greigite from siderite, *Geophy. J. Int.*, *160*, 89-100.

Schmidbauer, E., and M. Keller (2006), Magnetic hysteresis properties, Mössbauer spectra and structural data of spherical 250 nm particles of solid solutions Fe_3O_4–γ-Fe_2O_3, *J. Magn. Magn. Mater.*, *297*, 107-117.

Schoonen, M. A. A., and H. L. Barnes (1991), Reactions forming pyrite and marcasite from solution. II: via FeS precursors below 100°C, *Geochim. Cosmochim. Acta*, *55*, 1505-1514.

Schwarz, E. J., and D. J. Vaughan (1972), Magnetic phase relations of pyrrhotite, *J. Geomag. Geoelectr.*, 24, 441-458.

Sherman, D. M. (1990), Mössbauer spectra, crystal chemistry, and electronic structure of greigite, Fe_3S_4, *Eos, Trans. A.G.U.*, *71*, 1649.

Skinner, B. J., R. C. Erd, and F. S. Grimaldi (1964), Greigite, the thiospinel of iron; A new mineral, *Am. Mineral.*, *49*, 543-555.

Smirnov, A. V. (2006), Low-temperature magnetic properties of magnetite using first-order reversal curve analysis: Implications for the pseudo-single-domain state, *Geochem. Geophys. Geosyst.*, *7*, Q11011, doi:10.1029/2006GC001397.

Snowball, I. F. (1991), Magnetic hysteresis properties of greigite (Fe_3S_4) and a new occurrence in Holocene sediments from Swedish Lappland, *Phys. Earth Planet. Inter.*, *68*, 32-40.

Snowball, I. F. (1997a), Gyroremanent magnetization and the magnetic properties of greigite-bearing clays in southern Sweden, *Geophys. J. Int.*, *130*, 624-636.

Snowball, I. F. (1997b), The detection of single-domain greigite (Fe_3S_4) using rotational remanent magnetization (RRM) and the effective gyro field (B_g):

Mineral magnetic and palaeomagnetic applications, *Geophys. J. Int.*, *130*, 704-716.

Snowball, I. F., and R. Thompson (1988), The occurrence of greigite in sediments from Loch Lomond, *J. Quat. Sci.*, *3*, 121-125.

Snowball, I. F., and R. Thompson (1990), A stable chemical remanence in Holocene sediments, *J. Geophys. Res.*, *95*, 4471-4479.

Spender, M. R., J. M. D. Coey, and A. H. Morrish (1972), The magnetic properties and Mössbauer spectra of synthetic samples of Fe_3S_4, *Can. J. Phys.*, *50*, 2313-2326.

Srivastava, C. M., and R. Aiyar (1987), Spin wave stiffness constants in some ferrimagnetics, *J. Phys. C: Solid State Phys.*, *20*, 1119-1128.

Stacey, F. D. (1963), The physical theory of rock magnetism, *Adv. Phys.*, *12*, 45-133.

Szotek, Z., W. M. Temmerman, D. Ködderitzsch, A. Svane, L. Petit, and H. Winter (2006), Electronic structures of normal and inverse spinel ferrites from first principles, *Phys. Rev. B.*, *74*, 174431.

Tang, Y., Q. W. Chen, Y. Xiong, and Y. Li (2007), Magnetic field-induced increase in conversion rate of Fe_3S_4 to FeS_2, *Chin. J. Inorg. Chem.*, *23*, 941-947.

Tauxe, L., T. A. T. Mullender, and T. Pick (1996), Potbellies, wasp-waists, and superparamagnetism in magnetic hysteresis, *J. Geophys. Res.*, *101*, 571-583.

Torii, M., K. Fukuma, C. S. Horng, and T. Q. Lee (1996), Magnetic discrimination of pyrrhotite- and greigite-bearing sediment samples, *Geophys. Res. Lett.*, *23*, 1813-1816.

Tric, E., C. Laj, C. Jéhanno, J.-P. Valet, C. Kissel, A. Mazaud, and S. Iaccarino (1991), High-resolution record of the Upper Olduvai transition from Po Valley (Italy) sediments: Support for dipolar transition geometry? *Phys. Earth Planet. Inter.*, *65*, 319-336.

Uda, M. (1965), On the synthesis of greigite, *Am. Mineral.*, *50*, 1487-1489.

Vandenberghe, R. E., E. De Grave, P. M. A. De Bakker, M. Krs, and J. J. Hus (1991), Mössbauer effect study of natural greigite, *Hyperfine Interact.*, *68*, 319-322.

van Dongen, B. E., A. P. Roberts, S. Schouten, W. T. Jiang, F. Florindo, and R. D. Pancost (2007), Formation of iron sulfide nodules during anaerobic oxidation of methane, *Geochim. Cosmochim. Acta*, *71*, 5155-5167.

Vasiliev, I., M. J. Dekkers, W. Krijgsman, C. Franke, C. G. Langereis, and T. A. T. Mullender (2007), Early diagenetic greigite as a recorder of the palaeomagnetic signal in Miocene-Pliocene sedimentary rocks of the Carpathian foredeep (Romania), *Geophys. J. Int.*, *171*, 613-629.

Vasiliev, I., C. Franke, J. D. Meeldijk, M. J. Dekkers, C. G. Langereis, and W. Krijgsman (2008), Putative greigite magnetofossils from the Pliocene epoch, *Nature Geoscience*, doi:10.1038/ngeo335.

Vaughan, D. J., and M. S. Ridout (1971), Mössbauer studies of some sulphide minerals, *J. Inorg. Nucl. Chem.*, *33*, 741-746.

Vaughan, D. J., and J. R. Craig (1978), *Mineral Chemistry of Metal Sulfides*, Cambridge University Press, Cambridge, 493 pp.

Vaughan, D. J., and J. A. Tossell (1981), Electronic structure of thiospinel minerals: Results from MO calculations, *Am. Mineral.*, *66*, 1250-1253.

Verwey, E. J. W. (1939), Electronic conduction of magnetite (Fe_3O_4) and its transition point at low temperatures, *Nature*, *144,* 327-328.

Walz, F. (2002), The Verwey transition - a topical review, *J. Phys. Condens. Matter*, *14*, R285-R340.

Wang, Q. W., and J. W. Morse (1996), Pyrite formation under conditions approximating those in anoxic sediments. 1: Pathway and morphology, *Mar. Chem.*, *52*, 99-121.

Watson, J. H. P., B. A. Cressey, A. P. Roberts, D. C. Ellwood, J. M. Charnock, and A. K. Soper (2000), Structural and magnetic studies on heavy-metal-adsorbing iron sulphide nanoparticles produced by sulphate-reducing bacteria, *J. Magn. Magn. Mater.*, *214*, 13-30.

Weiss, P. (1907), Hypothesis of the molecular field and ferromagnetism, *J. Physique*, *6*, 661-690.

Wilkin, R. T., and H. L. Barnes (1997), Formation processes of framboidal pyrite, *Geochim. Cosmochim. Acta*, *61*, 323-339.

Williams, W., and D. J. Dunlop (1989), Three-dimensional modelling of ferromagnetic domain structure, *Nature*, *337*, 634-637.

Winklhofer, M., and G. T. Zimanyi (2006), Extracting the intrinsic switching field distribution in perpendicular media: A comparative analysis, *J. Appl. Phys.*, *99*, 08E710, doi:10.1063/1.2176598.

Wright, J. P., J. P. Attfield, and P. G. Radaelli (2001), Long range ordering in magnetite below the Verwey transition, *Phys. Rev. Lett.*, *87*, 266401(4).

Wright, J. P., J. P. Attfield, and P. G. Radaelli (2002), Charge ordered structure of magnetite below the Verwey transition, *Phys. Rev. B.*, *66*, 214422(14).

Yamaguchi, S., and T. Katsurai (1960), Zur bildung des ferromagnetischen Fe_3S_4, *Kolloid Zeit.*, *170*, 147-148.

Yamaguchi, S., and H. Wada (1969), Zum hydrothermal synthetisierten Eisen-Thiospinell, *Naturwissenschaften*, *56*, 138.

Yamaguchi, S., and H. Wada (1970), Magnetic anisotropy of Fe_3S_4 as revealed by electron diffraction, *J. Appl. Phys.*, *41*, 1873-1874.

Zhang, Z., and S. Satpathy (1991), Electron states, magnetism, and the Verwey transition in magnetite, *Phys. Rev. B.*, *44*, 13319-13331.